# EVIDENCE OF ACCRETION-GENERATED X-RAYS IN THE YOUNG, ERUPTING STARS V1647 ORI AND EX LUPI

By

William Kenneth Teets

Dissertation

Submitted to the Faculty of the

Graduate School of Vanderbilt University

in partial fulfillment of the requirements for

the degree of

DOCTOR OF PHILOSOPHY

in

Physics

May, 2012

Nashville, Tennessee

Approved:

Professor David A. Weintraub

Professor Andreas A. Berlind

Professor Jocelyn K. Holley-Bockelmann

Professor Keivan G. Stassun

Professor David J. Furbish

# Table of Contents

# ACKNOWLEDGMENTS

This work would not have been possible if it were not for the efforts of many people who have made a major impact in my life, and I would feel it would be a great disrespect if I did not acknowledge the people who have played such an important role in getting me to this point in my career.

First and foremost, this dissertation would not exist if it were not for my parents, Cheryl and Bill. Through their loving efforts, they have made me what I am today, and I cannot thank them enough for all that they have done for me in my thirty years of life. In addition, I would like to acknowledge my many friends and family members, too numerous to name individually, that have supported me in my endeavors.

I would have to say that my love of astronomy began from a seed that my parents planted in my mind when I was a young child. They provided me with my first telescope - a small refractor. Though we weren't able to find much more than the Moon or a few bright stars, this nevertheless fostered my love of astronomy. I remember flipping through the many astronomy books they bought me when I was very young (all of which I still have today) and marveling at the beauty of the universe, wondering if I could be an astronaut someday.

Once I was in high school, my love of astronomy and space science accelerated. For Christmas one year, my parents bought me another telescope, this time a 4.5" Newtonian, which was an upgrade from the small refractor that I had received many years before. The first clear night I had it out I was able to view Jupiter and Saturn. I dashed in and brought my parents out to see the two planets I had observed for

the first time through a telescope, allowing them to see the two heavenly bodies telescopically for the first time as well. From then on, I continued learning the constellations and star names, researching the many types of objects that I could now view, and staying up late many nights to observe the sky.

When I was in college at Austin Peay State University, I began taking physics courses (quickly changing my major from Engineering Technology to Physics once I discovered my true love of physics). I quickly became great friends with the Physics & Astronomy faculty. At this point, I also began participating in the observation nights held for our astronomy classes, operating the 8" Meade LX-90 and 10" Dobsonian telescopes that I had purchased with the remainder of my scholarship funds. I quickly learned that, along with my love of astronomy, I also had a passion for teaching it as well- I now had a career goal in mind. The faculty and staff of the APSU Physics & Astronomy department, namely Drs. Jaime Taylor, Spencer Buckner, Alex King, and Pei Xiong-Skiba, along with Sherry Bagwell, helped me pursue this career. I am greatly indebted to these wonderful people.

Once I had received my bachelors in Physics, I was accepted to the Physics graduate program at Vanderbilt University. I was one of six individuals accepted that year to become part of the graduate program that had an emphasis in astronomy. After several years of taking classes and acting as a teaching assistant for several astronomy lectures and many astronomy lab sections, I became a research assistant to Dr. David Weintraub. Through my interaction with David I have not only gained an enormous understanding of young stars and other aspects of my research field but I have also learned how to become a good researcher, gained an understanding of how

to question and interpret scientific results, and also learned how to become a good messenger of the science that I love. I would also like to acknowledge the immense help and understanding that he and the other members of the Physics & Astronomy faculty and staff provided me in getting to the point of having "Dr." in front of my name.

The staff of Dyer Observatory have also played an immeasurable role in my success as well. The constant encouragement of Rocky Alvey, Lynn McDonald, Nathan Griffin, Nancy Dwyer, Dr. Arnold Heiser, and Dr. Rick Chappell has helped me move towards the completion of my doctorate at Vanderbilt. In addition, Dyer Observatory has provided me with extensive experience in public outreach and education. I have come to learn firsthand that Dyer Observatory and the people associated with it are very special, and I am truly blessed to be a part of the observatory and to be able to call these folks my friends.

Last, but not least, I would like to also acknowledge my friend and partner, Kevin Thomas. Kevin has supported me in my efforts on countless occasions, giving me emotional support through rough times and also helping keep me in check to get to the finish line. He is a truly wonderful person and I am so very lucky to have him in my life.

# List of Tables

## List of Figures

# CHAPTER I

## INTRODUCTION

Why should we be interested in star formation? The obvious answer is that in several ways we owe our existence to stars. One reason is that our very own star, the Sun, makes its appearance each day in our lives. For humans, the direct, everyday influence of the Sun comes in the form of literally lighting our path, providing a warm environment in which we live our lives and giving us a source of power. The Sun drives Earth's climate and local weather patterns, indirectly providing us with necessities like food and water. This seemingly ordinary star is important to every living creature on Earth in one way or another. This alone is reason enough to ponder the mysteries of this star as well as the rest of the stars that we gaze at each night or observe with a telescope.

We also owe a debt of gratitude to other stars, specifically the stars that are no more – the previous generations of stars that long ago died out even before our solar system began to take shape. These stars forged the heavier elements in the nuclear furnaces of their cores or in the explosive processes that took place when they died. At the ends of their lives, they either obliterated themselves in the spectacular cataclysms of supernovae or swelled into large planetary nebulae of sublime beauty. In their death throws, they expelled into space the building blocks that ultimately led to our existence: the oxygen that we breathe, the phosphorus that forms the backbone of our DNA, and the silicates that form the crust of our planet. All life

on Earth, nay, the entire solar system, owes its existence to these element factories. That alone is reason enough to study and try to understand how these objects form, tick, and evolve.

With the requirement that X-ray astronomy be done with orbiting X-ray observatories because X-rays do not penetrate Earth's atmosphere, the amount of understanding gained through X-ray observations of young stellar objects (YSOs), when compared to what we know about stars and star formation from observations in, say, optical and infrared wavelengths, is not as plentiful. Yet, we find that young stars often produce copious amounts of X-rays, especially when compared to our Sun. In order to more fully understand the lives of stars, we must determine why this is. With so much energy being produced by young stars in the form of X-ray photons, this high-energy flux is likely to have a strong influence on the local environments of the stars. Not only will understanding X-ray generation in YSOs be beneficial to our understanding of how stars work, but it will also be important for understanding how other things, such as planet formation, are influenced by X-ray production. By studying young, solar-like stars characterized by strong X-ray emission, we are effectively able to look back in time and get a glimpse of what our early Sun looked like and what effects it had on the nascent solar system that would eventually be our home.

In the last few decades, as X-ray observations have become possible and technology has advanced to increase the sensitivity of our observations, much work has been done on this subject. As with virtually all facets of the sciences, there is almost never a single reason or explanation for an observed phenomenon, and this is also the case

for X-ray production in young stars. The focus of this dissertation is to explore some of the aspects of X-ray production in young stars. Specifically, we will use examples of erupting young stars as a testbed for one possible X-ray generation mechanism: accretion of circumstellar material. In §1, I present an overview of star formation. In §2, I describe the types of objects that are used as the focus of my X-ray analysis and present what is known and not well understood regarding these particular objects. I also discuss how these objects are related to the formation of stars like our Sun. In §3, I begin by presenting an overview of previous work regarding X-ray studies of young stars and the types of information that have been gleaned. Afterward, I focus on the tools of X-ray astronomy, namely the Chandra X-ray Observatory (CXO) and its instruments and capabilities. I also discuss the software tools that I used to reduce and model the data. §4 concerns my own X-ray work done with CXO observations of the young, erupting star V1647 Ori during the optical eruptions that were observed to begin in 2003 and 2008, while §5 deals with X-ray observations of another young, erupting star, EX Lupi, during its optical eruption of 2008. Finally, in §6 I discuss the overall results of the X-ray studies of V1647 Ori and EX Lupi and their implications. I conclude with a brief summary of the questions that the work of this dissertation has helped answer regarding X-ray production in young stars and what questions still remain unanswered.

### 1.1 An Overview of Star Formation

In order for star formation to occur, several ingredients must be present. First, the building blocks of the future star have to be present, i.e., a large cloud of gas and dust

known as a molecular cloud. These stellar nurseries usually consist (by mass) of 90% hydrogen, 10% helium, and less than 1% heavier elements; the heavy elements are mostly the products of previous generations of stars. Second, the environment has to have the correct conditions to support the formation of a star. Most notably, the local temperature has to be cool, no more than a few tens of Kelvins. At temperatures higher than this, the internal gas pressure is too strong to allow for core collapse. Infrared observations of dark nebulae, clouds of dust and gas that are thick enough to be opaque to visible light, show that young stars are forming within the confines of the cloud. A typical example of such an area suited for star formation is the Carina Nebula, shown in Figure 1.

Figure 1: False-color, Hubble Space Telescope visible light (left) and near-infrared (right) images of a portion of the Carina Nebula. Both figures are at the same spatial scale. The visible-light image shows an optically thick cloud of gas and dust. The infrared image allows us to peer into the cloud (which is barely detectable now) and observe a young star on its way to being fully formed. In this case, the young star also exhibits a bipolar jet.

Finally, when the stage is set with a cold interstellar cloud, core collapse of the cloud must be triggered by some means. The trigger mechanism does not have to be

violent. For example, radiation pressure of nearby stars can compress gas to create an over-density of material in part of the cloud, which can start the collapse of part or all of the cloud. Supernovae send out shockwaves that ripple through the interstellar medium. When a pressure wave comes in contact with an interstellar cloud, a shock forms as the high-speed wave slams into the slower-moving cloud, creating a region of high over-density. Gravitational encounters between galaxies can lead to large amounts of gas being stripped from each galaxy as they perform their gravitational tango, leading to tidal tails millions of light-years long. As the gas clouds of one galaxy are stretched and compressed by the gravitational influence of the interacting galaxies, over-densities arise in the gas. This often gives rise to massive amounts of star formation all at once, prompting astronomers to know many of these interacting bodies as "starburst galaxies."

In order to start the process of core collapse, even with all of the listed ingredients and trigger mechanisms, the Jean's stability must be overcome (Eq. 1.1).

$$\frac{dP}{dr} = \frac{G\rho M_{enc}}{r^2} \tag{1.1}$$

Equation 1.1 shows that the outward pressure $P$ in a volume over a given distance $r$ is determined by the gravitational force that is trying to collapse the mass enclosed inside the given volume ($M_{enc}$) with a certain density $\rho$. In an "inert" cloud, the thermal pressure (and other internal forces such as support from a magnetic field) of the material is in balance with the gravitational force. In order to start the collapse of the cloud, the external trigger mechanism must apply enough force so that the

internal pressure will be overcome. Once this occurs, the resulting over-density in the cloud has a stronger gravitational field, and a run-away process of contraction can start.

As an interstellar cloud collapses in on itself, the original cloud begins to fragment into separate clumps that each form a star. This is the main reason why, when sampling a stellar population, one finds that most stars are not single. Much work has been done to try and determine what factors lead to single or multiple-star formation. For example, Boss (2009) found through his three-dimensional hydrodynamic modeling that the strength of the magnetic field that pervades the cloud, as well as whether the initial rotating molecular cloud was prolate or oblate, has a significant impact on whether single or multiple protostellar cores are formed during collapse. However, the fragmentation process remains poorly understood.

### 1.1.1 Circumstellar Disks

In 1755, the German philosopher Immanuel Kant hypothesized that many of the "fuzzy" celestial objects observed via telescopes were dusty clouds in the process of forming stars and planets. In 1796, the French mathematician and astronomer Pierre-Simon Laplace proposed a similar model, arguing that the nearly-circular orbits of the planets were a direct result of the formation process (Woolfson, 1993). Today, the general model put forth by Kant and Laplace is accepted as the formation theory for the solar system. Usually known by names such as the Solar Nebula Disk Theory, this model starts with a protostellar clump that is on its way to becoming a fully-fledged star. Once a protostellar clump has formed within an interstellar cloud

and is contracting, its rotation speed as it collapses increases due to conservation of angular momentum. The roughly spherical cloud begins to flatten as the centrifugal force on the particles begins to counteract the gravitational force component that is perpendicular to the spin axis; however, the remaining gravitational force component, parallel to the spin axis, is not affected. The particles begin to settle towards a central plane perpendicular to the spin axis of the system. Over time, the once roughly-spherical cloud becomes a central mass surrounded by a disk. Numerical modeling of protostellar clumps indicates that this collapse phase lasts on the order of $\sim 10^6$ years (Yorke & Bodenheimer, 1999).

The Laplace model of solar system formation, while successful at explaining the overall structure of a solar system, was unable to fully explain how the Sun, with over 99% of the mass of the solar system, accounts for less than 1% of the total solar system angular momentum. Attempts had been made in the following years at modifying this model, but each attempt usually gave rise to other unexplainable issues. Prentice (1978) modified this formation model in such a way that the "Modern Laplace Model" was able to correctly predict many of the observed properties of the solar system including the angular momentum distribution. This model takes into account the formation of dust grains in the center of the cold disk which impart drag onto the collapsing disk. The gas at the center of the disk loses momentum and further collapses to form a slowly-rotating sun which, in the end, has one-hundredth of the total angular momentum of the disk. As the protostar's temperature increases, the dust grains evaporate while the planets continue to form in the faster-rotating disk.

With advancements in telescope and detector technology, the Solar Nebula Disk Theory has gained significant support, especially through direct observations of disks around some objects. Figure 2 shows several prime examples of young stars with disks seen both edge-on and face-on to our line of sight. Due to the substantial amount of material orbiting the central stars, these circumstellar disks appear mostly in silhouette with some reflected starlight illuminating the tops and bottoms of the disks. In some of the image panes, bipolar jets associated with accretion are observed.

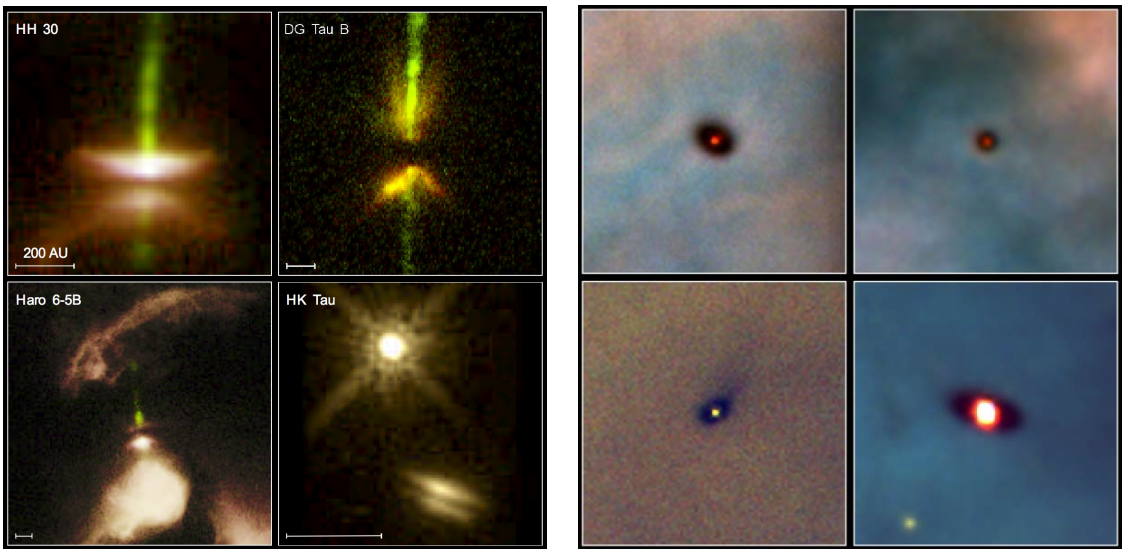


Figure 2: Edge-on circumstellar disks (left pane) and nearly face-on circumstellar disks (right pane) are observed mostly in silhouette around eight young stars. Image Credits: Chris Burrows (STScI), John Krist (STScI), Karl Stapelfeldt (JPL) and colleagues, the WFPC2 Science Team and NASA (left pane); Mark McCaughrean (Max-Planck-Institute for Astronomy), C. Robert O'Dell (Rice University), and NASA (right pane).

In many cases, especially when a target is very distant, direct observations of the disks are not possible. However, the signatures of circumstellar disks can be found

in the spectra of star-disk systems. Modeling of stellar spectra allows astronomers to determine many properties of stars. To nail down stellar parameters to within a high confidence level, the observed spectrum of the star has to match a synthesized spectrum very well. In the case of an "ordinary" star, the observed spectrum is usually modeled fairly easily, especially if the star is not extremely faint and if there are no peculiarities associated with the star's spectrum. The observed spectrum of a star surrounded by a circumstellar disk can be dramatically different, however, especially when one observes the system at infrared and longer wavelengths. Figure 3 shows the spectral energy distribution (SED) of the star GM Auriga, a star that is known to have a circumstellar disk. The SED of a system such as GM Auriga exhibits a flux contribution from the disk as well as from the star. The shorter wavelength flux of the SED, primarily those of the optical, are contributed mostly by the star itself. Longer wavelength data provide evidence of the disk. Instead of observing the expected decline in flux past the optical wavelength regime, the flux actually decreases much less due to the circumstellar material, which is radiating at infrared wavelengths after being warmed by its star or by accretionary growth of the disk itself. This "infrared excess" is the contribution of the disk to the SED. The bluer wavelengths, which are contributed by the star, provide the spectral information that allow one to model the stellar spectrum. This is not always an easy task as the more heavily-embedded the object is, the redder it appears due to scattering of the bluer wavelengths by intervening dust. If enough visible light emerges from the star-disk system, then a stellar spectrum can be derived. With that, then by carefully studying and modeling the shape of the infrared excess, one can determine many aspects of

the circumstellar disk, such as the inner disk radius, the vertical geometry of the disk, and the inclination of the disk to our line of sight.

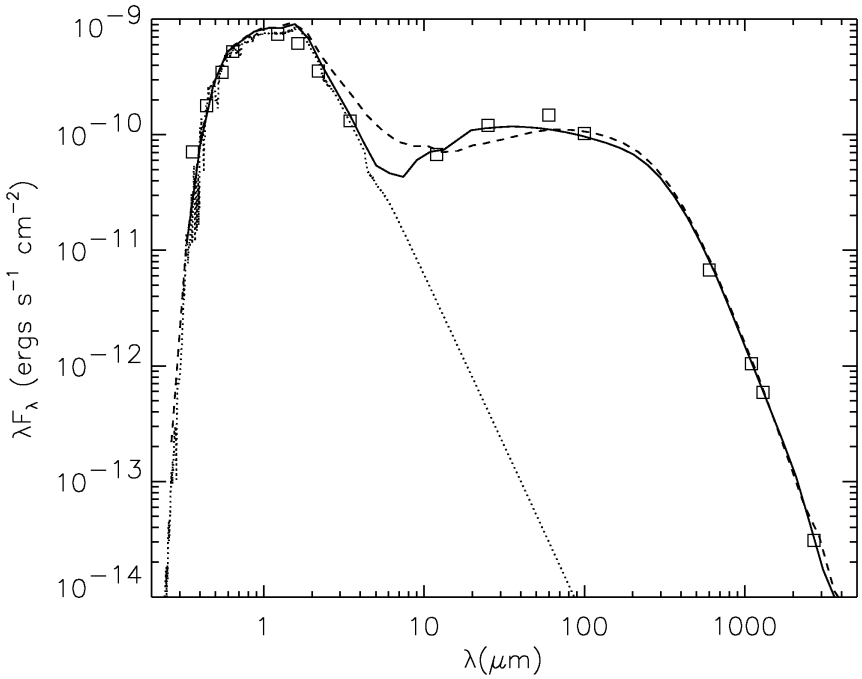


Figure 3: Spectral energy distribution (squares) of GM Auriga overlaid with the modeled SED of the stellar photosphere (dotted line) and the combined modeled stellar and circumstellar disk SEDs (solid line) with the disk viewed at an inclination of 50°. The disk begins 0.05 AU from the star and extends outwards to about 300 AU. The dashed line represents the same SED but with the disk extending inward to within 7 stellar radii instead of a having a large gap between the star and the inner disk boundary. Figure adapted from Figure 3 of Rice et al. (2003).

When considering the life of a star, the presence of a circumstellar disk can be considered a transient phase of a star's evolution. By observing a multitude of stars of various ages, each star gives us a snapshot into the stellar life cycle and allows us to determine the expected circumstellar disk lifetimes. Haisch et al. (2001) used measurements of infrared fluxes to determine the infrared colors of stars in six young

clusters. They found a strong correlation between the age of the cluster and the fraction of stars in each of the clusters that show infrared excesses characteristic of the presence of circumstellar disks. Starting with the youngest observed cluster ($\geq$80% of cluster members possessed circumstellar disks), Haisch et al. (2001) found that the cluster disk fraction decreased to 50% with an increase in age of approximately 3 Myr, suggesting that the overall disk lifetime of young stars is roughly 6 Myr.

Wolk & Walter (1996) observed 39 stars with strong infrared excesses and found that some appeared to have "transition disks," circumstellar disks that are in the process of dispersal and that are transitioning from optically thick to optically thin. By multiplying the fraction of stars observed to have transition disks with the mean age of the stars, they deduced that circumstellar disks have an optically-thick lifetime (the time it takes for the disk to go from optically thick to optically thin) of $\sim 10^5$ years. After that, the disks are dominated by micron-size dust grains. The presence of disks around stars older than a few million years is thought to be due to collisions of larger bodies within the disks. If these debris disks were primordial, then the detected dust out to $\sim$10 AU should have been depleted in $\sim 10^5$ years due to Poynting-Robertson drag (Mamajeck et al., 2004). The lifetimes of optically thick and optically thin disks help to constrain planet formation theories in that we now know the typical periods of time during which there are reservoirs of material out of which planets can form.

### 1.1.2 Circumstellar Accretion

On occasion, material will be perturbed in the circumstellar disk and accrete onto the parent star through various mechanisms possibly involving gravitiational

perturbations or disk instabilities (e.g., see works by Clarke et al. (1989); Bell et al. (1991); Bonnell & Bastien (1992); Armitage et al. (2001); D'Angelo & Spruit (2012)) from the inner portion of the circumstellar disk. Such accretion is likely controlled by magnetic flux tubes that connect the star to the disk.

YSOs are known to be quite magnetically active, as is often indicated by pronounced CaII emission as well as observations of periodic transits of starspots (direct manifestations of magnetic activity), which are derived from the observed modulation of light curves (Stassun et al., 2006). Donati et al. (2007) have shown through three-dimensional modeling that the stellar magnetic fields are intimately linked with the magnetic fields of the circumstellar disk. During accretion, circumstellar material is funneled along magnetic field lines and deposited at high stellar latitudes, where it is shock-heated as it impacts the photosphere. The accretion footprint emits at ultraviolet and X-ray wavelengths. The accreting material above the footprint absorbs and thermalizes radiation given off at the shock, causing it to re-radiate this energy at longer wavelengths. Since the material density is high near the accretion footprint, this plasma often radiates more as a blackbody than as an optically thin gas. The ultraviolet and optical emission thus comes in the form of a continuum overlaid on top of the stellar spectrum. This accounts for the ultraviolet excess observed in the spectra of many known accreting stars. In addition, the spectral features of accreting stars are often "veiled;" that is, the absorption features, here mostly in the optical wavelength regime, are effectively filled in due to the presence of continuum emission.

Hydrogen-balmer emission lines are observed in the spectra of T Tauri stars and are thought to result from absorption and re-emission of flux in the stellar atmosphere

produced by the accretion footprint. The hydrogen gas is excited and/or ionized, and recombination of the ionized hydrogen and spontaneous emission from excited atoms produces the characteristic observed hydrogen emission lines.

# CHAPTER II

# ERUPTING YOUNG STARS

## 2.1 T Tauri Stars

There are literally dozens of variable star classes. The majority of these, however, involve fully formed main-sequence stars or, as in the case of many single star systems, stars that have evolved off the main sequence. Some of these variable star classes consist of binary systems in which the components are physically interacting with one another, typically causing the total observed flux to vary sporadically or quasi-periodically. Other binary systems have components that are distant enough from one another that they only interact gravitationally with one another. In these cases, the stars' orbital geometry causes them to eclipse one another, periodically varying the observed flux. Still other variable star classes involve single, evolved stars that pulsate. There are fewer variable star classes that exist which consist of very young objects that have not reached the main sequence. This is often because these objects are still deeply embedded in dusty regions, making many of them very difficult to observe or even notice in the first place.

When discussing the final formation of low-mass ($2M_{\odot}$ and smaller) stars, these objects are often grouped into a category of stars known as T Tauri stars (TTSs), named after the prototype T Taurus. T Taurus, or "T Tau", was first noted in 1852 by John Russel Hind (Barnard, 1895). Joy (1945) suggested that this star, along with ten others, should comprise a separate class of variable stars based on

spectroscopic and photometric characteristics. TTSs were found to vary irregularly by several magnitudes, showed strong emission features in their spectra, had spectral types that were indicative of lower mass stars, and were associated with nebulosity.

T Tauri stars are further categorized into "classical" T Tauri stars (cTTSs) and "weak-line" T Tauri stars (wTTSs) based on the strengths of emission lines in their spectra. WTTSs are considered by some to be in a later stage of TTS evolution and may have shed most or virtually all of their disks. Walter (1986) suggested that these stars are not post-T Tauri stars but should instead be considered "naked TTSs. One of the major problems in the field of studying T Tauri stars is how to classify these objects based on their spectral characteristics. In earlier work, a rule-of-thumb for separating these stellar classes concerned the equivalent width of the hydrogen-alpha emission line: if the equivalent width of the hydrogen-alpha emission line at 6563Å was greater than 10Å for a TTS, then the star was considered a cTTS. If the hydrogen-alpha equivalent width was less than 10Å or in absorption), then the star was classified as a (wTTS). As many have found, this classification scheme is not extremely robust. For instance, it can be difficult to determine, based on the hydrogen-alpha line profile, whether or not the star is accreting even though the hydrogen-alpha spectral line is in emission. Kurosawa et al. (2006) used several different models to simulate classical T Tauri stars that were exhibiting hydrogen-alpha emission. They found, for example, that some scenarios could produce the required hydrogen-alpha equivalent width through magnetospheric accretion, but other models that were dominated by disk-wind emission produced similar equivalent widths. A more robust classification method that makes use of the hydrogen-alpha cutoff was suggested by Martín

(1997). Once the TTS spectral classification has been determined, the equivalent width corresponding to the maximum amount of hydrogen-alpha emission that can be produced by the star solely from an active chromosphere (excluding things such as flares) is modeled. The amount of hydrogen-alpha emission above the calculated maximum value is therefore likely a product of accretion. For instance, equivalent widths greater than ∼10Å for early-M and ∼20Å for late-M spectral types would be indicative that accretion is occurring.

WTTSs do not possess strong emission features like their cTTS counterparts, so they have fewer spectral characteristics that set them apart from regular main sequence stars. In the case where circumstellar accretion has decreased such that emission lines are no longer present in the stellar spectrum, a wTTS would be difficult to distinguish from a main sequence star. Since these stars are very young, the $^{7}$Li absorption feature at 6708Å[1] has been found by some to be a good indicator that a star might be a wTTS. Martín (1997) assumed that all TTSs will have an initial lithium abundance and that the abundance should not be significantly affected for stars younger than 10 Myr. He then calculated the minimum lithium equivalent width that these stars should have, which is mostly dependent on the stellar effective temperature, and found that the predicted equivalent widths are indeed higher than what is observed for young clusters, such as the Pleiades (age ≈ 100 Myr).

Due to the young ages of these stars, most TTSs still possess circumstellar disks,

[1]As stars age, convection effectively mixes their outer layers, and the lithium is transported into the lower convective layers where it is photo-dissociated by the higher temperatures. Thus, as stars age and the lithium in the outer part of the star is depleted, the equivalent width of the lithium spectral features decreases.

which provide mass reservoirs from which the stars can grow through circumstellar accretion. Typical mass accretion rates for T Tauri stars are around $10^{-9}$–$10^{-8}$ $M_{\odot}$ $yr^{-1}$ (Calvet et al., 2004), though this value can vary widely. Accretion of circumstellar material onto the central star results in flux increases in the X-ray through infrared wavelength regimes and also causes the star to appear variable as the accretion rate fluctuates or the accretion stream geometry changes. In addition, infalling material absorbs some of the bluer flux from the emission line, reducing the overall amount of the blue-wing emission of some emission features. In cases where the absorption is strong enough, the emission line blue wings go into absorption while the remainder of the feature stays in emission, producing what is known as an inverse P-Cygni profile.As material impacts the photosphere, the energy generated also ejects material from the star, generating a wind. The signature of this wind is observed in cTTS as a P-Cygni profile in the prominent emission lines. Though a wind would be expected to be produced in any direction (such that a redshifted and blueshifted component should be observed), the blueshifted wind component is observed most due to the optically thick circumstellar disk blocking our view of the redshifted component.

## 2.2 FUors and EXors

There are two prominent classes of cTTSs that are known to erupt because of sudden, large-scale accretion events: FUors and EXors. In general, it is thought that the main difference between these types of stars is the level of their "quiescent" accretion rates and the duration and magnitude of the large accretion episodes that they experience. Figure 4 illustrates they physical setup of these types stars and how

they exhibit the spectroscopic signatures of cTTSs, such as accretion and winds.

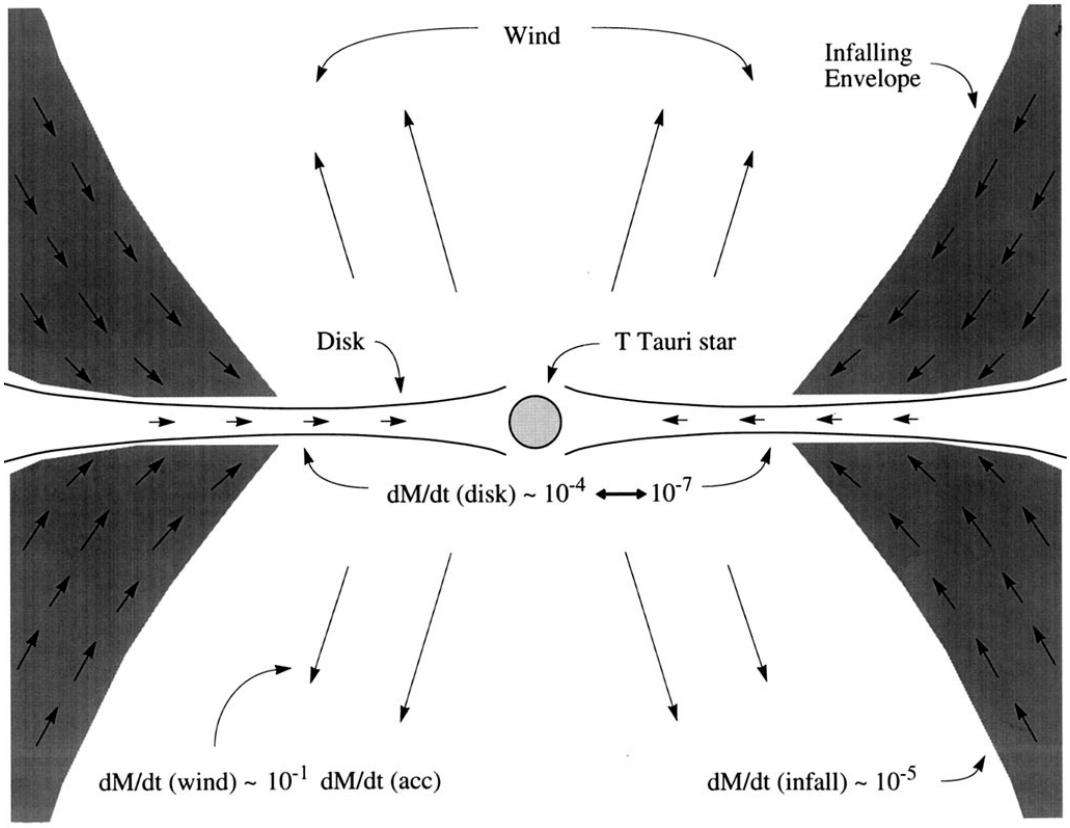


Figure 4: Schematic of an accreting T Tauri star. Figure adapted from Figure 1 of Hartmann & Kenyon (1996). Numbers quoted are for an FU Ori-type system; the same schematic applies to EX Lupi-type systems as well, but the values in the figure would be scaled down.

FUors are named after the prototype of the class, FU Orionis. FUors are thought to be YSOs due to their association with star forming regions (with many of them being heavily extincted) and their spectra exhibiting large infrared excesses (Weintraub et al., 1991). Many of them show signatures of having F to G spectral types, suggesting that these are low mass stars, i.e., T Tauri stars.

One of the defining characteristics of this class of YSO is the large optical eruptions that they are observed to undergo, with typical rise times of one to several years and decline times of decades to over a century (Fig. 5). FU Orionis, or FU Ori, was first observed to undergo an outburst between 1936 and 1937, when it rose six magnitudes in the B band. Since then, FU Ori has been gradually returning to its quiescent optical level but still has yet to reach its pre-outburst luminosity.

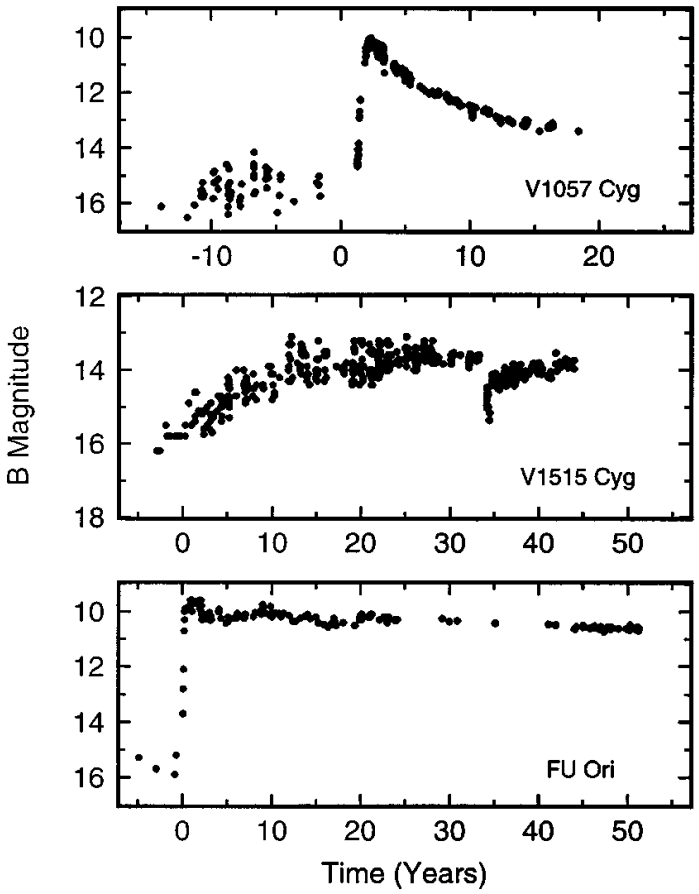


Figure 5: Optical Light curves of three FUors. Figure adapted from Figure 3 of Hartmann & Kenyon (1996).

FUors have typical accretion rates of $10^{-7}$ $M_{\odot}$ $yr^{-1}$, but the accretion rate rises by up to three orders of magnitude during large optical outbursts. During these large outbursts, the disk radiates most at optical wavelengths and can easily outshine its companion star (Hartmann & Kenyon, 1996). The eruptions are not thought to be due to dramatic changes in intervening extinction since the spectral features change when observing the star going from its minimum to its maximum optical level or visa versa (Herbig, 1977). However, with strong evidence to suggest that FUors are surrounded by circumstellar disks, it is thought that the observed eruptions are due to massive accretion events from the circumstellar disk. FUors were some of the first objects to have their outbursts explained successfully with a disk-accretion model (Lin & Papaloizou, 1985). Spectroscopic observations show absorption feature doublets (i.e., red-shifted and blue-shifted absorption lines), which are not characteristic of line broadening due to a fast-rotating star but are instead characteristic of material orbiting the star (Fig. 6). As one examines absorption features at longer wavelengths, the spread of the double-features decreases. Material (which is radiating as a blackbody in an optically-thick disk) would be cooler, orbiting at a slower rate, and radiating in longer wavelengths the farther out in the disk it is located. Thus, the longer-wavelength spectral doublets are indicative of material orbiting farther out from the star.

Hartmann & Kenyon (1996) determined that if one low-mass star were formed every 100 years for a 1kpc cylinder centered on the Sun, then given that there have been approximately five FUor outbursts in 60 years (as of 1996), then FU Ori outbursts should occur approximately 10 times for each low-mass star. Therefore, if the out-

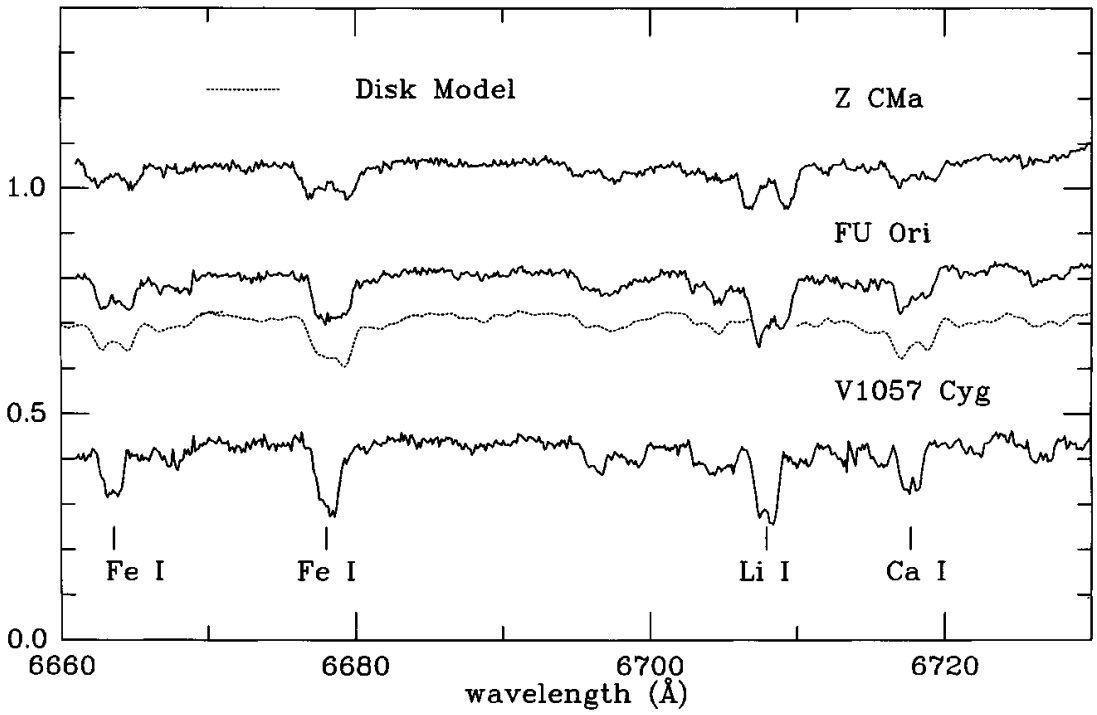


Figure 6: Portions of spectra of three FUors. The prominent absorption features show line-doubling. The thinner line under the spectrum of FU Ori represents a disk spectrum model for FU Ori. Figure adapted from Figure 6 of Hartmann & Kenyon (1996).

burst lasts a century, as appears to be the case for FU Ori itself, then low-mass stars could gain a significant amount of their final mass through these outburst episodes. This amount could be much higher, especially given that FUors tend to be located in heavily-reddened locations so that we may not be able to observe these eruptions very often.

Calvet et al. (1991) was able to successfully model the spectral contribution of the circumstellar disk for FUors. They assumed that the disk was in vertical hydrostatic

and radiative equilibrium and that the temperature varied as a function of radius in the disk. Calvet et al. (1991) then split up the disk into many concentric annuli and modeled each annulus in a stellar atmosphere radiative transfer method. From each model, an effective temperature and surface gravity were derived. They then combined the modeled spectral contributions from each annulus to determine the total spectral contribution of the disk. The spectrum of FU Ori was also modeled in this manner, and they were able to use the disk contribution to account for the optical spectral energy distribution of FU Ori itself, strongly suggesting that the disk of FU Ori outshines FU Ori. In addition, they found that the contribution of FU Ori to the heating of the disk is negligible (it was neglected in the modeling and not needed to get the modeled spectrum to fit the data) and that the presence of the strong absorption features indicates that the disk is also very optically thick.

EXors comprise another class of erupting star that is named after the prototypical star, EX Lupi. EXors are similar in some aspects to FUors, but they also have their differences that set them apart from FUors. EXors, however, have much lower maximum accretion rates as compared to FUors, and the rise times and subsequent decline times of optical outbursts are on the order of weeks and months to a few years, respectively. EXors are also observed to undergo optical outbursts much more frequently than FUors. EX Lupi, for example, was first observed to erupt in in 1901, with six later eruptions through 2008. Thus, EX Lupi has erupted nearly as many times during the typical span of one FUor outburst as what is predicted for a typical FUor.

During the 2008 "extreme" outburst of EX Lupi, the veiling-corrected accretion

rate was found to be $2 \times 10^{-7}$ $M_{\odot}$ $yr^{-1}$, which is approximately 40 times greater than the accretion rate during optical quiescence (Aspin et al., 2010). As compared with the quiescent accretion rate $10^{-7}$ $M_{\odot}$ $yr^{-1}$ for FU Ori, the accretion rates of EXors are found to be on the order of the quiescent accretion rates of FUors even when undergoing major outbursts.

# CHAPTER III

# X-RAY ASTRONOMY: A TOOL FOR STUDYING YOUNG STARS

## 3.1 Previous X-ray Work

The most obvious feature of the night sky is the thousands of stars that one can observe with the naked eye. Once the science of astronomy had evolved to the point of trying to use scientific means to derive information about the world and the universe itself, we naturally asked questions about these shimmering nighttime visitors. We began by observing what we could with our eyes, noting things such as brightness, color, and whether the stars appeared to vary in any way over time. With the invention of the optical telescope in 1609, we were able to increase our observing capabilities, as well as our understanding of stars, by many orders of magnitude. With the discovery of other types of light, such as infrared and ultraviolet, we began to ponder if these other forms of light might be tools to investigate other aspects of stars. We discovered in the twentieth century that our understanding of the lives of stars, and not just physical measurements of stars, would be greatly expanded with the use of infrared light, which allowed us to see into the dark, invisible portions of the celestial sphere and peer into dark molecular clouds and witness some of the earliest moments of a star's birth and development. A tremendous amount of work done in observing young stars in the optical and infrared wavelength regimes; however, the volume of literature regarding X-ray studies of young stars, especially cTTSs and wTTSs, is smaller. With optical and infrared light revealing so many secrets

of the lives of stars, what information could X-ray astronomy provide us, especially with regards to the lives of young stars? One of the big questions that is still not well answered is why many young stars, especially lower mass stars, are such strong sources of X-rays. X-ray studies of such objects are important for improving our understanding of the evolution of a star as well as of its circumstellar environment, in which planetary systems may be forming. Thus, X-ray observations of stars give us a glimpse into how the X-ray behavior of T Tauri stars like our nascent Sun affect the evolution of stellar systems.

The first observations of X-ray emission from T Tauri stars were made by the Einstein X-ray Observatory. Feigelson & DeCampli (1981) found eight sources in the Taurus and Orion star-forming regions that had X-ray luminosities of $\sim 10^{30}$–$10^{31}$ ergs $s^{-1}$, roughly three to four orders of magnitude greater than the Sun's X-ray luminosity of $\sim 10^{27}$ ergs $s^{-1}$ (Orlando et al., 2001). They concluded that due to the rapid X-ray variability of some of these stars (e.g., a $\sim$4-minute significant increase in X-ray luminosity in DG Tau), the high X-ray luminosity was likely produced near the stellar photosphere. Since then, astronomers who study X-rays from TTSs have identified different X-ray generation mechanisms, including solar-like coronal loops that are larger than the radius of the star, accretion shocks, and magnetic reconnection in accretion streams.

### 3.1.1 X-ray Production & Rotation

Previous work has found that there is sometimes a correlation between the rotation period of a non-accreting star and its X-ray luminosity. Specifically, the ratio

of the X-ray luminosity ($L_X$) to the bolometric luminosity ($L_{bol}$) increases with decreasing rotation period. Vilhu & Rucinski (1983) found that there also appears to be a "saturation level" of $L_X/L_{bol} \simeq 10^{-3}$ for G-K type stars with rotation periods shorter than 2–3 days. Wright et al. (2011) found that this may be due to the way that X-rays are generated via dynamo mechanisms inside the star (Fig. 7). Their findings suggest that the dominant X-ray generating mechanism for fast rotators is a convective (turbulent) dynamo and, as the stars age and their rotation periods have increased to a certain point ($\sim$2–3 days), the dominant dynamo mechanism switches to an interface-type dynamo. Therefore, once the rotation period of a "saturated" star has decreased past $\sim$2–3 days as the star ages, it appears that the dynamo mechanism changes and the value of $L_X/L_{bol}$ decreases such that the star then falls into the "unsaturated" X-ray regime.

For the Sun, X-ray activity is the result of magnetic activity heating the coronal plasma to X-ray-emitting temperatures. The complex magnetic field of the Sun is thought to be a combination of effects, primarily from an "$\alpha\omega$-dynamo." In this picture, the differential rotation of the Sun will cause the once-poloidal magnetic field lines to be effectively wrapped around the Sun (the "$\omega$" effect), while these wrapped magnetic field lines themselves twist due to rotation effects on magnetic flux tubes rising from deep within the Sun (the "$\alpha$ effect"). The Sun, however, is different from T Tauri stars in terms of internal structure. The Sun has a radiative zone that extends from the core to roughly three-fourths of the solar radius, while the remaining outer portion of the Sun transports the bulk of the generated energy via convection. This structure allows for the creation of an "interface dynamo" at the

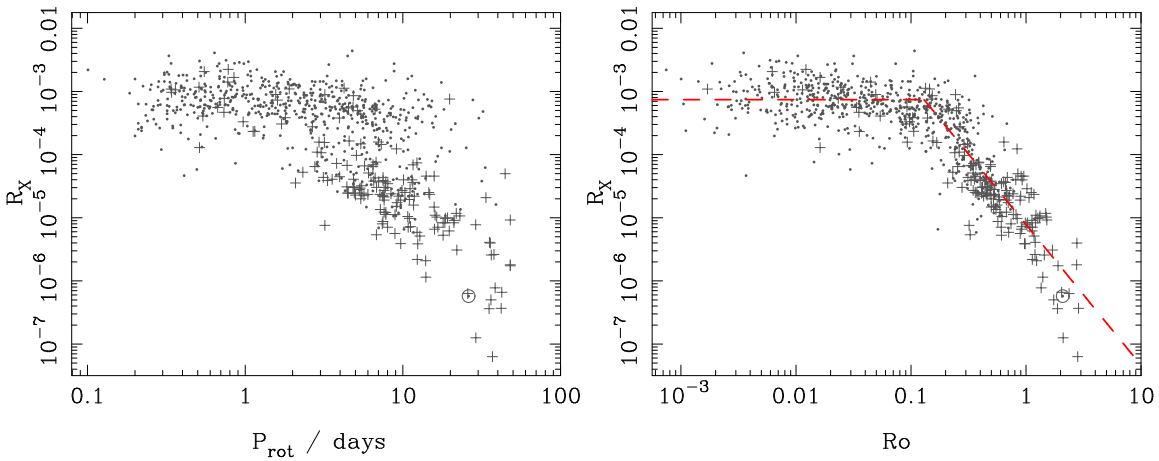


Figure 7: Figure 2 adapted from Wright et al. (2011) displaying X-ray to bolometric luminosity ratio ($R_X$) plotted against rotation period ($P_{rot}$)(left panel) and the Rossby number ($R_o$)(right panel) for all stars in the Wright et al. (2011) sample with X-ray luminosities and photometric rotation periods. Stars known to be binaries are shown as plus symbols, and the Sun is indicated with a solar symbol. These data show that ($R_X$) increases with decreasing ($P_{rot}$) and decreasing ($R_o$) up to a limit, at which point ($R_X$) saturates. The best-fitting saturated and non-saturated activity-rotation relations are shown as a dashed red line in the right-hand panel.

boundary between the radiative and convective zone which can generate a magnetic field. T Tauri stars, on the other hand, are fully convective, and thus are unable to create an $\alpha\omega$-dynamo. As a result, theorists now believe that fully convective stars are able to generate magnetic fields via a "turbulent" dynamo that is only weakly dependent on the rotation of the star.

Flaccomio et al. (2005) reanalyzed the results of Chandra Orion UltraDeep Project (COUP), a 2003 survey consisting of an 850 ks Chandra observation of the Orion Nebula Cluster (ONC). Flaccomio et al. (2005) specifically searched for clues as to how X-ray emission of ONC stars is related, if at all, to rotation. Restricting their analysis to stars with known rotation periods as well as using both unfiltered and

filtered light curves (which had large flares removed), they found that only 10% of their sample of stars showed evidence for X-ray modulation from rotation. In addition, they determined that the "X-ray saturation" that was observed in some of the sample is not due to the filling of the stellar photosphere with active regions and that the dominant X-ray emitting structures are smaller than the stellar radii.

### 3.1.2 X-ray Production & Coronal Structures

Surveys of the emission measure[2]-temperature distribution of many active binary stars (e.g., Sanz-Forcada et al. (2003)) found that there is often a prominent hot plasma component, at roughly 10 MK, along with a cooler plasma component similar to that found in the solar corona. Cargill & Klimchuk (2006) determined from their modeling results that the 10 MK plasma component is likely due to the presence of numerous small (loop height $\sim$ few thousand km), dense (electron densities $\sim 10^{12}$ $cm^{-3}$) coronal loops that are similar to, but much denser than, those found in the Sun.

Favata et al. (2005) found that a number of YSOs in the ONC produced large flares during the COUP observations. Models of these flares showed that many of them had loop heights that were on the order of at least 10 times the radius of the host star. With such large loop heights, Favata et al. (2005) concluded that these coronal loops, which confine the plasma responsible for the observed X-ray flares, also connect the stellar photosphere and accretion disk, allowing them to channel material falling from the circumstellar disk to the star during accretion.

[2]Emission measure is a determination of the amount of plasma contributing to observed emission.

### 3.1.3 X-ray Production & Accretion

One of the possible X-ray generation mechanisms is accretion of material from a circumstellar disk. Calvet & Gullbring (1998) determined that material near free-fall velocity can be shock-heated due to the large velocity gradient. They find that the plasma temperature, according to strong-shock theory, is given by

$$T_S \approx 3.5 \frac{M}{M_\odot} \left( \frac{R}{R_\odot} \right)^{-1} [MK]. \tag{3.1}$$

Substituting values for the radius and mass of typical TTSs (M = 0.1–1 $M_\odot$ and R = 0.5–2 $R_\odot$) into Equation 3.1, the expected shock temperature is $T_S \approx$ 0.4–4 MK, which corresponds to an X-ray temperature of $kT_X \approx$ 0.035–0.35 keV.

Stassun et al. (2006) searched for a possible link between X-ray production and accretion using COUP data and time-correlated BVRI photometry of young stars in the ONC. With accretion known to produce increases in optical flux, variability in optical flux (due to accretion) that is correlated with variability in X-ray flux would suggest that both flux variations are the result of accretion. Stassun et al. (2006) found that only 5% of their sample showed any correlation/anti-correlation between X-ray and optical variations, suggesting that accretion hotspots in the stellar photosphere are not dominant sites of X-ray production. However, it is still unclear as to why there is sometimes a correlation between optical and X-ray flux in some objects and not others when there are no observable characteristics that distinguish the stars in the 95% group from those in the 5% group.

### 3.1.4 Gleaning Other Information from X-rays

X-ray line profiles have also been used to determine characteristics of stars. Helium-like triplets (spectral features usually comprised of three spectral lines - a forbidden, an intercombination, and a resonance feature) can be used to determine plasma characteristics such as electron temperature and density. For example, the K-shell helium-like[3] transitions consist of a resonance line, two intercombination lines, and a forbidden line. The forbidden transition, which is observed to occur only at very low densities, can be collisionally excited to the excitation level of the intercombination lines. As density increases, the likelihood that an electron in the excited forbidden state will be excited to an intercombination energy state increases as the likelihood that an electron in the excited forbidden level will radiate spontaneously before being collisionally excited/de-excited decreases. Thus, the ratio of the forbidden to intercombination line strengths provides a proxy for density.

Kastner et al. (2002) observed the wTTs TW Hydra in 2000 with the Chandra X-ray Observatory using the High Energy Transmission Grating System and ACIS-S (CXO instruments will be in §3.2) . TW Hydra is known to be accreting due to the presence of hydrogen-balmer emission; however, determining the accretion rate from this line profile alone is often difficult to do with low uncertainty. The He-like Ne IX was observed in the high-resolution X-ray spectrum, and the relative line strengths were used to determine the electron density. After modeling the X-ray spectrum and deriving other plasma parameters such as emission measure, Kastner et al. (2002) were able to determine that the filling factor (the percentage of the stellar surface

[3]Helium-like refers to ions that have only have two bound electrons.

exhibiting this plasma) was much smaller than what is observed for normal coronal X-ray sources. They concluded that the plasma generating these spectral features likely arises from accretion hotspot(s) on the stellar photosphere. With the derived electron density and using an assumed filling factor and accretion stream velocity, the accretion rate was calculated for this object.

The X-ray spectrum of YSOs can also yield information about the circumstellar environment. The most notable example is the fluorescence of "cold" iron (iron that is weakly ionized) in the cirumstellar disk. Iron emission lines are often observed in the X-ray spectra of YSOs in the 6.7–7.0 keV range. This feature is the He-like Fe K$\alpha$-line triplet at 6.64, 6.67, and 6.70 keV. More recently, a neutral iron K-$\alpha$ doublet at 6.4 keV has been observed in the spectra of some YSOs, including those that are heavily embedded. These emission lines are the result of higher-energy X-ray photons (energy$\geq$7.11 keV) weakly ionizing iron atoms or ions through the removal of a 1s electron. Imanishi et al. (2001) provided the first detection of the neutral iron doublet in the X-ray spectrum of a deeply embedded YSO when observing YLW 16A in $\rho$ Ophichus (Fig. 8), and this feature was also detected in the X-ray spectrum of objects, such as V1647 Ori (Grosso et al., 2005; Teets et al., 2011) and seven sources in the ONC (Tsujimoto et al., 2005).

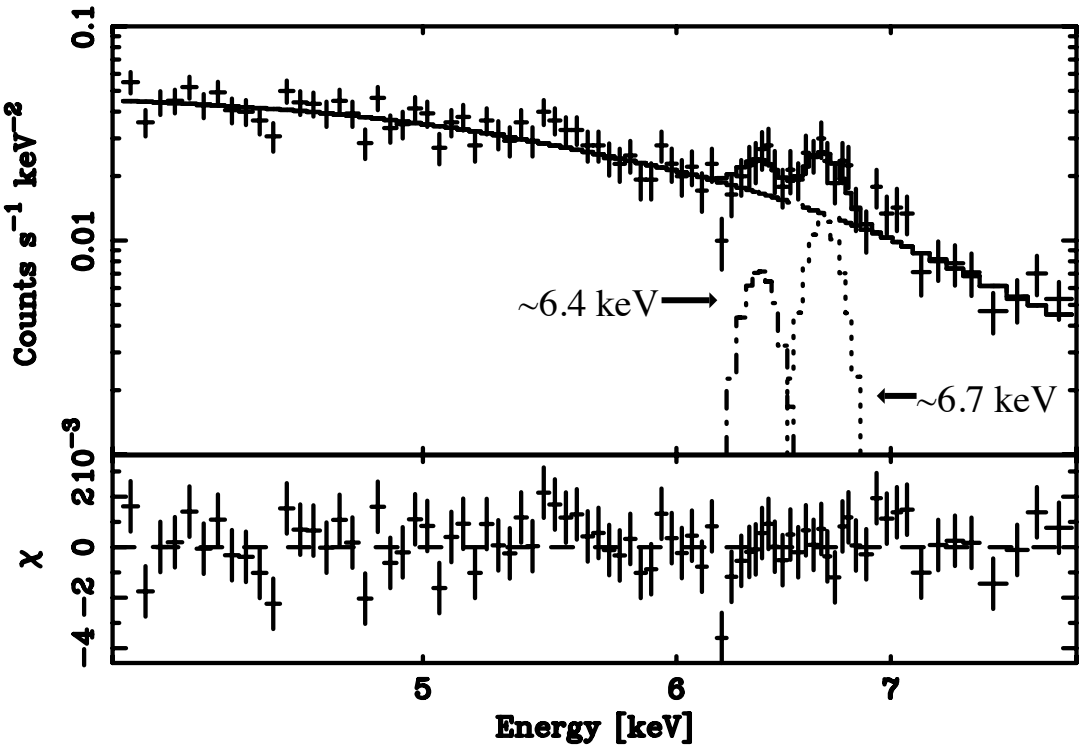


Figure 8: X-ray spectrum of YLW 16A (crosses) and the best-fit model (solid line), while the lower panel shows residuals from the best-fit model. The 6.4 and 6.7 keV spectral features are accounted for with the addition of two Gaussians (shown by the dot-dashed and dotted lines, respectively. Figure adapted from Figure 9b of Imanishi et al. (2001).

## 3.2 The Chandra X-ray Observatory

Launched from the Space Shuttle Columbia on July 23, 1999, the 45-foot long Chandra X-ray Observatory (CXO) is an orbiting X-ray telescope and the third of NASA's four "Great Observatories." CXO (Fig. 9) is named after Subrahmanyan Chandrasekhar, the Nobel prize-winning physicist most noted for first calculating the mass limit of a white dwarf. Chandra's rather eccentric orbit takes it into a high Earth orbit, putting it above the Van Allen belts for most of its 64.3-hour orbital period and allowing for roughly 55 hours of continuous observation time. The Chandra X-ray Observatory is unique in that it has the highest spectral and spatial resolutions thus far of any orbiting X-ray observatory – up to 0.012Å (or 1 eV) at Full Width Half Maximum (FWHM) and up to to 0.5″ at FWHM, respectively. Chandra's spectral range is 0.3–10 keV, and though other X-ray observatories such as XMM-Newton provide a wider calibrated spectral energy range, they have a lower spectral resolution. The Chandra X-ray Observatory has a suite of instruments and components, including the High Resolution Mirror Assembly (HRMA), the High Resolution Camera (HRC), the Advanced CCD Imaging Spectrometer (ACIS), and the Low- and High-Energy Transmission Gratings (LETG/HETG), which allow it to make a number of various types of X-ray observations.

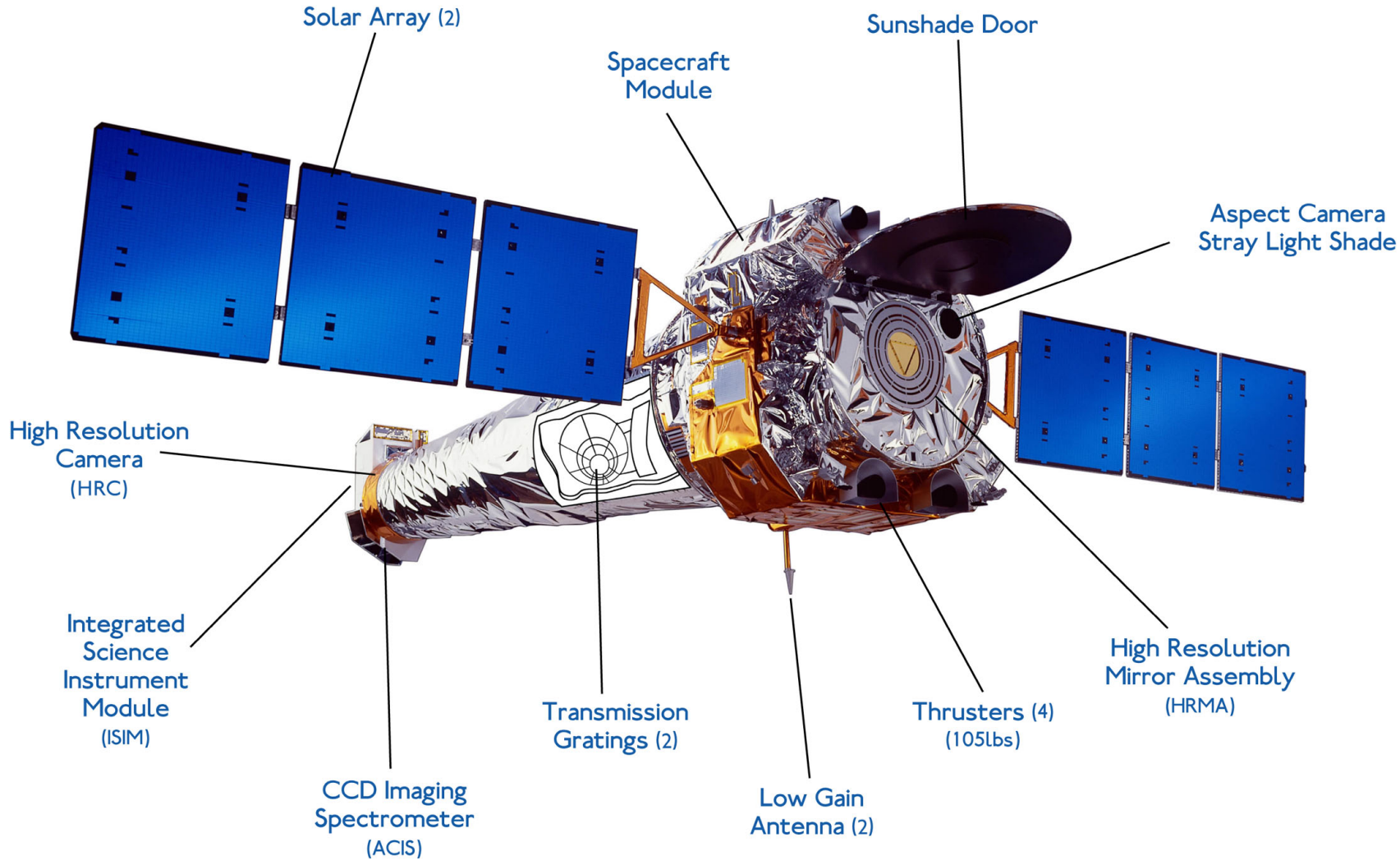


Figure 9: Schematic of the Chandra X-ray Observatory.

### 3.2.1 The High Resolution Mirror Assembly

The Chandra X-ray Observatory's telescope consists of four pairs of nested iridium-coated mirrors (Fig. 10) known as the High Resolution Mirror Assembly (HRMA). The mirrors of an X-ray telescope are cylindrical in shape, and Chandra's mirrors have diameters that range from 0.65 to 1.23 meters. A spherical mirror, such as that found in an optical telescope, would be unable to reflect and focus X-ray photons since X-ray wavelengths are on the order of the size of the atomic/molecular spacing of the material that makes up the mirror; i.e., the photons would typically pass through the mirror. To overcome this problem, mirrors make use of "grazing incidence" in which the surfaces of the mirrors are nearly (within a couple of degrees of) parallel to the path of the incoming X-ray photons. The photons are first intercepted by four nested mirrors that have a slight parabolic curvature. Afterwards, the photons are intercepted by a second set of mirrors, located behind the first set, which have a slight hyperbolic curvature. In effect, these mirrors gradually alter the trajectory of the photons, requiring the telescope to have a long focal length. As a result, the detectors have to be placed a large distance from the mirror assembly – the distance from the Central Aperture Plate (CAP), which separates the parabolic and hyperbolic mirrors of Chandra, to the focal point of the HRMA is 10.23 meters.

As with all telescopes, light gathering power and resolution are two of the major design concerns. How effectively the mirrors are able to reflect and focus incoming X-ray photons depends on the incoming X-ray photon energy as well as the grazing angle of the mirrors. Due to the cylindrical shape of Chandra's mirrors, the overall effective

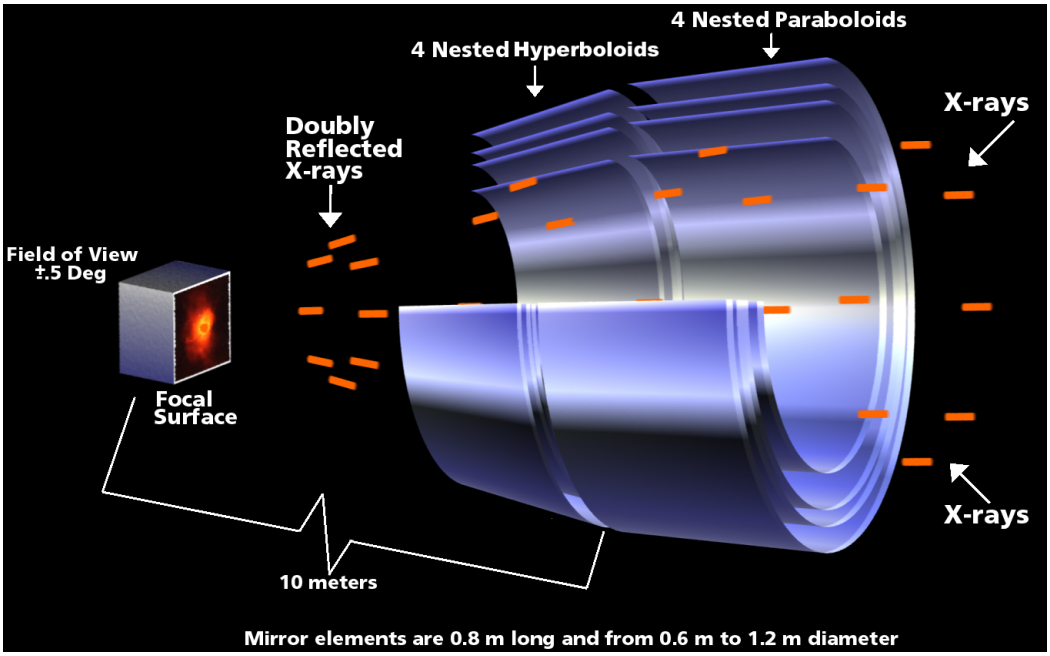


Figure 10: Schematic of the Chandra X-ray Observatory High Resolution Mirror Assembly. Image credit: NASA/CXC/SAO.

area of the mirrors (800 $cm^2$, 400 $cm^2$, and 100 $cm^2$ for 0.25 keV, 5.0 keV, and 8.0 keV photons, respectively) is very small. Multiple nested mirrors help to overcome these issues. In addition, due to the diffractive effects of the telescope system, the total amount of encircled energy within a given radius of the nominal aimpoint decreases with increasing energy; i.e., as the X-ray flux becomes harder (higher energy) for an X-ray source, the harder X-ray flux becomes less focused and the resolution of the source decreases. As a result, if a source is not within a few arcseconds of the nominal aimpoint, one must make use of an exposure map to compensate for the lost photons.

### 3.2.2 High- and Low-Energy Transmission Gratings

The High-Energy Transmission Grating (HETG) is mounted on a swing-arm so that it can be placed in the optical path during spectroscopic work (primarily with

one set of ACIS CCDs) and later retracted during imaging observations. The HETG (Fig. 11) is composed of two sets of gratings, with each set employing a different grating spacing. One set comprises the Medium-Energy Gratings (MEG), which are used in conjunction with the outer two pairs of mirrors and deal with the lower-energy (0.4–5.0 keV) X-ray photons, while the other set comprises the High-Energy Gratings (HEG), which are used in conjunction with the inner two mirror sets that focus the higher-energy (0.8–10.0 keV) X-rays. The MEG and HEG systems are composed of 336 individual gratings (144 HEG and 192 MEG) arranged on the HETG Support Structure (HESS), which places them in proper position behind the HRMA. The gratings themselves are composed of gold bars electroplated onto a polyimide substrate, with the bars and corresponding spacings roughly 0.1$\mu$m for the HEG and 0.2$\mu$m for the MEG. The rulings of the two sets of gratings are angled $\sim$10 degrees to one another so that the medium- and high-energy spectra are separated from one another. This results in the dispersed X-ray spectrum appearing as an "X". Due to multiple gratings needing to focus dispersed spectra onto a single focal plane, the gratings are arranged in several planes coinciding with the Rowland circle geometry while the detectors are placed on the opposite portion of the Rowland circle to intercept the focused spectra.

The Low-Energy Transmission Grating (LETG) is mounted on another swing-arm and operates in a similar manner to the HETG. The LETG is used primarily with the HRC-S array (energy range is 0.07 keV–10.0 keV), though it can be used with ACIS-S (energy range is 0.2–10 keV) with reduced quantum efficiency. Much like the HETG, the LETG gratings are mounted on a circular support structure, in this case known

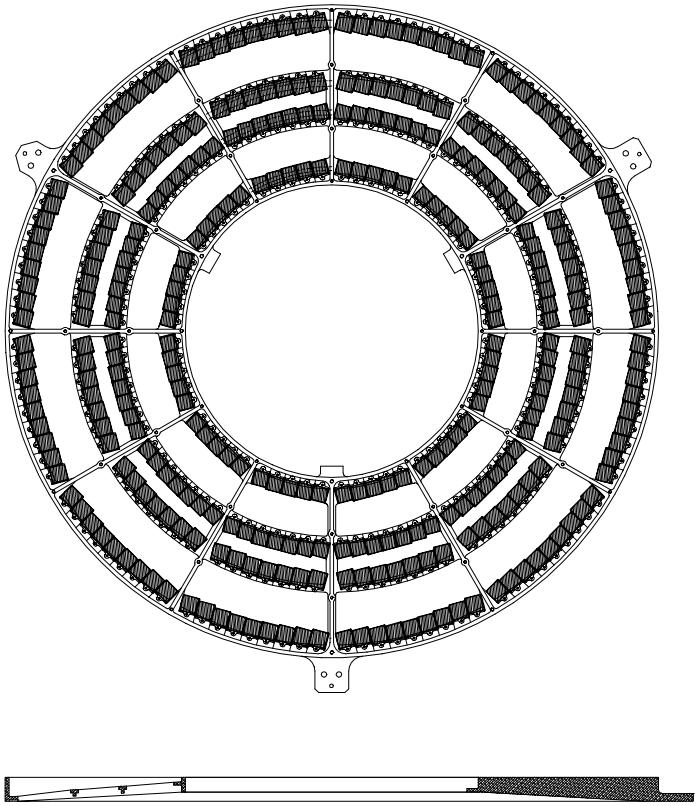

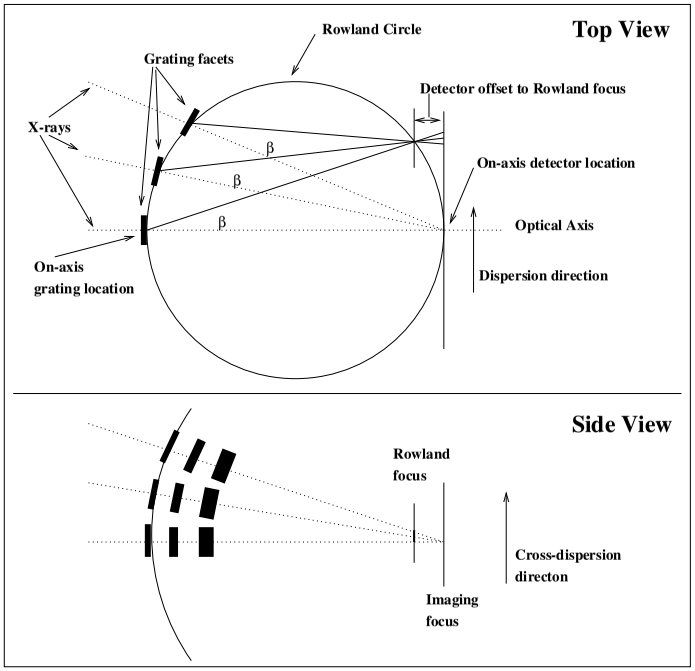


Figure 11: Schematic of the High Energy Transmission Grating viewed from face-on (top-left) and from the side (bottom-left). The Rowland geometry of the gratings and detector placement is shown in the right panel. Image credits: NASA/CXC/SAO.

as the Grating Element Support Structure (GESS), which places the gratings behind the HRMA when in use. The GESS supports a system of 180 grating modules, each of which has three grating facets that each contain 80 grating elements. In the case of LETG, the grating elements are triangular in shape and are composed of individual fine gold wires supported by coarser gold wires. Due to the triangular shape of the coarse support structure, the dispersed spectrum of an X-ray target is star-shaped at zeroth-order.

### 3.2.3 HRC

The High Resolution Camera (HRC) is one of two primary imaging instruments on the integrated Science Instrument Module (SIM) of Chandra. This camera is an imaging-optimized microchannel plate (MCP) detector (as opposed to the traditional CCD detector). The HRC, like ACIS, is composed of two sets of detectors. The HRC-I has the largest field of view of any of the science instruments ($30'$ by $30'$), and is optimized for imaging. HRC-S is optimized for spectroscopic work, has a field of view of $6'$ by $30'$, and is used in conjunction with the LETG.

A MCP works on the basis of photoemission. The HRC consists of two MCPs, each with millions of angled channels that are on the order of 10 microns in diameter. As an incoming X-ray photon intercepts the MCP, the photon enters a microchannel and, due to the angle of the channels, strikes the channel wall, which results in the ejection of an electron. Due to the bias charge between the two plates, the electron is accelerated down the channel, striking the wall again and releasing more electrons. This cascade effect continues through the channel, and a shower of several million

electrons eventually exits the output microchannel plate where they are intercepted by an array of detectors that record both the position and charge of an incoming signal. As multiple photons strike the MCP and the resulting electron showers are recorded by the position-charge detectors, an image is built up.

### 3.2.4 ACIS

The other workhorse detector of CXO is the Advanced CCD Imaging Spectrometer (ACIS). ACIS consists of 10 1024x1024 pixel CCDs, four of which are arranged in a 2x2 fashion (ACIS-I) and are used primarily for X-ray imaging. The remaining six CCDs (ACIS-S) are arranged in a horizontal row below ACIS-I and can be used for imaging or for X-ray spectroscopy when used in conjunction with one of the grating systems. Two of the ACIS-S CCDs (labeled "S1" and "S3") are back-illuminated while the remaining eight ACIS CCDs are front-illuminated. "Back-illuminated" and "front-illuminated" refer to how CCDs detect incoming photons. In traditional CCDs, the gate structures (discussed below) are mounted on the illuminated side of the CCD. Incoming photons can be reflected or absorbed by the gates and internal wiring of the chip before reaching the depletion layer (where the photons are "detected"). This can dramatically reduce the quantum efficiency of the chip. Back-illuminated CCDs have improved quantum efficiency since they are illuminated from the side opposite the gates and the chip substrate above the depletion has been dramatically thinned such that the substrate layer is essentially transparent to the incoming photons. Thus, the two back-illuminated ACIS-S CCDs have higher quantum efficiency in regard to the lower-energy (0.3$\sim$4.0 keV) photon range and have slightly better spectral resolution

than the front-illuminated CCDs.

Each of the 10 ACIS CCDs has square pixels 0.49″ on a side, giving each CCD a field of view of 8.3′. The total field of view is 16.9′ by 16.9′ for ACIS-I and 8.3′ by 50.6′ for ACIS-S. A maximum of six CCDs may be used simultaneously during an observation. A typical configuration uses all six of the ACIS-S CCDs or all four ACIS-I CCDs along with the S2 and S3 CCDs (either to maximize the imaging area for spatially extended X-ray sources or to increase the likelihood of serendipitous observations of other X-ray events).

When an X-ray photon (with an energy of at least 3.7 eV) strikes the (mostly) silicon CCD and is absorbed, electrons are liberated. The number of ejected electrons depends upon the energy of the incident X-ray photon. Due to the removal of an electron from a silicon atom, a net positive charge – a "hole" – is left behind. The freed electrons are then confined close to the interaction site via an electric field so as not to recombine with the holes. After an exposure, the confined charges are then transferred via "gate structures," each of which consists of three electrodes that effectively transfer confined charge from one pixel to another by rapidly varying the voltages in the electrodes. The gates are also what actually define the pixel boundaries in the CCD. When the transferred charge reaches the edge of the CCD, the charge is then transferred to a serial readout that then transfers each pixel charge to a local processor to determine the position and amplitude of any detected X-rays. Each full frame exposure lasts 3.2 seconds, effectively giving ACIS a cadence of ∼3.2 seconds. As opposed to a typical observation with an optical CCD where the user only sees a total flux in one filter after an entire observation, the high candence of ACIS allows

one to effectively determine the energy of each incoming photon and its corresponding time of arrival. With the effective energy and arrival time of each individual X-ray photon recorded, one can build up a crude spectrum as well as a light curve of an X-ray target; however, additional processing is required for high-flux X-ray sources that generate "pile-up," i.e., multiple photons can strike a single part of the CCD during the 3.2 second frame exposure and mimic the signal of a single, higher-energy photon.

### 3.2.5 Other Instruments of Note

Chandra is also equipped with an 11.2 cm Ritchey-Chretien optical telescope and CCD system mounted to the front of the observatory, which is part of the aspect control system known as the Aspect Camera Assembly (ACA). The primary function of the ACA is to monitor a fiducial LED system mounted around the Science Instrument Module (SIM). The system can also monitor up to five bright stars while simultaneously monitoring the fiducial LED system, providing possible optical monitoring of X-ray targets during an observation.

## 3.3 From the Telescope to Science Results -CXO Data Reduction

After the raw X-ray data are downloaded from the Chandra X-ray Observatory, they go through a standard data processing pipeline, carried out by the Chandra X-ray Center (CXC), in order to begin standard calibration of the raw data and ensure scientifically usable results. The processing pipeline goes through several stages, or"levels," in which various calibrations are applied. Afterward, the end products go

through "Verification and Validation" by CXC scientists to ensure the data quality and investigate any anomalies. Once the calibrated data are ready, the user then employs data reduction software to extract data from the science files.

The Chandra Interactive Analysis of Observations (CIAO) software was written to facilitate the analysis of Chandra X-ray data as well as data from other X-ray missions. This software allows the user to further reduce the data products to his/her individual scientific needs. In order to generate the final reduced data file, CIAO makes use of several data products that are produced via the CXC calibration pipeline. Numerous data files are available if the end user needs to re-reduce the final pipeline products, but the standard files needed are:

- Observation Fits File – This is the main file which contains all of the observation data (i.e., target and background data) that will be extracted and used to create X-ray spectra for analysis.

- Aspect Solution File – This file contains telemetry data concerning the orientation of the telescope throughout an observation. This file is used in combination with the events data file to determine the precise celestial position associated with a detected X-ray event. During an observation, Chandra is dithered, i.e., the spacecraft's aimpoint does not remain fixed throughout the observation but rather follows a Lissajous pattern. The main purpose of dithering is to smooth out pixel-to-pixel variations in the detectors, and the aspect solution file accounts for this motion.

- Bad Pixels File – As the name suggests, this file contains a list of known bad

pixels or pixel columns.

- Parameter Block File – This file contains information concerning how long each pixel of the given chip was exposed before being read out.

- Dead Area Correction Files – This standard set of calibration files is used to account for cosmic rays striking an ACIS CCD and rendering portions of it unusable during an entire frame.

- Mask File – This telemetry file denotes which parts of a CCD were active during an observation, and, thus, from which pixels are usable to extract events data. The active "window" of a CCD is determined by factors such as the pixel clocking mode.

With these calibration files, one of the typical routines used for extracting point-source spectra is the CIAO routine *specextract* (or *psextract* in previous versions of CIAO). This program utilizes several tools built into CIAO to apply the calibration files to the events file and produce reduced data products such as:

- Response Matrix File (RMF) – This file contains information concerning the detector response; i.e., it correlates the response of the detector with the pulse height read out by the CCD in order to determine the properties of the incoming photons, such as the photon energies.

- Ancillary Response File (ARF) – This file contains the effective area versus energy for the detector and telescope configuration of a given observation.

- Pulse Height Amplitude (PHA) or Pulse Invariant (PI) Files – This FITS file contains tabulated data regarding X-ray events detected during an observation. Mainly pertinent to the end-user is the "data" block of the file, which includes the detector channels, their corresponding energies, event count rates and the associated count rate errors, and the group that each channel belongs to in instances when the data are binned. PI files are essentially PHA files that have the RMF applied, i.e., the pulse-height amplitude has been converted to a corresponding energy using the detector response stored in the RMF file. A background PI file is created in addition to a source (target) PI file to allow the spectral modeling software to estimate the source spectrum contamination from background X-ray flux. One also typically uses CIAO to create a background light curve to determine if the X-ray background underwent any flaring during the observation, which could drastically affect the analysis of the target spectrum if not properly accounted for.

Once the spectrum files and their corresponding RMF and ARF files are created, spectral modeling can begin. The typical X-ray analysis packages used to model CXO X-ray data are XSPEC, X-ray spectral modeling software produced by the High Energy Astrophysics Science Archive Research Center (HEASARC) (Arnaud, 1996), or Sherpa, CIAO's built-in modeling and fitting software package (Freeman et al., 2001). These packages are mission-independent, meaning that even though they were written for analyzing CXO data they are also capable of modeling data from other X-ray missions such as XMM-Newton and Suzaku. These packages have a great

deal of built-in flexibility in how they can be used to model data. For example, one can model a single spectrum with a single model, simultaneously fit multiple spectra to the same model, or simultaneously fit multiple spectra to a single model but allow some parameters to vary per spectrum.

# CHAPTER IV

# X-RAY PRODUCTION BY V1647 ORI DURING OPTICAL OUTBURSTS

In this chapter, I present a manuscript that was published in the Astrophysical Journal in November 2011, which deals with analysis of the X-ray observations obtained of the young, erupting star V1647 Ori during its 2008 optical outburst. This paper, in which I am first author, is listed in the references of this dissertation as Teets et al. (2011).

## 4.1 Introduction

The young stellar object (YSO) V1647 Ori was first noted to be an erupting source when it brightened suddenly in November 2003, illuminating a new nebula now known as McNeil's Nebula. This deeply embedded, low-mass YSO is typically considered to be an EX Lupi-type object (an "EXor") though it shares some spectral characteristics with FU Orionis (Vacca et al., 2004), the prototype of a similar class of erupting pre-main sequence (PMS) stars ("FUors"). EXors are observed to brighten irregularly at optical wavelengths up to several times per decade; these outbursts persist for weeks to months (Herbig, 2001). FUors are YSOs that erupt less often than EXors, perhaps only once per century, and fade much more slowly, i.e., on timescales of years to decades (Herbig, 1977). The general consensus is that these eruptions are the result of massive accretion events that occur irregularly as young protostars grow; such accretion episodes may be the primary process through which young stars

accrete most of their mass (Hartmann & Kenyon, 1996). The mechanisms underlying EXor and FUor outbursts remain very poorly understood; however, models generally invoke the rapid onset of disk instabilities that lead to sudden inward migration of the inner disk truncation radius and dramatic changes in the star/disk magnetic field configuration (e.g., Zhu et al. (2009); Königl et al. (2011)).

Soft X-ray ($\sim$0.3 keV) generation via shock-heating of plasma at the bases of PMS accretion streams has been proposed for some objects from X-ray grating observations (see review by Güdel & Nazé, 2009) using plasma diagnostics based on helium-like ions (see review by Porquet et al., 2010), a prime example being TW Hydrae (Kastner et al., 2002; Brickhouse et al., 2010). On the other hand, studies such as the Chandra Orion Ultradeep Project (COUP) indicate that coronal activity, and not accretion, is likely the primary production mechanism for the harder X-rays that are characteristic of most pre-main sequence stars (Preibisch et al., 2005; Stassun et al., 2006). Debate still lingers as to the primary X-ray generation mechanism in YSOs during optical outbursts.

Since 2003, V1647 Ori has been observed to undergo two distinct outbursts that have been detected in the optical and near-infrared (McNeil, 2003; Itagaki et al., 2008) as well as at X-ray wavelengths (Kastner et al., 2004, 2006; Grosso et al., 2005; Grosso, 2006; Hamaguchi et al., 2010). The magnitudes and timescales for brightening and fading displayed by V1647 Ori do not match those of EXors. Furthermore, the duration of the initial outburst was shorter than those of FUors (Kastner et al., 2006; Aspin, Beck, & Reipurth, 2008). However, spectroscopic data do show signatures of accretion, such as strong H$\alpha$ and Br$\gamma$ emission (Reipurth & Aspin, 2004; Brittain et

al., 2010), confirming that the eruptions of V1647 Ori do resemble those of FUors and EXors.

V1647 Ori has been observed in X-rays before and during both of the eruptions (as well as after the first of the two eruptions) detected in the optical/near-infrared since 2003. Although other FUor- or EXor-like YSOs have been observed in X-rays (V1118 Ori (Audard et al., 2010); EX Lup (Grosso et al., 2010); Z CMa (Stelzer et al., 2009); FU Ori (Skinner et al., 2006); V1735 Cyg (Skinner et al., 2009)), V1647 Ori is the only eruptive YSO to undergo such extensive X-ray monitoring. During the 2003 eruption, the sudden rise in flux and subsequent decline in both the optical and near-infrared correlated strongly with a sharp increase and then decline in the X-ray flux, which suggests a common origin (Kastner et al., 2004, 2006). In this paper, we present and analyze X-ray spectra obtained with the Chandra X-ray Observatory (CXO) during the 2008–2009 outburst. In §4.2, we describe the observations and data reduction. In §4.3, we examine the trends and patterns seen in the X-ray emission from V1647 Ori over the past two outbursts, present modeling results for each of the five recent CXO observations, and compare these results to those obtained from previous (2003–2005) CXO and XMM-Newton observations. Finally, in §4.4 we discuss the implications of the results, and we argue that the measured properties of the X-ray emitting plasma are best understood within the framework of the accretion-generated X-ray hypothesis.

## 4.2 Observations & Data Reduction

Observations of V1647 Ori made with the Chandra X-ray Observatory (CXO) were triggered in 2008 September with a 20 ks observation (CXO Cycle 10, PI: D. Weintraub, ObsID 9915), after V1647 Ori was reported to have undergone a new optical outburst between early 2008 January and late 2008 August (Itagaki et al., 2008). Subsequent 20 ks observations were initiated in 2009 January and April (ObsIDs 9916 and 9917, PI: D. Weintraub). In addition, in 2008 November, two observations (ObsIDs 10763 and 8585; PI: N. Calvet) were made of the NGC 2068/2071 region that serendipitously included V1647 Ori. Together, these five CXO pointings yield an extended sequence of observations of this source over a seven-month period immediately following the onset of the optical outburst in 2008.

Fortuitously, a field of view that includes V1647 Ori was observed in 2002 November, a full year before the start of the 2003 outburst (Simon et al., 2004); subsequent CXO observations targeting V1647 Ori were obtained in 2004 March and April, 2005 August and December, and 2006 May and August (Kastner et al., 2004, 2006). In addition, targeted XMM-Newton observations were obtained in 2004 April (Grosso et al., 2005) and 2005 March (Grosso, 2006), and a targeted Suzaku observation was obtained in 2008 October (Hamaguchi et al., 2010). The 2004–2006 observations cover a two-year period during which V1647 Ori more or less faded steadily from a strong YSO X-ray source into a very faint one, albeit with large X-ray flux variability. For direct comparison with our analysis of the 2008–2009 epoch datasets, we have re-reduced and analyzed all of the 2002–2006 CXO datasets, using the same techniques

and software packages that we have used for the latest (2008–2009) datasets.

For all Chandra observations, the Advanced CCD Imaging Spectrometer (ACIS) was used in one of two imaging configurations. ACIS detectors have a pixel size of $0.49''$ and each ACIS-I and ACIS-S CCD has a field of view of $8.3' \times 8.3'$. CXO/ACIS has significant sensitivity over the energy range 0.3–10 keV, with the soft (<1 keV) X-ray sensitivity dependent on whether a back-illuminated or front-illuminated CCD serves as the detector (see below). The CIAO v4.1 software package and CALDB v4.1.0–4.1.4 calibration files were used to reduce the data and extract pulse-invariant (PI) spectra. Observation details are given in Table 1. To compare X-ray luminosities from 2008–2009 with those obtained from previous observations, source spectra were extracted from $2.5''$ radius regions (making sure the aperture was positioned so as to encompass as many source photons as possible, even when V1647 Ori is $4'$ off-axis) while background spectra were extracted from regions near but beyond $2.5''$ from the target, on the same chip, using $20''$ outer radius extraction apertures. Inspection of background light curves reveals background levels to be fairly constant with no evidence of large fluctuations, such as flares, occurring during the observations. Spectra were also re-extracted from previous Chandra observations using the same apertures to ensure that direct comparisons of results from different observation epochs could be performed reliably. For observations in which the primary target was not V1647 Ori (ObsIDs 2539, 10763, and 8585), exposure maps were generated to investigate off-axis position effects. In all three of these observations, the net count and mean count rate corrections due to off-axis source positions were insignificant, on the order of a few percent. The resultant spectral data points of the five recent observations

were grouped into energy bins with a minimum of five counts per bin before spectral modeling was done. The count rates were high enough and durations long enough for each of the 2008–2009 observations that this bin size yielded PI spectra with good statistics. For the 2002–2006 observations, we employed single-count-minimum binning for very low-count observations and five-count-minimum binning for higher-count observations so as to yield spectra suitable for modeling. Because no events with energies less than 0.5 keV and few events with energies greater than 8.0 keV were detected from V1647 Ori, we limited our modeling to the 0.5–8.0 keV energy range.

Table 1. 2002–2009 ACIS Observations of V1647 Ori.

| ObsID | Observation Date | JD | ACIS Chip | Exposure (ks) | Net Counts (0.5–8.0 keV) | Mean Count Rate ($ks^{-1}$) | Median Photon Energy (keV) | Mean Hardness[a] Ratio | Hardness Ratio[b] of Total Counts |
|---|---|---|---|---|---|---|---|---|---|
| 2539[c] | 2002 Nov 14 | 2452593 | S2 | 62.8 | 17 | $0.3 \pm 0.1$ | $2.0 \pm 0.3$ | $-0.34 \pm 0.31$ | $-0.28 \pm 0.28$ |
| 5307[d] | 2004 Mar 07 | 2453072 | S3 | 5.5 | 64 | $11.7 \pm 1.5$ | $3.6 \pm 0.3$ | $0.46 \pm 0.15$ | $0.45 \pm 0.14$ |
| 5308[d] | 2004 Mar 22 | 2453087 | S3 | 4.9 | 12 | $2.5 \pm 0.8$ | $2.0 \pm 0.5$ | $-0.45 \pm 0.33$ | $-0.46 \pm 0.33$ |
| 5382 | 2005 Apr 11 | 2453472 | I3 | 18.2 | 86 | $4.8 \pm 0.5$ | $3.5 \pm 0.1$ | $0.51 \pm 0.19$ | $0.46 \pm 0.12$ |
| 5383 | 2005 Aug 27 | 2453610 | I3 | 19.9 | 18 | $0.9 \pm 0.2$ | $3.0 \pm 0.8$ | $0.01 \pm 0.29$ | $0.34 \pm 0.25$ |
| 5384 | 2005 Dec 09 | 2453714 | I3 | 19.7 | 2 | $0.1 \pm 0.1$ | $2.2 \pm 1.1$ | $0.0 \pm 0.20$ | $-0.07 \pm 0.92$ |
| 6413 | 2005 Dec 14 | 2453719 | I3 | 18.1 | 4 | $0.2 \pm 0.1$ | $1.7 \pm 0.3$ | $-0.36 \pm 0.26$ | $-1.0 \pm 0.75$ |
| 6414 | 2006 May 01 | 2453857 | I3 | 21.6 | 3 | $0.1 \pm 0.1$ | $1.3 \pm 0.3$ | $0.09 \pm 0.23$ | $0.07 \pm 0.92$ |
| 6415 | 2006 Aug 07 | 2453955 | I3 | 20.5 | 4 | $0.2 \pm 0.1$ | $2.4 \pm 0.4$ | $-0.27 \pm 0.21$ | $-1.0 \pm 0.73$ |
| 9915 | 2008 Sep 18 | 2454728 | I3 | 19.9 | 466 | $23.6 \pm 1.1$ | $3.5 \pm 0.1$ | $0.36 \pm 0.07$ | $0.37 \pm 0.05$ |
| 10763[c] | 2008 Nov 27 | 2454798 | I2 | 19.7 | 217 | $11.0 \pm 0.7$ | $3.9 \pm 0.1$ | $0.65 \pm 0.09$ | $0.64 \pm 0.08$ |
| 8585[c] | 2008 Nov 28 | 2454799 | I2 | 28.5 | 160 | $5.8 \pm 0.4$ | $3.4 \pm 0.1$ | $0.40 \pm 0.10$ | $0.43 \pm 0.09$ |
| 9916 | 2009 Jan 23 | 2454855 | I3 | 18.4 | 245 | $13.6 \pm 0.9$ | $3.7 \pm 0.2$ | $0.41 \pm 0.08$ | $0.43 \pm 0.07$ |
| 9917 | 2009 Apr 21 | 2454943 | I3 | 29.8 | 260 | $8.8 \pm 0.5$ | $3.5 \pm 0.2$ | $0.28 \pm 0.08$ | $0.37 \pm 0.07$ |

[a]Average of hardness ratios computed from 2 ks light curve data bins (ObsID 2539 uses 10 ks light curve data bins).

[b]Hardness ratio computed using the total numbers of hard and soft X-ray photons from the entire observation.

[c]V1647 Ori was not the target of the observation, and given values have been adjusted to compensate for the $4'$ off-axis position of V1647 Ori. Exposure maps indicated net counts and mean count rates for ObsID 2539 should be increased by 8% while those for ObsIDs 10763 and 8585 required a 3% increase.

[d]The back-illuminated ACIS-S3 CCD is more sensitive to X-rays from plasma in the temperature regime characteristic of V1647 Ori than are the front-illuminated ACIS CCDs. Values displayed for net counts and mean count rates, and their associated errors, for ObsIDs 5307 and 5308 have been adjusted downward by 10%, based on spectral simulations in order to make net counts and mean count rates directly comparable between all chips.

Note. — All errors are $1\sigma$. The net counts for each observation are the total number of counts within the 0.5–8.0 keV range. Median photon energy uncertainties were calculated via the half-sample method used in Kastner et al. (2006). Mean count rates were determined by dividing the net counts by exposure times. Uncertainties for mean count rates and hardness ratios of total counts follow Poisson statistics. The uncertainty for the hardness ratio of the total counts for ObsID 5384 could not be calculated due to the even distribution of the very low number of counts

Since V1647 Ori was imaged with both front- and back-illuminated CCDs in the exposure sequence under analysis, we generated synthetic spectra and convolved these spectra with the instrument responses to determine whether mean, broadband (0.5–8.0 keV) count rates were directly comparable for all observations of V1647 Ori. The simulations (Table 2) showed that, for the plasma temperature regimes considered here, the back-illuminated S3 CCD is $\sim$10% more sensitive to incoming flux than the front-illuminated ACIS-I CCDs. Net counts and mean count rates in the energy range 0.5–8.0 keV (Table 1) were therefore adjusted downward accordingly for the two observations (ObsIDs 5307 and 5308) that used the S3 CCD in order to remove this sensitivity bias.

Table 2. Comparison of Simulated Front- and Back-Illuminated ACIS Chip Exposures

| Plasma Temperature (kev) | S3/I3 Count Ratio | S3 HR | I3 HR | HR Difference |
|---|---|---|---|---|
| 2 | 1.21 | 0.02 | 0.12 | 0.10 |
| 5 | 1.14 | 0.30 | 0.38 | 0.08 |
| 7 | 1.11 | 0.40 | 0.48 | 0.08 |

Note. — Net count and hardness ratio (of total counts) comparisons for simulated spectra convolved with instrument responses from ObsIDs 5307 and 9915, which used the back-illuminated S3 CCD and front-illuminated I3 CCD, respectively. Each of the 1-ks spectra were simulated using the *fakeit* command in XSPEC with the intervening hydrogen column density and chemical abundance fixed at $4.0 \times 10^{22}$ cm$^{-2}$ and 0.8 solar, respectively. The front-illuminated chip detects roughly 85% of the net counts of the back-illuminated chip, with a greater drop in sensitivity for soft versus hard X-rays.

## 4.3 Results

### 4.3.1 Short-Term and Long-Term Variability

We calculated the median photon energies, mean count rates, and mean hardness ratios for all 14 CXO observations of V1647 Ori. These results are reported in Table 1. In calculating the hardness ratios, the hard (H) X-rays are defined as those in the range from 2.8 to 8.0 keV and the soft (S) X-rays as those with energies from 0.5 to 2.8 keV (Grosso et al., 2005). The hardness ratio is then HR = (H-S)/(H+S), such that negative values of HR indicate softer spectra, and positive values indicate harder spectra. The recalculated values and error ranges of the mean count rates and median photon energies for the 2004–2006 observations differ only marginally from those reported by Kastner et al. (2006). With data from only three epochs in hand, Kastner et al. (2004) reported that the X-ray flux brightened and hardened during the outburst (2002 November 14 to 2004 March 07) and then quickly faded and softened post-outburst (2004 March 07 to 2004 March 22). With data from additional epochs available, however, Kastner et al. (2006) reinterpreted the late 2004 March data as a short-term downward fluctuation, not as a quick end to the original outburst. They interpret the observed pattern of changes in the median photon energy as evidence that the X-ray spectrum hardened during outburst, remained somewhat hard for at least one year, and then softened after 2005 August 27 as both the optical and X-ray flux from V1647 Ori returned to pre-outburst levels. The results obtained here (for hardness ratio) confirm this general trend. This hardening and softening (the mean hardness ratios (with $1\sigma$ uncertainties) changed from $-0.34 \pm 0.31$ (soft) to $+0.46$

$\pm$ 0.15 (hard) and back to $-0.45 \pm 0.33$ (very soft) over the course of three years, from 2002 November through 2005 December) took place over a timescale of months, with V1647 Ori remaining near peak outburst X-ray luminosity and hardness for more than one year - with the notable exception of the 2004 March 22 data. V1647 Ori likely remained in its soft X-ray, low X-ray luminosity phase for almost three years, from late 2005 until its latest optical outburst in 2008 August. The five CXO observations covering the interval from 2008 September through 2009 April all show V1647 Ori in a hard X-ray, high X-ray luminosity state. As was the case during the 2002–2006 observations, the source remained near peak X-ray luminosity for at least seven months (Fig. 22, figure to be discussed in Section 4.4). As of 2009 December 18, V1647 Ori appeared to still be in an outburst phase with J-, H-, and K-band photometric magnitudes near values measured at the brightest phase of outburst during 2008 September (Venkat & Anandarao, 2009). Thus, it appears that V1647 Ori remained near peak luminosity for at least one year.[4]

X-ray light curves and hardness ratios as a function of time were extracted for each observation to examine the properties of any possible short-term X-ray variability. In particular, these time series data permit us to investigate whether the trends in X-ray flux and hardness ratio seen in 2002–2006 were repeated during the recent outburst that began around 2008 August. The extracted X-ray light curves and hardness ratio time series for six of the nine observations from 2002–2006 are presented in Figure 12. X-ray light curves and hardness ratio curves for the five 2008–2009 Chandra observations are presented in Figures 13–17, which show (from top to bottom) the

[4]As of submission of this paper, the outburst appears to be ongoing.

overall X-ray light curve, the soft (0.5–2.8 keV) light curve, the hard (2.8–8.0 keV) light curve, and the hardness ratio time series. Energy ranges for the soft and hard X-ray bands follow those defined in Grosso et al. (2005), and plotted uncertainties in mean hardness ratios and count rates are $1\sigma$.

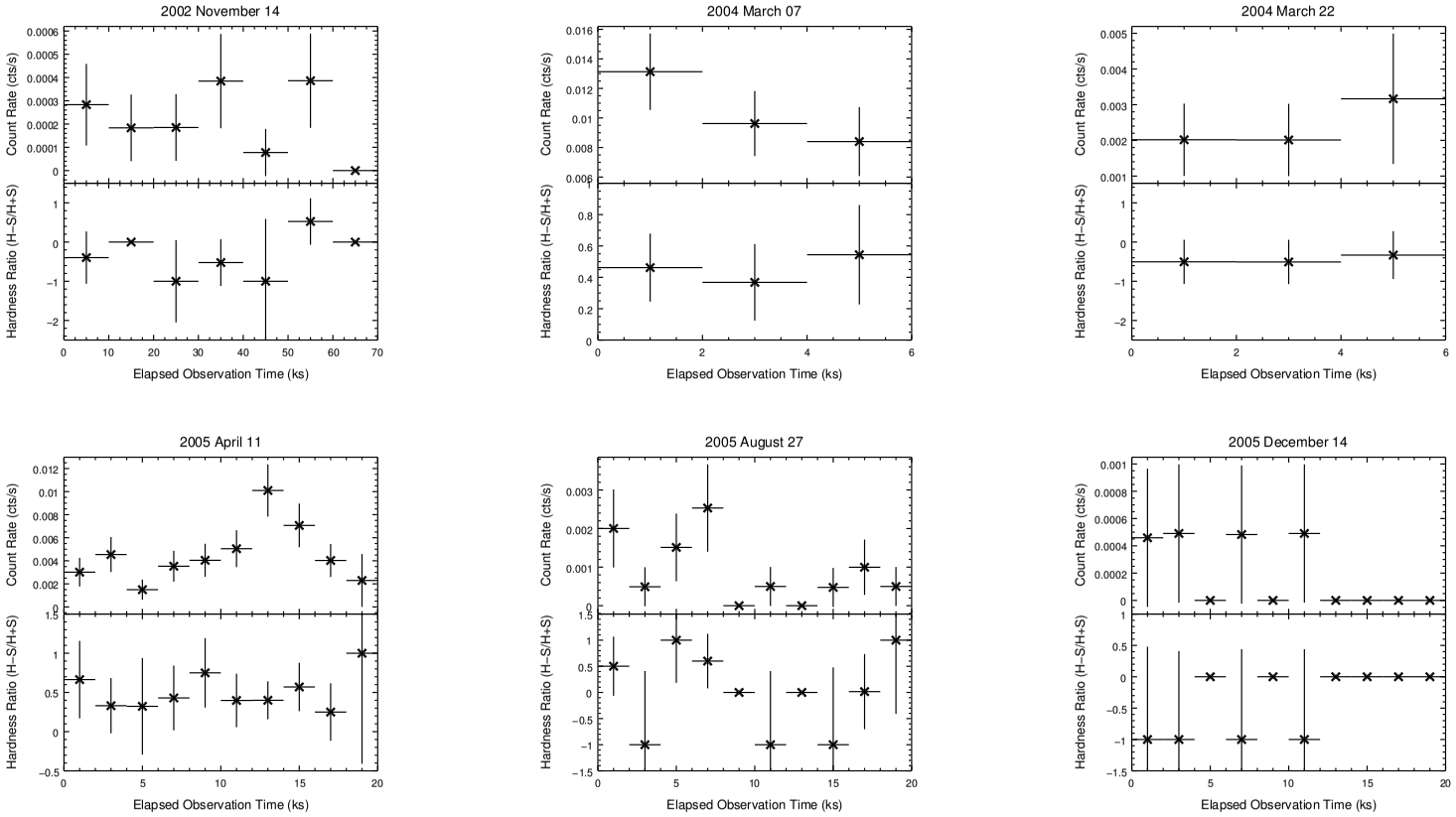


Figure 12: Background-subtracted X-ray light curves for 2002-2006 epoch observations. Time bins are 2 ks for each observation (except 2002 November 14, which uses 10 ks bins due to the very low count rate) and contain counts (0.5–8.0 keV) per total time associated with each bin, not the total time associated with the observation. Observations for 2005 December 09, 2006 May 01, and 2006 August 07 do not detect V1647 Ori, so their light curves are not presented. Uncertainties in mean hardness ratios and count rates are $1\sigma$.

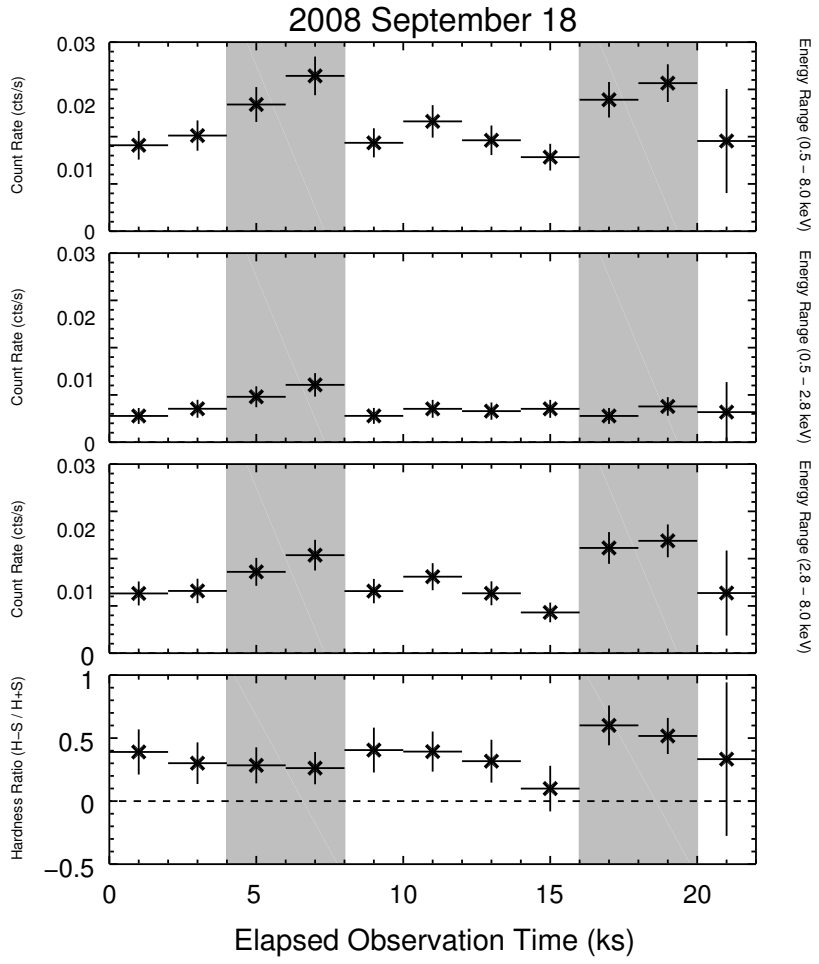


Figure 13: X-ray light curves and hardness ratio of V1647 Ori during observation 9915. The top panel light curve covers the 0.5–8.0 keV energy range, the second panel down spans the lower energy range of 0.5–2.8 keV, and the third panel down covers the higher 2.8–8.0 keV energies. The bottom panel displays the hardness ratio for each of the bins. Counts were binned into 2 ks bins. Uncertainties in mean hardness ratios and count rates are $1\sigma$. Apparent "X-ray bright" time intervals are indicated by the shaded regions in the figure (4–8 ks and 16–20 ks) and in Figures 14–17.

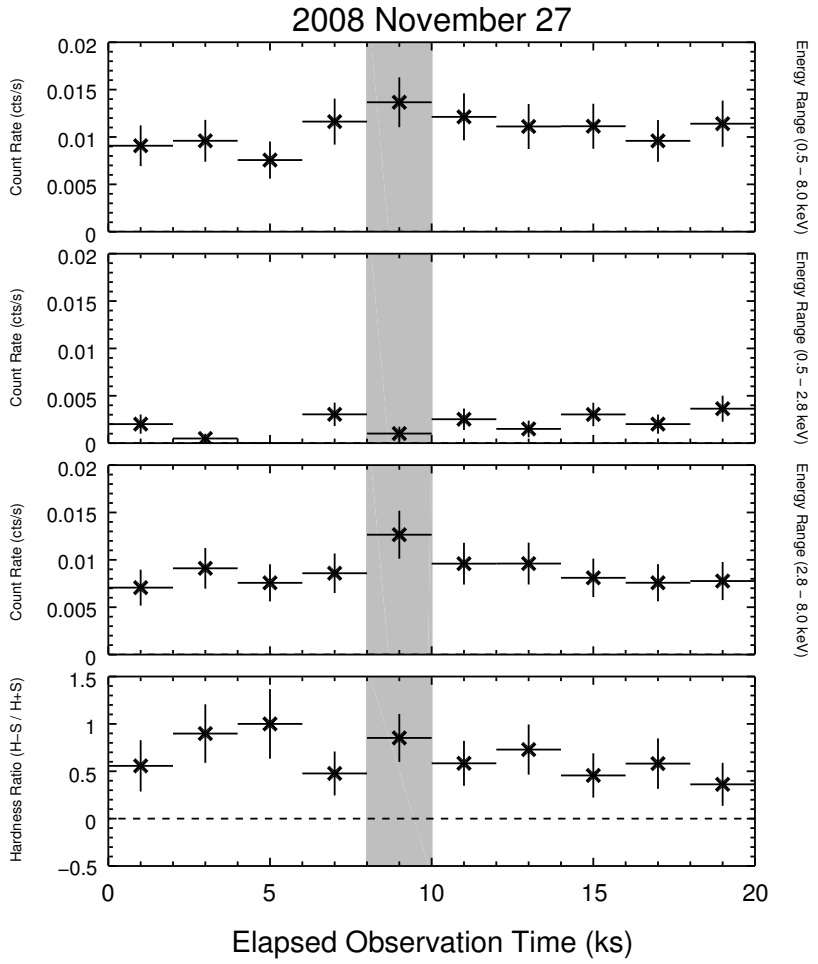


Figure 14: X-ray light curves and hardness ratio of V1647 Ori during observation 10763. See Figure 13 for description of panels. Counts were binned into 2 ks bins. Uncertainties in mean hardness ratios and count rates are $1\sigma$. V1647 Ori had a slightly elevated X-ray flux, seen best in the hard X-ray band, from 8–10 ks.

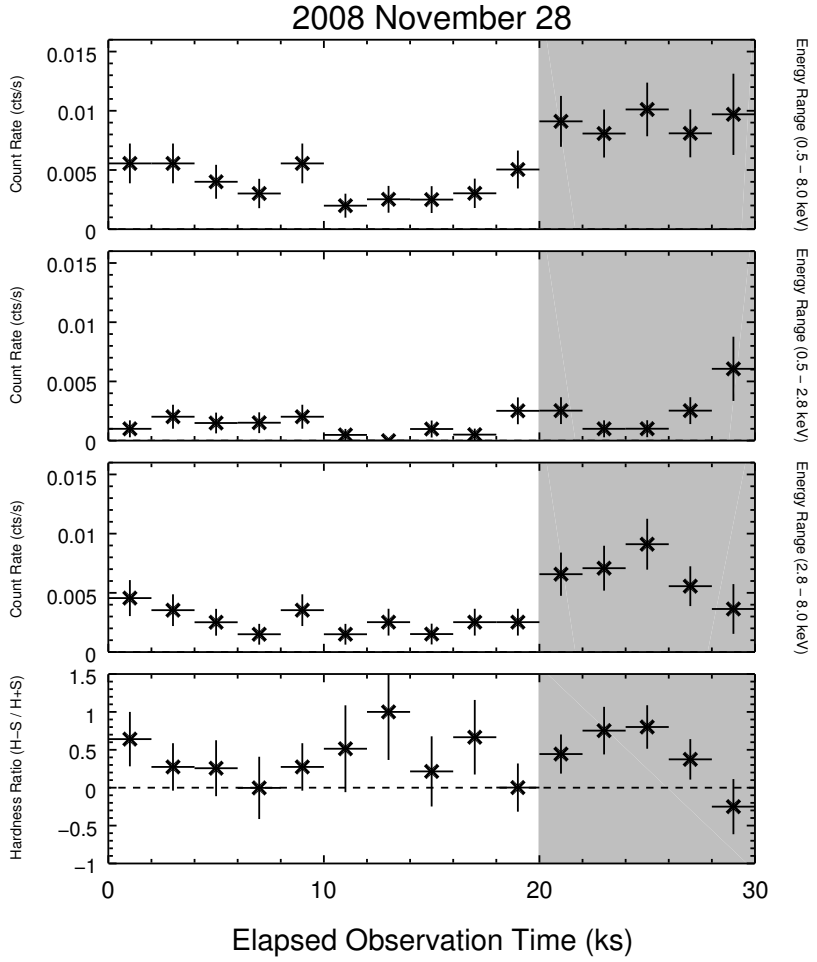


Figure 15: X-ray light curves and hardness ratio of V1647 Ori during observation 8585. Counts were binned into 2 ks bins. Uncertainties in mean hardness ratios and count rates are $1\sigma$. The hard and broad-band X-ray light curves show that the hard X-ray flux from V1647 Ori increased sharply at 20 ks into the observation and remained elevated for $\sim$10 ks. During this period of elevated X-ray flux, the soft-band flux remained more or less constant.

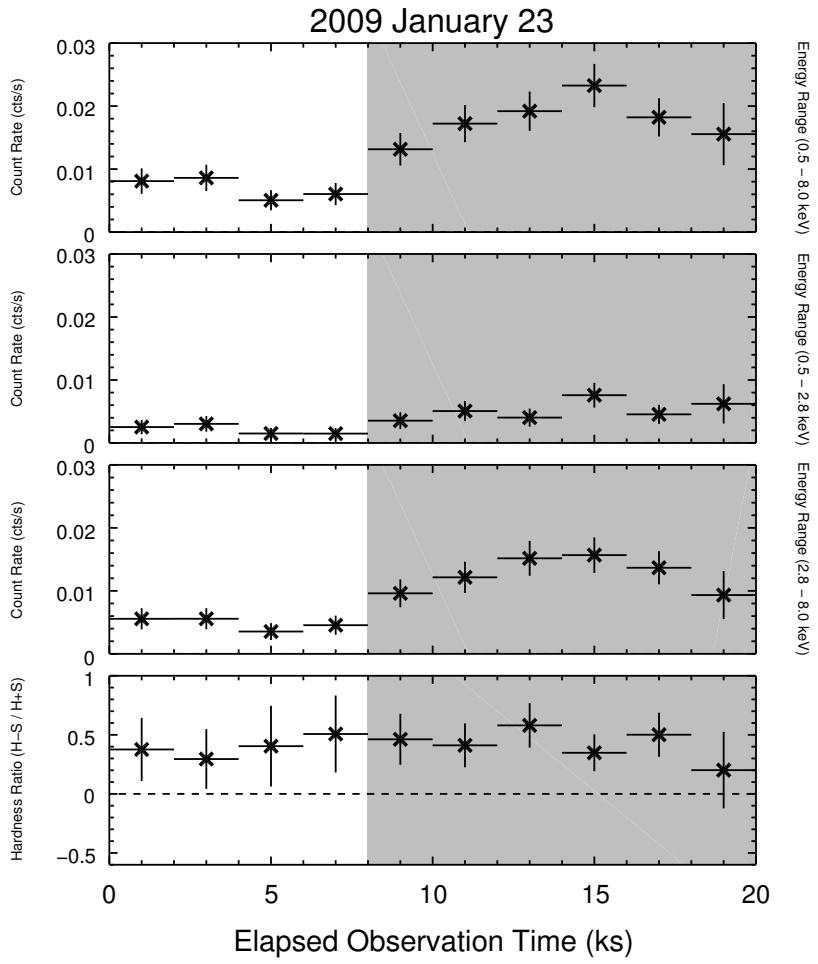


Figure 16: X-ray light curves and hardness ratio of V1647 Ori during observation 9916. Counts were binned into 2 ks bins. Uncertainties in mean hardness ratios and count rates are $1\sigma$. The X-ray light curve shows that V1647 Ori began increasing in hard-band and, possibly, soft-band flux about 8 ks into the observation, and the flux remained elevated for $\sim$12 ks.

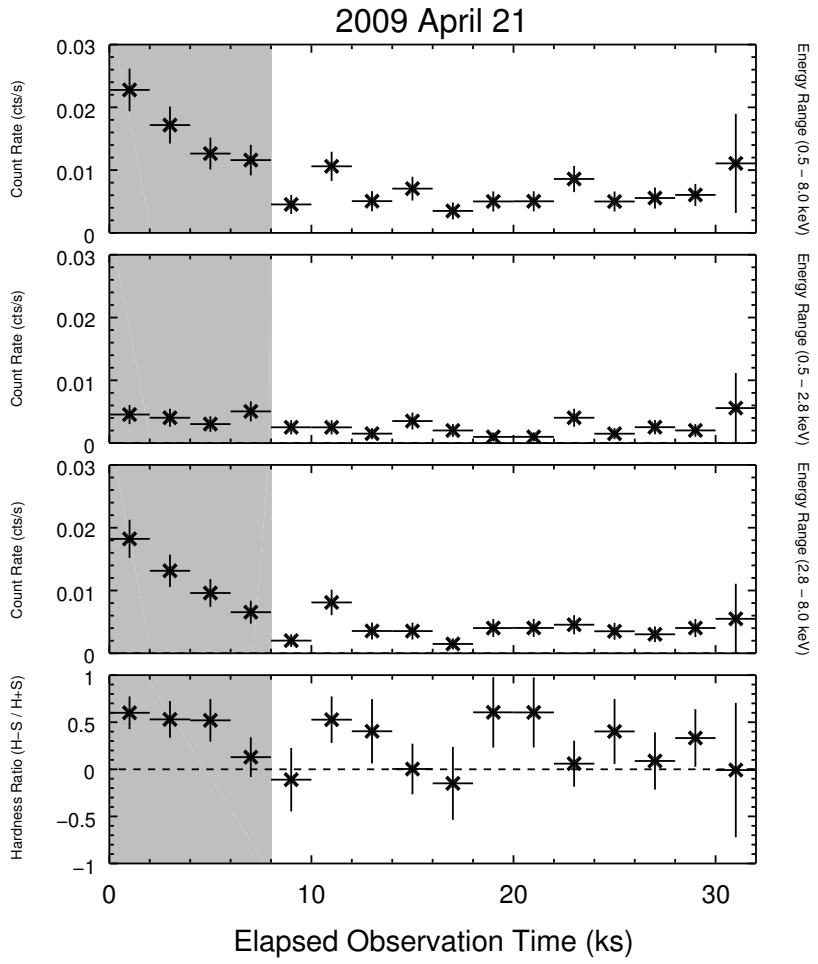


Figure 17: X-ray light curves and hardness ratio of V1647 Ori during observation 9917. Counts were binned into 2 ks bins. Uncertainties in mean hardness ratios and count rates are $1\sigma$. V1647 Ori appeared to be in an elevated hard X-ray flux state at the onset of the observation, with the X-ray count rate remaining elevated for $\sim$8 ks.

The X-ray count rate for V1647 Ori was intrinsically lower during most of the 2002-2006 observations (the count rate was >5 $ks^{-1}$ only on 2004 March 07) than in 2008–2009 (the count rate was >5 $ks^{-1}$ during all five observations). Also, in some cases like ObsIDs 5307 and 5308 (both from 2004), the observations were on the order of only a few kiloseconds in duration. The low count rates in most of the 2002–2006 data and the short exposure times in two of these observations make comparisons with the more recent datasets, in terms of the presence or absence of 2–10 ks timescale variations, fairly difficult. However, observations 5382 and 5383, obtained in 2005 April and August, respectively – more than a year after the initial optical outburst of V1647 Ori in 2003 November – yielded enough counts that we can compare these two light curves with the more recent observations with some confidence. As seen in these two light curves from 2005 (Fig. 12, lower-left panel, beginning at ∼10 ks, and lower-middle panel, beginning at ∼5 ks), the X-ray count rate again varied by a factor of ∼4 on a timescale of 2–10 ks, a level and duration of short-term variability very similar to that seen in the more recent (2008–2009) observations. We conclude that kilosecond-timescale variations are seen in all observations of V1647 Ori in which the signal is strong enough and the observing window long enough for us to search for such events, and that the amplitude duty cycle and duration of these few-kilosecond X-ray variations were stable over the five-year period from 2005 to 2009. Such variability appears to be part of the normal X-ray pattern for this object, at least when the count rate is elevated. One therefore needs to interpret the overall flux levels observed during the 2004 March 07 and 2004 March 22 observations, which, respectively, are only 5.5 ks and 4.9 ks in duration, with caution.

The highest measured X-ray mean count rate following the latest (2008) optical outburst of V1647 Ori is higher (23.6 $ks^{-1}$; one month post-outburst) than the highest level (11.7 $ks^{-1}$; four months post-outburst) observed during its 2003–2005 outburst (Table 1). In addition, with the exception of the 2004 March 07 observation, the 2008–2009 observations (a period spanning seven months) show V1647 Ori to be consistently brighter than it was during the 2003–2005 outburst. We find that in 2008–2009 the X-ray spectrum stays relatively hard, as is shown by the median photon energies, which in 2008–2009 are consistently about twice the energy (3.4 to 3.9 keV) that was observed before the first eruption (2.0 keV in 2002) and after V1647 Ori had returned to its quiescent state in late 2005 (1.7 keV). Also, while the mean hardness ratios were negative both before (2002 November) and after (2005 December) the first eruption, the mean hardness ratios in 2008–2009 stay consistently around $\sim$0.3 or greater.

These results also reveal that V1647 Ori exhibited a very interesting sequence of changes of state, beginning in 2004 March. V1647 Ori had switched from its elevated state on 2004 March 07 (11.7 counts $ks^{-1}$, median photon energy of 3.6 keV, mean hardness ratio of +0.46) to what appears to be a quiescent state on 2004 March 22 (2.5 cts $ks^{-1}$, median photon energy of 2.0 keV, $-0.45$ mean hardness ratio) but then was again in an elevated state one year later on 2005 April 11 (4.8 cts $ks^{-1}$, median photon energy of 3.5 keV, mean hardness ratio of +0.51). Yet by 2005 August 27, V1647 Ori was again returning to quiescence (0.9 cts $ks^{-1}$, 3.0 keV median photon energy, +0.01 mean hardness ratio) and by 2005 December was fully back to quiescence.

At least three explanations are plausible for the observed changes we have de-

scribed in the X-ray emission from V1647 Ori that occurred between 2004 March 07 and 2004 March 22 and between 2004 March 22 and 2005 April 11. One: the outbursts generate both hard and soft X-rays; most of the time (2004 March 07 and 2005 April 11), the hard X-ray plasma is dominant in the X-ray spectrum as observed by CXO, but at certain times (2004 March 22) the soft X-ray plasma component is seen more clearly. Two: the first major outburst (2003 November through early 2004 March) had ended, at least in the X-ray regime, after only a few months. By 2005 April, the source was again in an elevated state and by 2005 August, four months later, was again returning to quiescence. Three: the 2004 March 22 observation caught V1647 Ori during a short duration (2–10 ks) quiescent moment during the extended (months long) outburst phase. However, the XMM-Newton observation obtained on 2004 April 4 showed a low X-ray flux level at the beginning of the observation that is consistent with the quiescent level observed by CXO that increased in the second part of the observation (Grosso et al., 2005). Moreover, the supporting evidence from observations made at optical and near-infrared wavelengths for the first outburst ending in 2004 mid-March and for a second outburst beginning later that year (explanation "Two") is weak, at best. Of the remaining two possibilities, we will argue in §4 that explanation "One" is more likely.

A comparison of the count rates (Figs. 13–17, top panels) and hardness ratios (Figs. 13–17, bottom panels) during the ∼2–10 ks variability periods suggests that the X-ray spectrum of V1647 Ori may harden as it brightens and soften as the source fades during these few-kilosecond variations. This appearance of a correlation between the changing count rate and the changing hardness ratio on a few kilosecond timescale

during short-term variability, however, is not consistent. In fact, we find a weak anti-correlation between these properties (correlation coefficient = $-0.18$) on these short timescales; however, we do find a strong, positive correlation over much longer periods of time between the X-ray luminosity (calculated in our spectral modeling; see Section 4.3.2) and hardness ratio, as shown in Figure 18. In this figure, the top panels show the seven-year X-ray luminosity curve of V1647 Ori while the middle panels show the corresponding hardness ratios with a single, average measurement plotted for each observation epoch. A more direct demonstration of this correlation is shown in Figure 19 where we plot the change in mean hardness ratio versus the change in X-ray luminosity between observations of V1647 Ori. We derive a correlation coefficient of 0.44 for these two parameters.

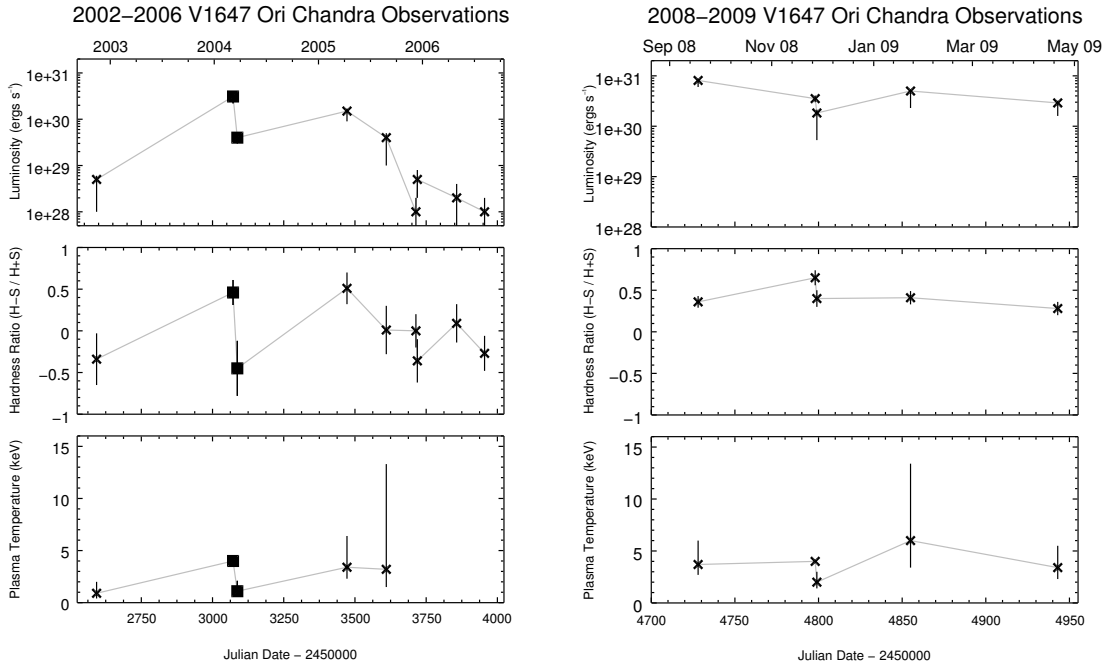


Figure 18: Time series of observed X-ray luminosity (top panels), mean hardness ratio (middle panels), and plasma temperature (bottom panels) for V1647 Ori. Crosses represent data obtained with ACIS front-illuminated CCDs, and squares represent data obtained with the ACIS back-illuminated S3 CCD. Plotted uncertainties for the hardness ratios and luminosities represent the 68% confidence interval ($1\sigma$) and plotted uncertainties for the plasma temperatures represent the 90% confidence interval ($1.6\sigma$). The modeled plasma temperatures for the 2005 December through 2006 May observations are not shown because this parameter was not well constrained by spectral fitting.

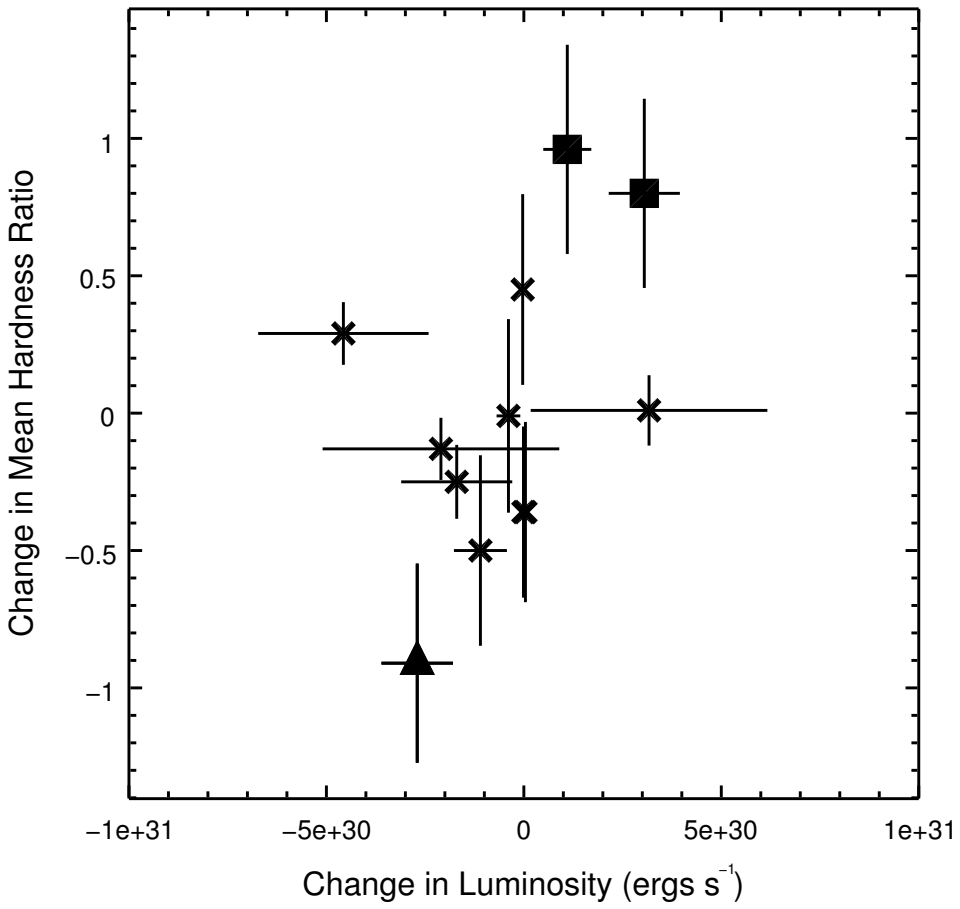


Figure 19: Two-parameter plot for all CXO observations of V1647 Ori showing the correlation between the changes in mean hardness ratios of individual observations and the changes in observed X-ray luminosities. Crosses represent values corresponding to data obtained with ACIS front-illuminated CCDs, squares represent values involving data obtained with ACIS front-illuminated CCDs and the back-illuminated S3 CCD, and the triangle represents a value that used back-illuminated S3 CCD data only. The correlation coefficient for the changes in mean hardness ratio and changes in observed X-ray luminosity is 0.44.

As seen in the top and middle left-hand panels of Figure 18, from the first Chandra observation in 2002 to the first observation of V1647 Ori in 2004, the luminosity increased by $\sim$2 orders of magnitude while the mean hardness ratio increased from a relatively soft value of $-0.34$ to a hard value of 0.46. From the second to the third observation, the X-ray luminosity dropped by an order of magnitude while the mean hardness ratio softened to a much lower value of $-0.45$, much lower than that seen in the 2002 observation of V1647 Ori when it was seen to be in quiescence. When the fourth Chandra observation occurred in 2005, the luminosity had risen back to outburst levels again while the mean hardness ratio increased again to $+0.51$, the highest observed to that date. In subsequent Chandra observations through early 2006, the X-ray luminosity of V1647 Ori diminished while the hardness ratio dropped.

In the top and middle righthand panels of Figure 18, we present the X-ray luminosity and mean hardness ratio versus time for most recent Chandra observations of V1647 Ori. The same correlation between changes in X-ray luminosity and changes in the mean hardness ratio seen in the 2002 through 2006 observations is evident in all observations from 2008 through 2009. From 2008 September 18 to 2008 November 27, there appears to be an anti-correlation with the luminosity decreasing slightly between these observations while the hardness ratio increases. We note, though, that in both of these epochs, the luminosity is high and the spectrum is quite hard. Since the short-period light curves of each observation show that there is typically X-ray variability on timescales of kiloseconds, with X-ray flux sometimes increasing by several factors, this apparent anti-correlation might be attributed to short-duration variability.

These results suggest that we can identify two states for V1647 Ori, as seen in time-averaged data on a 5–30 ks timescale:

- In its *quiescent* state, V1647 Ori has a low count rate ($<$1 ct ks$^{-1}$), low median photon energy ($\lesssim$2.5 keV), and negative (soft X-ray dominated) hardness ratio.
- In its *elevated* state, the count rate is at least 25–50 times greater, the median photon energy doubles, and the hardness ratio becomes strongly positive (hard X-ray dominated).

The X-ray evidence shows that when V1647 Ori enters a major optical/near-infrared outburst, the X-ray profile switches from quiescent to elevated, and when the outburst phase ends, the X-ray profile switches from elevated to quiescent.

### 4.3.2 Spectral Modeling

**Procedure & Results** Modeling of the spectra employed XSPEC v12.4. For those spectra with single-count binning, XSPEC was set to use the Cash-statistic instead of the $\chi^2$ statistic to assess the goodness of fit. All models at first assumed a thin, single-temperature plasma (APEC model) subject to absorption by an intervening column of hydrogen (WABS component). From the 2004 April XMM-Newton observations, single-component thermal plasma models of the V1647 X-ray spectrum yield a hydrogen column density, chemical abundance, and plasma temperature of $N_H = 4.1\times10^{22}$ cm$^{-2}$, Z = 0.8 solar, and $kT_X = 4.2$ keV, respectively (Grosso et al., 2005), and recent Suzaku observations yield similar results (Hamaguchi et al., 2010). Therefore, initially, $N_H$, Z, and $kT_X$ were set approximately to the aforementioned

values ($N_H = 4.0 \times 10^{22}$ cm$^{-2}$, Z = 0.8 solar, and $kT_X = 4.0$ keV). As our initial test indicated that Z is poorly constrained by the Chandra data, only $N_H$ and $kT_X$ were left free to vary during the fitting procedure. For four of the five 2008–2009 observations, the models converged to best-fit solutions with column density and plasma temperature within a 90% confidence interval of their initial values; however, the 2008 November 27 spectrum model was unable to converge to a physically-meaningful fit, so the plasma temperature was fixed at $kT_X = 4.0$ keV (Table 3).

A similar fitting method was used for the 2002–2006 observations (Table 4). Initially, the first five of these spectra spectra were modeled with freely varying hydrogen column densities and plasma temperatures, while the chemical abundance was fixed at 0.8 solar. These spectral models, however, were unable to constrain plasma temperatures or X-ray fluxes and luminosities, so the hydrogen column density was then fixed at $N_H = 4.1 \times 10^{22}$ cm$^{-2}$, and the models were refit. The remaining four spectra, obtained when V1647 Ori was reverting to an optical/X-ray quiescent state, were modeled with the hydrogen column density and plasma temperature fixed at $N_H = 4.1 \times 10^{22}$ cm$^{-2}$ and $kT_X = 0.86$ keV, respectively. Given the small number of counts in these four spectra, the associated error ranges for these X-ray fluxes and luminosities were obtained by multiplying the error ranges for the mean count rates of these observations with an appropriate energy conversion factor (ECF), where the ECF for each observation epoch was obtained by dividing the derived X-ray flux by the mean count rate.

Table 3. Model Fits for 2008–2009 Chandra Observations of V1647 Ori.

| ObsID | Observation Date | Reduced $\chi^2$ | Degrees of Freedom | $N_H$ ($\times 10^{22}$ cm$^{-2}$) | $kT_X$ (keV) | EM ($\times 10^{53}$ cm$^{-3}$) | Observed $F_X$ ($\times 10^{-13}$ ergs cm$^{-2}$ s$^{-1}$) | Observed $L_X$ ($\times 10^{30}$ ergs s$^{-1}$) |
|---|---|---|---|---|---|---|---|---|
| 9915 | 2008 Sep 18 | 0.85 | 77 | $4.1^{+0.9}_{-0.7}$ | $3.7^{+2.3}_{-1.0}$ | $15.0^{+6.3}_{-4.4}$ | $4.2^{+0.3}_{-1.1}$ | $8.1^{+0.5}_{-2.1}$ |
| 10763 | 2008 Nov 27 | 1.24 | 39 | 4.1 (Fixed) | 4.0 (Fixed) | $6.1^{+0.8}_{-0.8}$ | $1.8^{+0.3}_{-0.3}$ | $3.5^{+0.5}_{-0.5}$ |
| 8585 | 2008 Nov 28 | 0.71 | 26 | $5.9^{+2.4}_{-1.4}$ | $2.0^{+1.0}_{-0.6}$ | $8.2^{+9.5}_{-3.7}$ | $1.0^{+0.1}_{-0.7}$ | $1.8^{+0.3}_{-1.3}$ |
| 9916 | 2009 Jan 23 | 0.79 | 42 | $4.1^{+1.1}_{-0.8}$ | $6.0^{+7.4}_{-2.6}$ | $6.8^{+3.5}_{-1.6}$ | $2.6^{+0.2}_{-1.4}$ | $5.0^{+0.3}_{-2.7}$ |
| 9917 | 2009 Apr 21 | 0.88 | 44 | $4.1^{+1.3}_{-0.9}$ | $3.4^{+2.1}_{-1.1}$ | $5.9^{+4.1}_{-2.0}$ | $1.5^{+0.2}_{-0.7}$ | $2.9^{+0.3}_{-1.3}$ |

Note. — Uncertainties given for hydrogen column density, plasma temperature, and chemical abundance correspond to the 90% confidence intervals, whereas the observed X-ray luminosities are given with their corresponding 68% confidence intervals. Chemical abundance was fixed at 0.8 solar. For ObsID 10763, in order to constrain the observed X-ray flux and luminosity, the hydrogen column density and plasma temperature were fixed at the given values. Emission measures and luminosities assume a distance of 400 pc to V1647 Ori.

Table 4. Model Fits for 2002–2006 Chandra Observations of V1647 Ori.

| ObsID | Observation Date | Reduced Statistic | Degrees of Freedom | $kT_X$ (keV) | EM ($\times 10^{53}$ cm$^{-3}$) | Observed $F_X$ ($\times 10^{-13}$ ergs cm$^{-2}$ s$^{-1}$) | Observed $L_X$ ($\times 10^{30}$ ergs s$^{-1}$) |
|---|---|---|---|---|---|---|---|
| 2539 | 2002 Nov 14 | 1.37 | 13 | $0.9^{+1.1}_{-0.5}$ | $0.6^{+1.9}_{-0.6}$ | $0.03^{+0.01}_{-0.02}$ | $0.05^{+0.01}_{-0.04}$ |
| 5307 | 2004 Mar 7 | 1.19[a] | 10 | 4.0 (F) | $5.4 \pm 1.3$ | $1.6 \pm 0.5$ | $3.1 \pm 0.9$ |
| 5308 | 2004 Mar 22 | 1.45 | 10 | $1.1^{+1.0}_{-0.5}$ | $3.9^{+6.9}_{-3.9}$ | $0.2 \pm 0.1$[b] | $0.4 \pm 0.1$ |
| 5382 | 2005 Apr 11 | 0.98[a] | 14 | $3.4^{+3.0}_{-1.1}$ | $3.1^{+1.2}_{-1.0}$ | $0.8^{+0.1}_{-0.3}$ | $1.5^{+0.2}_{-0.6}$ |
| 5383 | 2005 Aug 27 | 1.99 | 16 | $3.2^{+10.1}_{-1.7}$ | $0.8^{+0.8}_{-0.4}$ | $0.2^{+0.1}_{-0.2}$ | $0.4^{+0.1}_{-0.3}$ |
| 5384 | 2005 Dec 9 | 1.67 | 1 | 0.86 (F) | $0.2^{+0.6}_{-0.2}$ | $0.01 \pm 0.01$[b] | $0.01 \pm 0.01$ |
| 6413 | 2005 Dec 14 | 0.87 | 3 | 0.86 (F) | $0.9^{+0.8}_{-0.5}$ | $0.02 \pm 0.01$[b] | $0.05 \pm 0.03$ |
| 6414 | 2006 May 1 | 2.83 | 2 | 0.86 (F) | $0.3^{+0.6}_{-0.3}$ | $0.01 \pm 0.01$[b] | $0.02 \pm 0.02$ |
| 6415 | 2006 Aug 7 | 1.45 | 3 | 0.86 (F) | $0.9^{+0.6}_{-0.3}$ | $0.01 \pm 0.01$[b] | $0.01 \pm 0.01$ |

[a] Value is the reduced-$\chi^2$ value.

[b] Observed X-ray flux errors and corresponding X-ray luminosity errors were derived by multiplying the mean count rate errors from Table 1 by an energy conversion factor (ECF).

Note. — Uncertainties given for hydrogen column density and plasma temperature correspond to the 90% confidence intervals, whereas the observed X-ray luminosities are given with their corresponding 68% confidence intervals. All models use a fixed hydrogen column density of $N_H = 4.1 \times 10^{22}$ cm$^{-2}$ and a chemical abundance fixed at 0.8 solar. For ObsID 5307, the plasma temperature was fixed ("F") at a typical post-outburst plasma temperature of $kT_X = 4.0$ keV in order to constrain the remaining model parameters. For ObsIDs 5384, 6413, 6414, and 6415, the very low number of counts did not permit spectral fitting with freely-varying plasma temperature, so the plasma temperature was fixed at a pre-outburst value as discussed in Kastner et al. (2004). Observed fluxes and emission measures were derived from the resulting model fits, an energy conversion factor (ECF) was calculated for each observation, and the mean count rate uncertainties were multiplied with the ECF to better constrain the source fluxes displayed. All models, unless otherwise noted, use the Cash statistic to determine goodness of fit, and the reduced statistic is the Cash-statistic or $\chi^2$ value divided by the number of degrees of freedom. Emission measures and observed luminosities assume a distance of 400 pc to V1647 Ori.

For the CXO observations of V1647 Ori with sufficient total counts (ObsIDs 9915 and 9917), we performed fits of a two-component thermal plasma model with parameters for hydrogen column density set to $4.0 \times 10^{22}$ cm$^{-2}$, plasma temperatures set to $kT_X = 0.5$ keV and 2.0 keV, and chemical abundance fixed at 0.8 solar. Visual inspection of the spectral models shows that there is a negligible difference between the best-fit single- and two-component models, F-test results suggest that there is no statistical improvement in the model fits with the addition of a second plasma component; i.e., the best-fit parameters for the latter model converge on values such that the contribution of the lower-temperature component is negligible. We conclude, therefore, that all of the 2008–2009 CXO data are best fit with a single-component model.

Best-fit models for each of the five recent Chandra observations are shown in Figure 20. The overall trend of the spectral models is to converge to fits with parameters similar to those of the best-fit single-component model reported by Grosso et al. (2005). Intervening hydrogen column densities do vary from model to model but remain in the $N_H \sim 4$–$6 \times 10^{22}$ cm$^{-2}$ range, and plasma temperatures are $kT_X \sim 2$–6 keV, slightly higher than but still within the range of uncertainty found by Kastner et al. (2006).

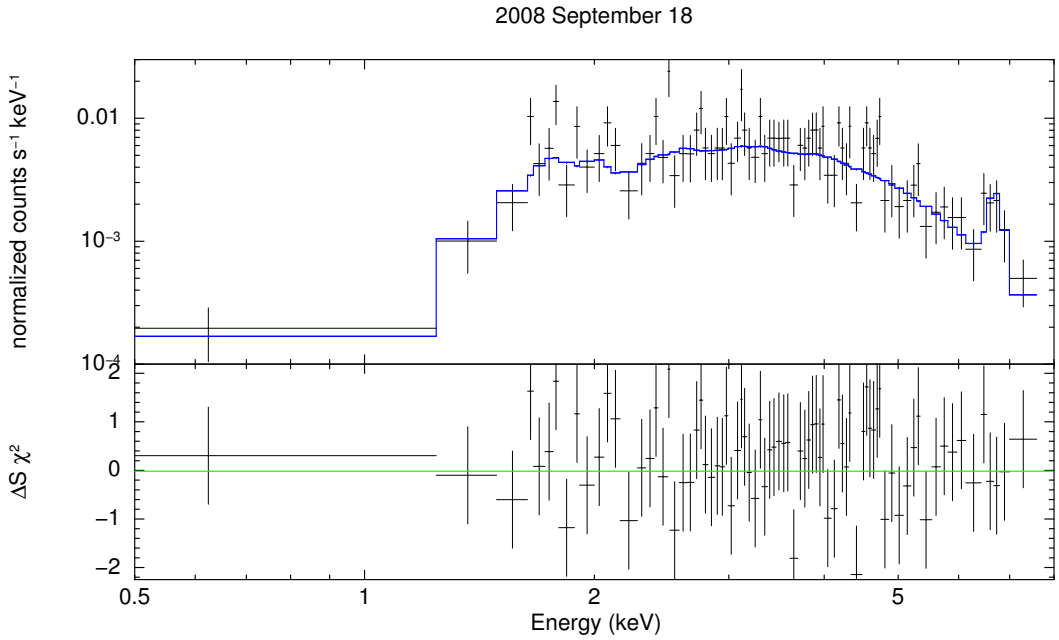


Figure 20: Best-fit XSPEC models of spectra obtained from 2008 September to 2009 April, with observations in chronological order from top to bottom. The top frame in each panel displays the data (binned to five-count-minimum bins) in black overlaid with the model in blue.

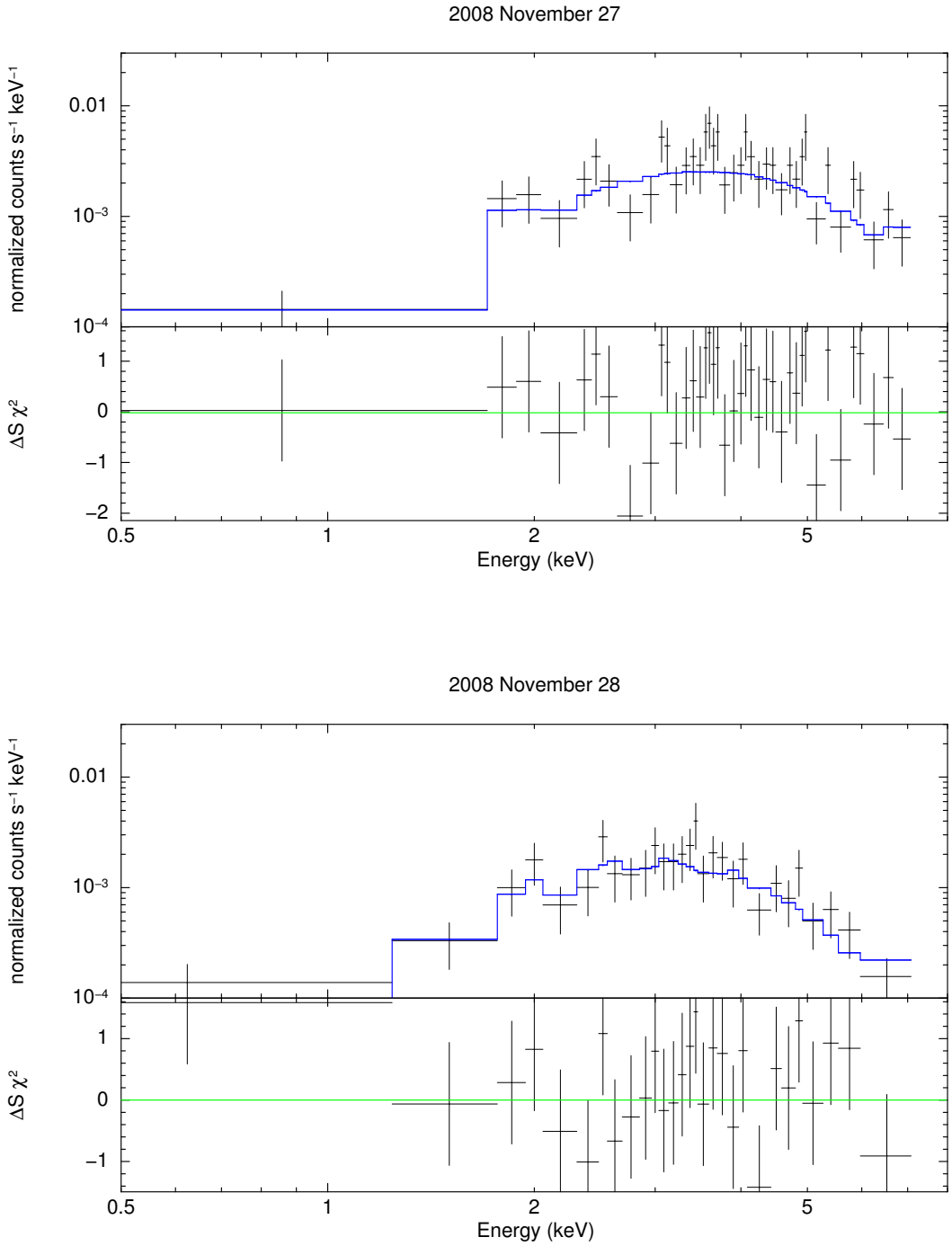


Figure 20: Best-Fit XSPEC Models of 2008–2009 V1647 Ori Spectra (cont.)

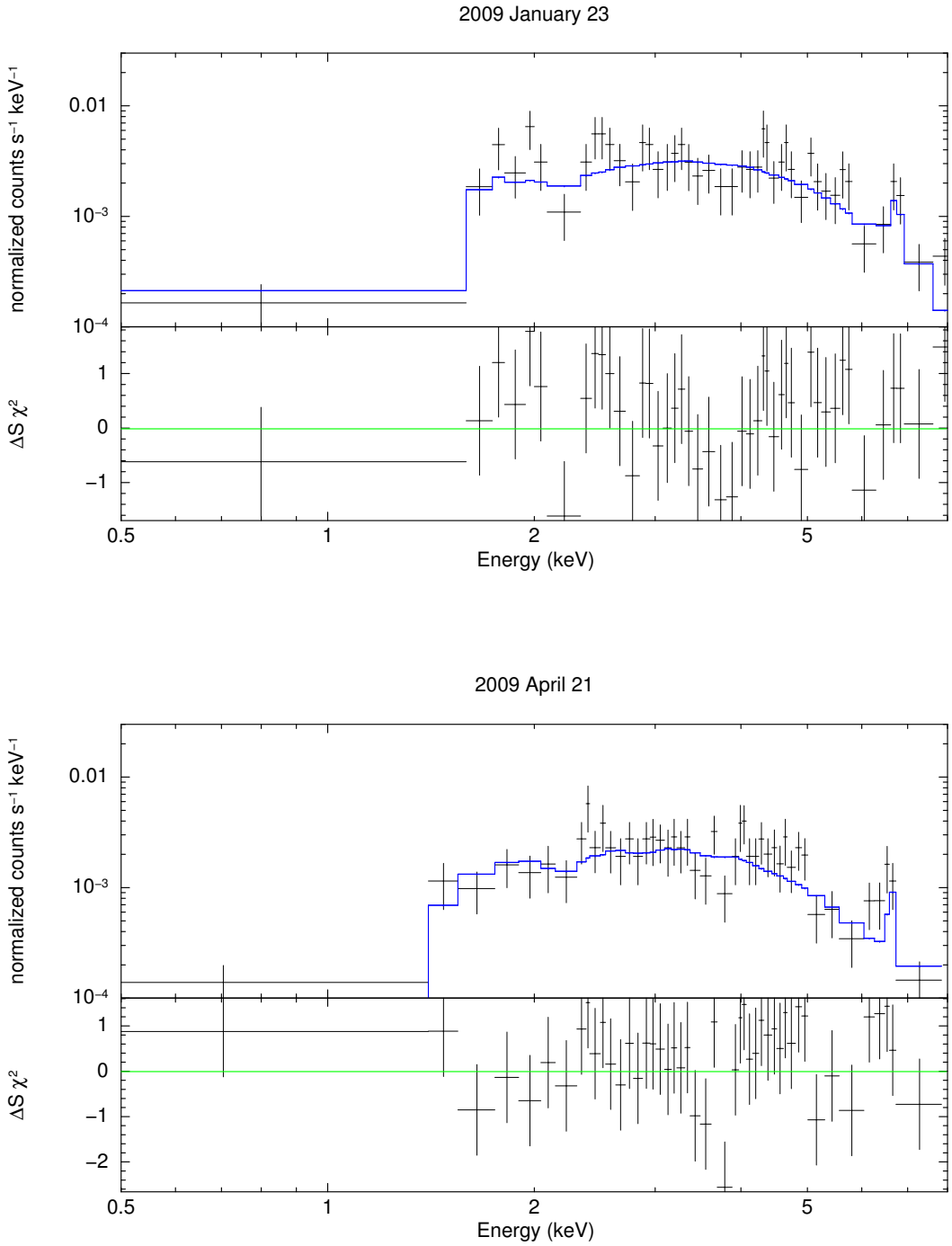


Figure 20: Best-Fit XSPEC Models of 2008–2009 V1647 Ori Spectra (cont.)

Determining a robust model for the last three recent epochs was more challenging than for the first two epochs, especially for ObsID 9916 (2009 January 23). A major concern for us was to assess whether the flux and hardness variability seen in the light curves for these observations (Figs. 15–17) contributes to the difficulty of fitting a unique model to the spectral data. To assess the effects of variability on the robustness of our spectral analysis, we divided each of these the spectra into two phases, one in which the X-ray flux was relatively lower and one in which the flux was elevated. Each of these spectra was then modeled independently. Though the hardness ratios suggest that the spectra did harden marginally as V1647 Ori went from X-ray-dim to X-ray-bright during these observations, the spectral modeling yields no measurable changes in hydrogen column density or plasma temperature. Thus, it appears that the changes in the light curves are likely due only to changes in the plasma emission measure.

**Iron Line Emission Analysis** Our initial modeling of the V1647 spectra from 2008 and 2009 suggests the presence of line emission from near-neutral iron at 6.4 keV as well as from the (unresolved) helium-like iron K$\alpha$-line triplet at 6.64, 6.67, and 6.70 keV. The neutral iron line emission at 6.4 keV is often seen in accretion-powered sources and is usually attributed to the fluorescence of cold gas in the presence of a nearby X-ray continuum emission (Tsujimoto et al., 2005). Thus, the presence of this line in some of the V1647 Ori spectra could be attributed to fluorescence of (neutral) circumstellar disk material by accretion-generated X-rays. It would not be surprising to detect this emission in the spectra of V1647 Ori given that the environment of this

YSO does appear to contain the necessary ingredients for the formation of 6.4 keV emission, namely a strong, relatively hard X-ray source illuminating cold circumstellar material. Observations of other YSOs, including roughly a half-dozen sources in the COUP survey, with these environmental components have also shown this feature.

Following Grosso et al. (2005), we added a Gaussian component centered at 6.4 keV to the spectral models in order to account for the neutral line component. Models of two observations (2008 September 18 and 2009 April 21) appear to be well fit with the addition of a 6.4 keV line with equivalent widths of $\sim$200 and $\sim$500 eV, respectively, while the 2008 November 27-28 and 2009 January 23 are fit well without the additional neutral iron line emission component (Fig. 21). On the other hand, it is possible that the 6.4 keV emission is present during all of the 2008–2009 observations from CXO but that its spectral signature is muffled by noise in the 2008 November and 2009 January observations. While it appears that we have detected 6.4 keV iron emission in the 2008 September 18 and 2009 April 21 observations, we cannot conclude definitively that these "detections" are real. We note that the best-fit 6.4 keV equivalent widths are poorly constrained with error ranges extending from zero to roughly twice the equivalent width values. Given this range of uncertainty, we cannot exclude the possibility that there is no 6.4 keV iron line. We feel confident, however, that these detections are real given that visual and quantitative comparisons of our findings with those detections found by Tsujimoto et al. (2005) are very similar.

We have compared the intensities/appearances of this line in the various observations of V1647 Ori by CXO, XMM-Newton, and Suzaku. The equivalent widths of this emission feature are very similar to those found in the spectra of the 2004

April 4 XMM observation (109 eV) and in the 2008 October 8 Suzaku observation (∼600 eV). We are unable to clearly determine whether there is a correlation between the strength and appearance of the 6.4 keV line and any of the associated plasma characteristics.

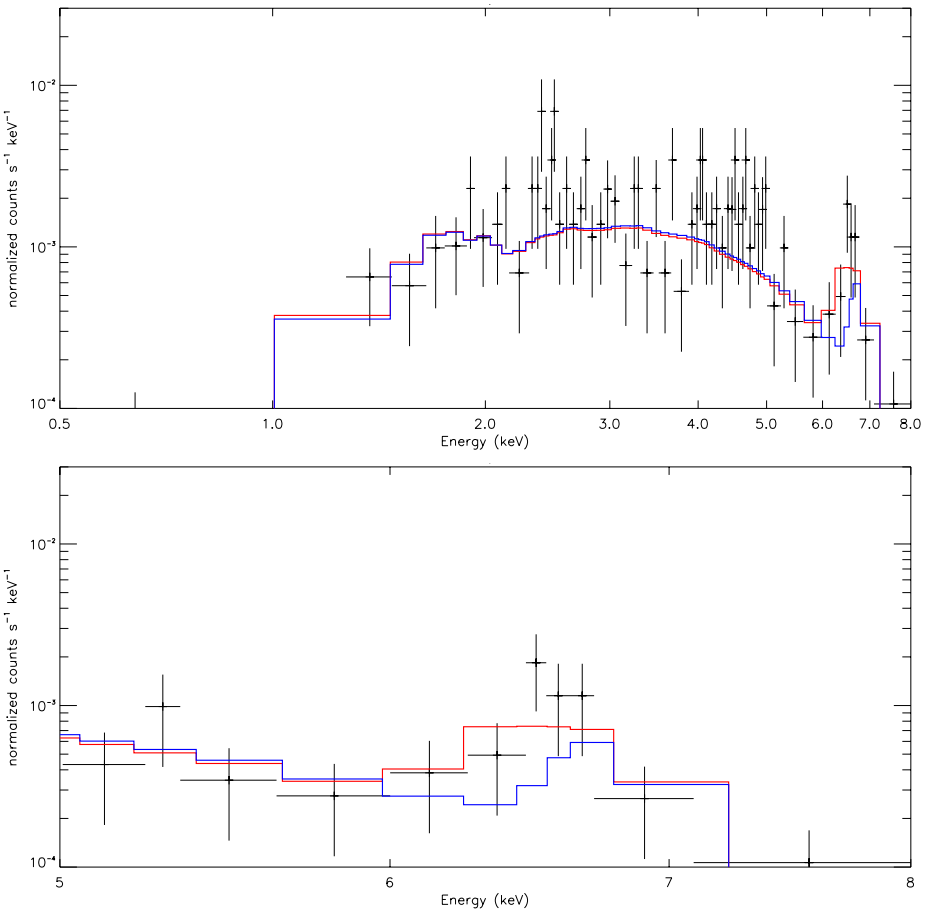


Figure 21: Spectrum of the 2009 April 21 observation (black) overlaid with the single-component plasma model (blue) and the model with the additional Gaussian component (red) centered at 6.4 keV (equivalent width of 510 eV) added to account for neutral iron emission. The entire modeled wavelength range (0.5–8.0 keV) is shown in the top panel, and the bottom panel displays the 5.0–8.0 keV energy range to more easily show the iron emission and the Gaussian component. Spectral data points employ a three-count-minimum bin size.

## 4.4 Discussion

Figure 22 suggests that the overall X-ray flux of V1647 Ori is strongly correlated with optical/near-infrared flux. This correlation is revealed more clearly in Figure 23, in which we plot the X-ray luminosity versus the $I_C$-band luminosity. We interpolated $I_C$-band luminosities for the 2002–2005 X-ray observation dates. We did not extrapolate $I_C$-band luminosities for the two 2006 X-ray observation dates due to the highly uncertain flux behavior of V1647 Ori. Of the 2008-2009 X-ray observations, we could only interpolate an $I_C$-band luminosity for ObsID 9916. With these eight interpolated luminosities, we derived a correlation coefficient between X-ray luminosity and $I_C$-band luminosity of 0.65.

Dramatic increases in optical/near-infrared flux for YSOs, such as FU Ori, have long been thought to be associated with enhanced accretion (Hartmann & Kenyon, 1996). In such an environment, material is channeled through magnetic funnels from the co-rotation radius of the circumstellar disk down to the photosphere (Shu et al., 1994). Hence, when the X-ray flux from a pre-main-sequence star or protostar is elevated and the rapid rise in X-ray emission is directly correlated with large-scale optical outbursts, the correlation itself strongly suggests that accretion is the mechanism responsible for generating the increase in X-ray output (Kastner et al., 2006).

One way in which accretion-generated X-ray emission could be identified observationally would be through the relatively soft X-rays emitted by the plasma when it plunges onto the stellar surface at free-fall velocities and is shock heated to tempera-

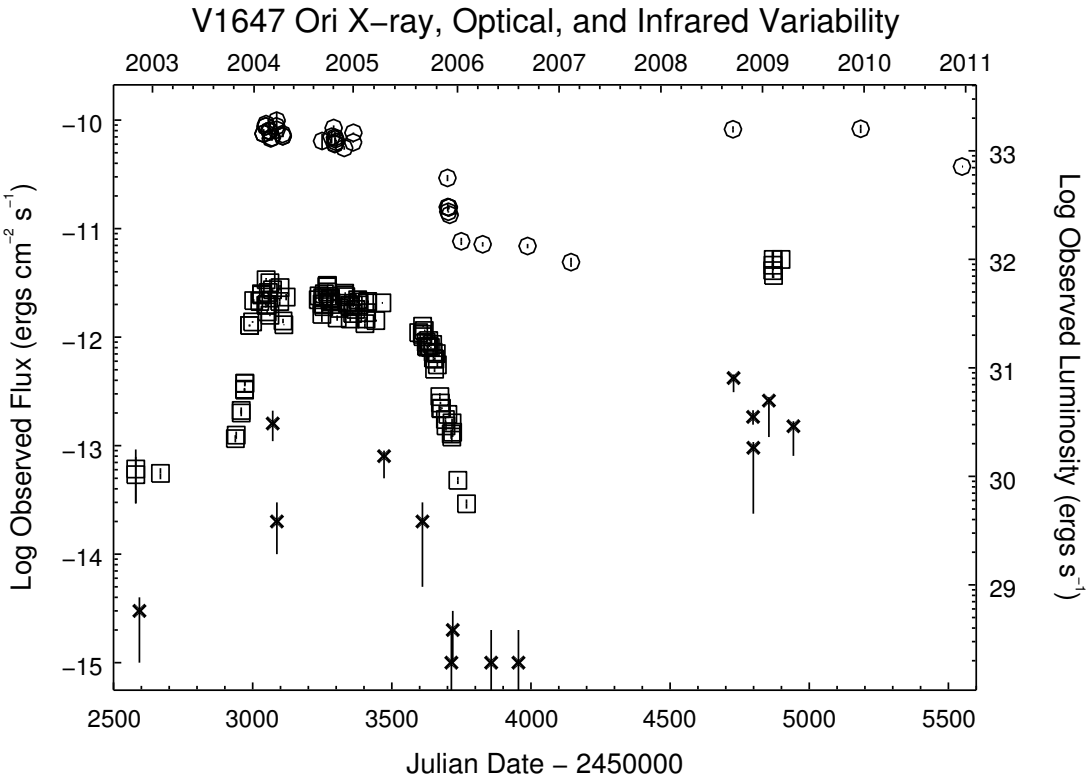


Figure 22: Near-infrared and X-ray light curves of V1647 Ori. Chandra X-ray data are shown as crosses; the $I_c$-band data are shown as squares, and the H-band data are shown as circles. I-band Goddard Robotic Telescope (GRT) (Sakamoto et al., 2011) data (Michael Richmond, personal communication) were obtained in 2009. For the published I- and H-band data, error bar size is on the order of the data point size (data are from: Briceño et al. (2004), McGehee et al. (2004), Reipurth & Aspin (2004), Semkov (2004), Ojha et al. (2005), Ojha et al. (2006), Semkov (2006), Venkat & Anandarao (2006), Acosta-Pulido et al. (2007), Fedele et al. (2007), Aspin, Beck, & Reipurth (2008), Ojha et al. (2008), Aspin et al. (2009), and Venkat & Anandarao (2011)). The uncertainties for the GRT data and CXO data are $1\sigma$. Calendar year is indicated along the top horizontal axis.

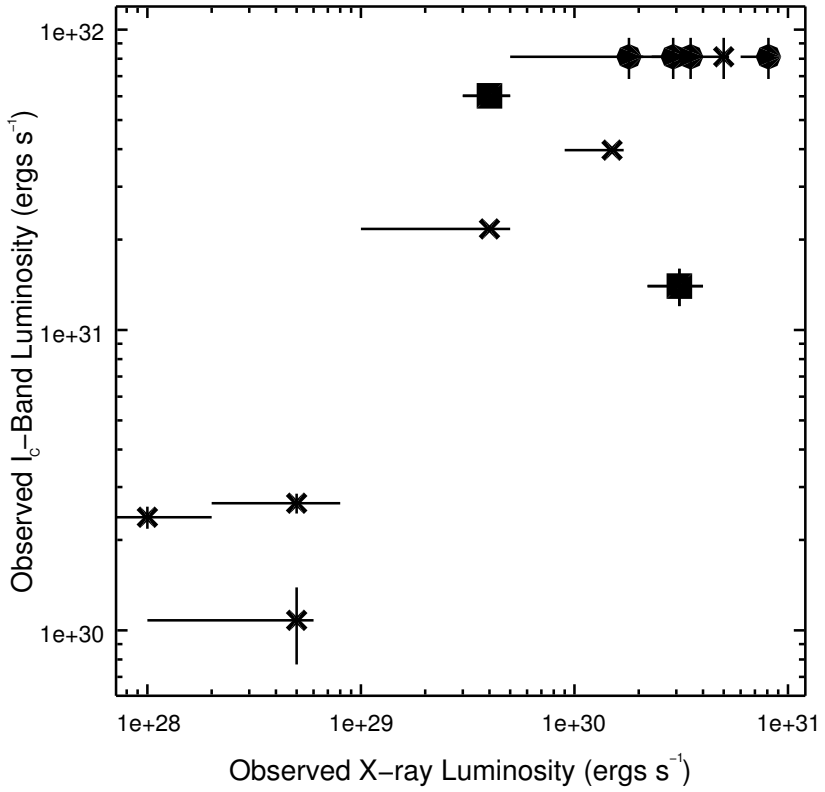


Figure 23: Two-parameter plot for all CXO observations of V1647 Ori showing the correlation between the observed $I_c$-band near-infrared and X-ray luminosities. Crosses represent data obtained with ACIS front-illuminated CCDs, and squares represent data obtained with the ACIS back-illuminated S3 CCD. Errors for $I_c$-band luminosities that were interpolated at X-ray observation dates were calculated by averaging the errors of the $I_c$-band luminosities of the five observations made nearest to the interpolation date. Circles represent four observations (ObsIDs 9915, 10763, 8585, and 9917) in which the interpolated $I_c$-band luminosity of ObsID 9916 was assumed to be the correlated $I_c$-band luminosity. The correlation coefficient for the $I_c$-band and X-ray luminosities without the circle values is 0.65, while the correlation coefficient using all values is 0.67.

tures of a few million Kelvin ($kT_X$ ~0.3 keV) (Kastner et al., 2002; Stelzer & Schmitt, 2004; Raassen, 2009; Brickhouse et al., 2010). We can speculate that a second such signature would be much hotter ($kT_X$ ~few to tens of keV) and harder X-rays generated in magnetic reconnection events (Shibata & Yokoyama, 2002; Brickhouse et al., 2010) within the accretion streams. Whether the soft or hard X-ray generating plasma is observable likely depends on the observing geometry. If we have an unobscured line of sight to the footprint of the accretion column, our observations should be sensitive to the cooler plasma; if the accretion column obscures our view of the accretion-column footprint, our observations should be sensitive only to the hotter plasma in the accretion stream; and if the obscuration of the accretion footprint is partial, we might detect both plasmas. In between periods of dramatically enhanced accretion, previous studies such as COUP (Preibisch et al., 2005; Stassun et al., 2006) and the XMM-Newton Extended Survey of the Taurus molecular cloud (XEST) (Audard et al., 2007), suggest that the X-ray signature of young stars should be that of normal coronal emission. Such emission would be similar to but much fainter than the hot, hard plasma seen from reconnection events in the accretion funnel.

During quiescence, the X-ray flux of V1647 Ori has a low count rate, low median photon energy, and negative hardness ratio; in contrast, when the X-ray flux is elevated, the count rate increases by a factor of 25 or greater, the median photon energy doubles, and the hardness ratio becomes strongly positive. Most of the V1647 Ori light curves reveal that this YSO also experiences what appear to be short-term (few kilosecond) variability in its X-ray flux.

### 4.4.1 Observations of Hotter and Cooler X-ray-Generating Plasmas

Since most of the CXO observations show this short-duration variability when the X-ray count rate is high, the short-term variations are likely part of the normal behavior for V1647 Ori. For all 2008–2009 CXO observations, the X-ray variability is almost entirely seen in hard (>2.8 keV) X-rays. Our model fits of the V1647 Ori spectra indicate that the X-ray signature of the plasma we observe from this source during optical eruptions is predominantly a bright, hot, hard, single-temperature plasma heated to temperatures of 2–6 keV, which is also consistent with X-rays generated from reconnection events in an accretion funnel (Isobe et al., 2003; Brickhouse et al., 2010).

We must keep in mind, however, that the intervening hydrogen column density will play a significant role in our ability to detect X-ray flux from accretion hotspots at temperatures of a few million Kelvin, especially when dealing with column densities as high as those modeled in V1647 Ori observations. An accretion-footprint (shocked) plasma at a temperature of $kT_X \sim 0.3$ keV subject to an intervening absorbing column density of a few times $10^{22}$ cm$^{-2}$ would have ∼98% of its X-ray flux extinguished. Even given the smallest hydrogen column density found via spectral modeling of the 2004–2005 V1647 Ori observations when the hydrogen column density was allowed to vary freely ($\sim 1 \times 10^{22}$ cm$^{-2}$), such a soft component still has ∼96% of its X-ray flux absorbed. If the hydrogen column density decreased dramatically — to $N_H$ of a few times $10^{21}$ cm$^{-2}$ — the accretion shock emission could dominate the observed flux. This seems a plausible scenario to explain the softer plasma detected in late

2004 March, especially if the large intervening hydrogen column density inferred at other observing epochs was due mostly to the accretion streams.

An alternative explanation is that we observed V1647 Ori when it was in the midst of a large accretion episode that pushed the star-disk boundary inward to the point where the accretion became non-magnetospheric (Hartmann, 1998), effectively reducing the amount of hard X-ray flux produced by magnetic reconnection events in the accretion stream.

During the 2008–2009 epoch, when the X-ray luminosity of V1647 Ori increased, the spectrum hardened and the emitting plasma increased in temperature (Fig. 18, right panel); also, when the overall X-ray luminosity decreased, the X-ray spectrum softened and the X-ray generating plasma cooled. These correlations are also seen in the Chandra observations following the 2003 eruption (Fig. 18, left panel). However, between 2008 September and 2008 November, the spectrum appeared to harden slightly as the X-ray luminosity decreased slightly. If we are observing X-rays generated predominantly by the $\sim$1 keV plasma in the accretion footprint, then a decline in accretion should result in a decline in total X-ray luminosity, particularly in the lower energy flux, resulting in a hardening of the spectrum. Therefore, the hardening of the spectrum and decrease in X-ray luminosity observed between 2008 September and November might be a time when CXO was able to see plasma closer to the protostellar surface. In fact, this epoch showed a low temperature ($\sim$2 keV) plasma, consistent with what could be a mixture of hotter (4–6 keV) and cooler (1 keV) plasmas. These data may offer evidence that the X-ray flux includes an emission component from the cooler plasma in the footprint of the accretion funnel located in the stellar photo-

sphere. Because the cooler plasma suffers greater extinction and because CXO is less sensitive to softer X-ray emission than XMM-Newton, CXO would likely only detect the cooler plasma when the viewing geometry is favorable.

**Intervening Hydrogen Column Density** Our modeling work for the X-ray observations obtained in 2004–2005 and 2008–2009, when the mean X-ray count rates were greater than 1 cts $ks^{-1}$ yield a best fit value for $N_H$ of about $4.1 \times 10^{22}$ $cm^{-2}$, consistent with the results derived by Grosso et al. (2005) and a visual extinction of $A_V \sim 20$ (Vuong et al., 2003). We were unable to fit $N_H$ in our modeling work for the low count-rate observations during the quiescent period in 2005–2006; however, Aspin, Beck, & Reipurth (2008) obtained a best fit value for $A_V$ of $19 \pm 2$, based on their optical, near-infrared, and mid-infrared observations obtained in February 2007, which was also during the quiescent period (based on the optical and near-infrared photometry reported by Aspin, Beck, & Reipurth (2008)). The observed value of $A_V$ for February 2007 lends strong support to our use of $N_H = 4.1 \times 10^{22}$ $cm^{-2}$ for our modeling of the quiescent epoch observations. In addition, together these data suggest that $N_H$ and, by implication, $A_V$, remained essentially unchanged as inferred from the X-ray observations, whether V1647 Ori was in the quiescent or elevated X-ray state.

On the other hand, as seen at longer wavelengths, the extinction toward V1647 Ori has changed. Ábrahám et al. (2004) derive $A_V = 13$ from near-infrared data obtained in 1998 by 2MASS. During the outburst in 2004–2005, Briceño et al. (2004) found $A_V = 8$–$10$ on 2004 February 18, Reipurth & Aspin (2004) found $A_J = 1.26$, $A_H = 0.81$,

and $A_K = 0.5$ on 2004 Feburary 18, all of which are consistent with $A_V$ of $\sim$5 (Becklin et al., 1978), Vacca et al. (2004) obtained $A_V = 11$ from measurements of the 3.1 $\mu$m water band on 2004 March 9, and Ojha et al. (2006), who made optical and near-infrared observations from 2004 into very late 2005, reported $A_V$ of $\sim$5 during the 2004 outburst. Ojha et al. (2006) then report that $A_V$ increased to $\sim$10 by the end of 2005, when V1647 Ori had dramatically faded, and Aspin, Beck, & Reipurth (2008) reported $A_V$ was as high as 19 by early 2007. Clearly, the extinction, as measured via optical and near-infrared measurements, changed first from quiescence to outburst and then from outburst back to quiescence.

These apparently discordant results have a straightforward and consistent explanation in the context of an accretion episode. In X-rays, we are essentially detecting V1647 Ori along a direct line of sight to the stellar photosphere. Our results therefore indicate that the absorption along this direct line of sight — which likely includes at least part of a thick circumstellar disk that is tilted about 30 degrees from edge-on (Acosta-Pulido et al., 2007) — does not change significantly as a function of time, despite the evident changes in X-ray luminosity. The optical and near-infrared photons we observe, however, emerge from the near-photosphere environment of V1647 Ori along two paths. One path, along our direct line of sight to the photosphere, produces heavily reddened and extincted light. The second path takes photons nearly perpendicular to our line of sight, through an evacuated polar cavity, where they then scatter into our line of sight (Acosta-Pulido et al., 2007). These photons are bluer and much less heavily extincted than the line-of-sight photons. When V1647 Ori is in the quiescent state (1998, late 2005–2007), we see a faint, reddened, heavily

extincted source because the contribution from scattered light is minimal. During the outburst state (2004–2005; 2008–2009), we see a brighter, bluer source because the contribution to the continuum of scattered photons is large.

### 4.4.2 Possibility of a Second Plasma

Though the plasma temperature of V1647 Ori strongly correlates with the X-ray luminosity and hardness ratio (Fig. 18), it is unclear whether we are observing a single-component plasma that increases or decreases in temperature and thus causes the observed changes in X-ray luminosity or if a second, lower-temperature plasma is also present and whose contribution to the total spectrum is overwhelmed by the hotter temperature plasma during outbursts. Other sources, such as V710 Tau (Shukla et al., 2008) and EX Lupi (Grosso et al., 2010) have spectra that can be modeled as two-temperature plasmas, with one component fading as the star returns to quiescent levels. Grosso et al. (2005) was able to model the XMM-Newton observation of V1647 Ori in 2004 April with a single-temperature plasma but also found a better fit using a two-component model. However, this observation of V1647 Ori was at least twice as long as most of the Chandra observations from 2004–2009. In addition, XMM-Newton is more sensitive to lower-energy photons than CXO/ACIS. Therefore, it may be the case that V1647 Ori does have two plasmas that contribute to the X-ray spectra but that ACIS was unable to consistently detect the lower-temperature component due to the inherit limitations of its design, the shorter observation times of the CXO observations, and the high degree of softer X-ray absorption by the intervening hydrogen column.

In order to test whether CXO would be able to detect two distinct plasma temperatures in 5 ks and 20 ks observations, we simulated a two-component plasma (using *fakeit*) with a normalization ratio and plasma temperatures identical to those found by Grosso et al. (2005) and suffering extinction by the same hydrogen column density. The simulated spectra were then convolved with the responses of the front-illuminated ACIS-I3 and back-illuminated ACIS-S3 CCDs. The simulations incorporated appropriately-scaled normalization parameters so that the resultant count rates were comparable to those of the 2005 and 2008–2009 CXO observations. Each of the simulated spectra was first fit with a single-component model and then with a two-component model. All of the 20 ks observations were found to be fit better using two-component models with each fit yielding values for plasma temperatures and normalization that were close to the original simulation parameters. F-tests also suggested a slight improvement in the model fits if the 75%/25% normalization ratio between the low/high components, as found by Grosso et al. (2005), was forced. When fit with a two-component model, the simulated 5 ks observation of the more sensitive ACIS-S3 CCD yielded a best fit (using the 75%/25% normalization ratio) that converged to a model with two nearly-identical temperature plasmas, i.e., to a single-temperature plasma, and thus does not lead to a better fit. Thus, it appears that CXO should have the sensitivity to detect a two-component plasma such as that found by Grosso et al. (2005) if the observations are long enough and the lower-temperature plasma flux is strong enough compared to the higher-temperature plasma flux.

The spectral models for each of the five Chandra observations obtained in 2008–

2009 consistently converge to fits with a single-temperature plasma that, to within the errors, is ∼4 keV. As seen with the correlation between X-ray luminosity and the mean hardness ratio, median photon energy, and mean count rate, we also find that when the X-ray luminosity increases or decreases, so does the plasma temperature. This single-component model is consistent with the single-component model of the 2005 April 11 XMM-Newton data (Grosso et al., 2005).

### 4.4.3 Similarity of the 2003 and 2008 Eruptions

Finally, the second (2008) eruption of V1647 Ori has very similar spectral characteristics to that of the first (2003–2005) eruption. From Tables 1, 3, and 4, the five 2008–2009 observations of V1647 Ori, which span a period of approximately seven months, show

- mean hardness ratios that are consistently as hard (to within the errors) as the hardest value of any observation following the previous eruption;
- median photon energies at levels that are very similar to the greatest median photon energy of any observation from the previous eruption;
- mean count rates that are 20–50 times higher than those observed during X-ray quiescence and that are typically 1–2 times the highest mean count rate of the 2003–2006 observations;
- plasma emission measures that are usually 1–2 times greater than any modeled from the 2003-2005 observations;

- and X-ray luminosities that are consistently greater than $1.5 \times 10^{30}$ ergs $s^{-1}$, 1–2 times the X-ray luminosity of V1647 Ori during any of the 2003-2005 CXO observations.

Given that the spectral characteristics of V1647 Ori are so similar in observations in which the X-ray flux is elevated above the X-ray quiescent level, it appears that the same X-ray generation mechanism was at work during both eruptions and that the plasma characteristics were very similar during the two eruption epochs. The derived X-ray luminosities suggest that the second eruption was more energetic than the first, and given that the modeled emission measures are greater for the observations following the second eruption, it is reasonable to conclude that we observed the same phenomenon in both eruptions but that a larger mass of X-ray emitting plasma was active during the outburst that began in 2008.

## 4.5 Summary

Our X-ray monitoring demonstrates that the two optical/near-IR outbursts undergone by the enigmatic V1647 Ori in less than a decade were accompanied by strong X-ray outbursts. During these two outbursts (2003–2005 and 2008–present), we see that the X-ray flux rose to peak luminosity over a span of a few weeks and then remained elevated for approximately two years during the first eruption and for at least one year during the second eruption. Given that there is very strong evidence that the outbursts observed in the optical and near-infrared regimes are driven by accretion, we conclude that the correlated outbursts in X-rays are also driven by accretion.

We find that all of the CXO spectra of V1647 Ori are best modeled with a single, moderate-temperature (2–6 keV) plasma. In almost all cases, the plasma temperature that emerges from models of the CXO spectra is too high to be generated via accretion hotspots on the stellar photosphere but is reasonable for a plasma generated via magnetic reconnection events. However, the X-ray-emitting plasma could also be located in a strongly enhanced stellar corona, or at the inner edge of the circumstellar disk. Given that accretion is ongoing, lower-temperature plasma generated by shocks at the accretion footprint is very likely present; however, during these CXO observations, any such soft component contributed much less flux than the moderate-temperature plasma and so usually did not leave a distinct signature in the X-ray spectra. With the elevated hard X-ray flux lasting the duration of the 2008–2009 epochs, we conclude that the X-ray flux is not the result of typical coronal flares generated via reconnection events. We believe that since the optical/near-infrared flux remains elevated throughout this observation epoch, we are instead observing the X-rays generated from reconnection events in the accretion stream, with the softer X-ray flux possibly being generated by accretion hotspots at the stellar photosphere.

We find no significant change in X-ray absorbing column, indicating that varying optical/IR color measurements, which have previously been interpreted as evidence for variable reddening toward V1647 Ori, may instead be indicative of varying contributions from scattered vs. direct photospheric emission from the YSO. Two of the spectra obtained during the most recent (2008) outburst appear to show the 6.4 keV neutral iron feature indicating fluorescence from cold (presumably circumstellar disk) gas surrounding V1647 Ori.

With V1647 Ori being observed intensely during both outbursts at X-ray, optical, and infrared wavelengths, this objects stands as one of the best characterized systems that exhibits such a close correspondence between X-ray output and accretion rate. As a result of intense monitoring at X-ray, optical, and infrared wavelengths during two successive accretion-driven outbursts, V1647 Ori stands as the best characterized YSO in terms of the correspondence between X-ray output and accretion rate. We have shown, furthermore, that this YSO exhibited strikingly similar X-ray behavior and spectral properties during its recent accretion bursts. These results underscore the need for X-ray monitoring of additional eruptive YSOs, so as to evaluate whether the remarkable consistency of V1647 Ori is the exception or the norm.

We thank Nuria Calvet for providing early access to the data in CXO ObsIDs 10763 and 8585. This research was supported via awards numbers GO8-9016X and GO9-0006X to Vanderbilt University issued by the Chandra X-ray Observatory Center, which is operated by the Smithsonian Astrophysical Observatory for and on behalf of NASA under contract NAS8-03060.

# CHAPTER V

# DETECTION OF A COOL, ACCRETION SHOCK-GENERATED X-RAY PLASMA IN EX LUPI DURING THE 2008 OPTICAL ERUPTION

In this chapter, I present the current version of a manuscript that has been submitted for publication. This paper deals with analysis of the X-ray observations obtained of the young, erupting star EX Lupi during its 2008 optical outburst. This paper, in which I am first author, is a collaboration between myself, my advisor David Weintraub, and the following individuals:

- Nicolas Grosso - Observatoire Astronomique de Strasbourg, Université de Strasbourg
- Joel Kastner and Michael Richmond - Rochester Institute of Technology
- Kenji Hamaguchi - Goddard Space Flight Center

## 5.1 Introduction

The classical T Tauri star (cTTs) EX Lupi is the prototype of a class of young, heavily embedded, pre-main sequence (PMS) stars known as "EXors" that are observed to undergo irregular optical outbursts (Herbig, 2001), with each outburst continuing for up to a few years. EX Lupi was first observed to undergo a large optical outburst in 1955, brightening by nearly five magnitudes from a typical quiescent optical magnitude of 13.2 to a peak magnitude of 8.4 before fading back to its quiescent

level approximately one year after the onset of the outburst (Herbig, 1977). EX Lupi had erupted five times prior since the 1890s; however, these eruptions typically increased the optical brightness of EX Lupi by only one or two magnitudes (McLaughlin, 1946). With considerable gaps in the observing data, it is unclear what the peak outburst magnitudes were or how long these outbursts lasted. It does appear clear, however, that the 1934 eruption lasted much longer (at least six years) than what is typically observed for EX Lupi. In 1994, almost 40 years after its 1955 outburst, EX Lupi was observed to erupt again, brightening to a peak magnitude of 11.4 in the V band and remaining brighter than magnitude 13.0 for approximately 1.5 years (Herbig, 2001). Three similar small eruptions occurred during the next eight years with EX Lupi reaching a peak magnitude of 11.3, 11.1, and 10.8 in the V band in 1998 June, 1999 July-July, and 2002 July-August, respectively (Herbig, 2007). The most recent eruption began in 2008 January when EX Lupi was observed to brighten to a peak visual magnitude of $\sim$8 at the end of the month (Jones, 2008) and remained in an elevated optical-flux state for approximately 8 months. This latest eruption therefore appears to rival the 1955 "extreme" outburst, though the 1955 outburst appears to have lasted a few months longer.

During an EXor outburst, the underlying spectrum is veiled by hot continuum emission and some emission features show an inverse P-Cygni profile (Herbig, 2001), signifying an infall of circumstellar material. Consequently, the large-scale variability of EXors is attributed to short-lived increases of the mass accretion rate (e.g., from a quiescent value of $6 \times 10^{-9}$ to $2 \times 10^{-7}$ $M_{\odot}$ yr$^{-1}$ for the 2008 optical outburst, according to Aspin et al. 2010). Proposed mechanisms for eruptive young stellar objects

(YSOs), such as EXors, include circumstellar disk instabilities that arise because of the gravitational influence of a nearby (unseen) companion (Bonnell & Bastien, 1992), thermal instabilities in the circumstellar disk (Bell et al., 1991; Clarke et al., 1989), and magnetohydrodynamic instabilities within the disk (Armitage et al., 2001; D'Angelo & Spruit, 2012). EXors are similar in behavior to another class of young, erupting stars known as "FUors." These stars are also thought to erupt due to sudden, massive accretion events. The main differences between the two classes are that FUors have higher accretion rates (roughly $10^{-4}$ $M_{\odot}$ yr$^{-1}$) during outbursts, resulting in the visible flux levels being elevated by several more magnitudes than what is found in EXor outbursts, and that the durations of the FUor outbursts are typically decades whereas EXor outbursts are, at most, a few years in duration (Hartmann & Kenyon, 1996).

PMS stars are known to produce a significant amount of flux as X-rays ($L_X/L_{bol}$ $\sim 10^{-4}$–$10^{-3}$, compared with $L_X/L_{bol} \sim 10^{-7}$–$10^{-6}$ for the Sun), although the origin of the X-ray flux is not well understood. The hard (E $\gtrsim$ 1.0 keV) X-ray flux is generally attributed to coronal activity, as in the analysis by Preibisch et al. (2005) of observations of a large sample of young stars in Orion in the Chandra Orion Ultradeep Project (COUP). Others have found that accretion of material onto the star could be another source of soft (E $\lesssim$ 1.0 keV) X-rays. Circumstellar material that is accreted onto the stellar photosphere at near free-fall velocity is capable of generating soft X-rays as it is heated to a temperature as high as a few million degrees Kelvin ($kT_X$ $\sim$ 0.04 to 0.4 keV) (Sacco et al., 2010). This emission can be now identified via X-ray spectroscopy (see, e.g., review by Güdel & Nazé (2009)). An excellent example

of an object in which this process appears to be occurring is the nearby, relatively evolved (age $\sim$ 10 Myr) cTTs TW Hydrae (Kastner et al., 2002; Brickhouse et al., 2010; Dupree et al., 2012). Brickhouse et al. (2010) modeled the accretion onto a stellar photosphere and found that there arise two regions where soft X-ray emission could arise: an inner shock front, where material first impacts the photosphere, and a outer post-shock region that is heated by energy transfer from the shock region to coronal material at temperatures of over 1MK. To further complicate the issue, some accreting stars may have their X-ray production, specifically the softer X-rays, quenched during accretion episodes (Gregory et al., 2007). Quenching could occur if the hydrogen column density in the accretion column absorbs the accretion shock-generated X-rays originating from the accretion footprint in the stellar photosphere.

The PMS star V1647 Ori exhibited different behavior when it was observed during its optical/NIR outbursts from 2002–2006 (where the mass accretion rate varied from a quiescent value of $6\times10^{-7}$ to $2\times10^{-5}$ $M_{\odot}$ yr$^{-1}$ Muzerolle et al. 2005) and again from 2008–2009 by CXO and XMM-Newton (Kastner et al., 2004, 2006; Grosso et al., 2005; Grosso, 2006; Hamaguchi et al., 2010; Teets et al., 2011). During the optical outbursts of V1647 Ori in these two epochs, the X-ray flux correspondingly increased by up to two orders of magnitude; however, the increases in X-ray flux were primarily detected in the harder (2.8–8.0 keV) energy range. The spectral characteristics of V1647 Ori during both outbursts were remarkably similar and best modeled as plasma at temperatures on the order of 2–6 keV, too high to be produced by an accretion shock but in the range expected from magnetic reconnection events in the accretion streams (Teets et al., 2011). The high local hydrogen column density around V1647 Ori

makes it nearly opaque to lower-energy X-ray photons generated in the photosphere, making the direct detection of X-ray flux from shocks at accretion hotspots difficult; however, direct evidence of the existence of such hotspots may be present in the form of a rotational modulation signature observed in the X-ray light curve of V1647 Ori (Hamaguchi et al., 2012).

EX Lupi was observed in the UV and X-ray regimes with XMM-Newton during a 78 ks observation beginning on 2008 August 10. Grosso et al. (2010) found the X-ray spectrum of EX Lupi to be best modeled as a two-component plasma with one component at a temperature of $kT_X \sim 0.5$ keV suffering very low extinction from a hydrogen column density of $3.6 \times 10^{20}$ cm$^{-2}$ and the other, which dominated the intrinsic X-ray emission, at a temperature of $kT_X \sim 4.6$ keV suffering very high extinction from a hydrogen column density of $2.7 \times 10^{22}$ cm$^{-2}$. The cooler component was determined to likely be associated with X-ray emission from accretion shocks due to its low X-ray temperature, and the UV activity observed was found by Grosso et al. (2010) to be typical of accretion events and dominated by emission from accretion hotspots covering about one percent of the stellar surface.

In this paper, we present three periods of X-ray observations of EX Lupi obtained with the Chandra X-ray Observatory (CXO). The first X-ray dataset was obtained approximately two months after the peak of optical outburst, the second was collected three months later, and the third about seven months after the first observation. These three observation epochs, along with the XMM-Newton observation in 2008 August, allow us to follow the X-ray evolution of this object as it faded back toward quiescence at optical wavelengths. In §2, we describe the observations and data

reduction. In §3, we discuss the results and their implications in the context of accretion shock-generated X-ray production.

## 5.2 Observations & Data Reduction of X-ray Data

A 20.1 ks exposure observation of EX Lupi was triggered on 2008 March 25 (CXO Cycle 9; PI: D. Weintraub, ObsID 8923) with CXO after EX Lupi was observed to be in optical outburst in 2008 January (Jones, 2008). Subsequent anticipated target-of-opportunity observations were initiated on 2008 June 16 (ObsID 8924, 20.1 ks), 2008 October 6 (ObsIDs 8925 and 10789 with durations of 10.6 and 15.4 ks, respectively), and 2008 October 9 (ObsID 10791, 4.1 ks). The 2008 October observation was split into three separate exposures due to CXO scheduling constraints. ObsIDs 8925 and 10789 were both obtained on 2008 October 6 while ObsID 10791 was obtained on 2008 October 9. Together, these five pointings yield an observing sequence, spanning approximately seven months, that follow the X-ray evolution of EX Lupi from two months after the start until after the conclusion of the optical outburst. During this same seven-month period (specifically in 2008 August), a 78 ks anticipated target-of-opportunity observation of EX Lupi was also obtained by XMM-Newton (Grosso et al., 2010). For all Chandra observations, the Advanced CCD Imaging Spectrometer Imaging (ACIS-I) array was used in faint telemetry mode with EX Lupi at the aimpoint of the I3 CCD.

CIAO v4.1 and CALDB v4.1.0–4.1.4 were used to reduce the data and extract pulse-invariant (PI) spectra. Observation details are given in Table 5. CXO/ACIS has a calibrated energy range of 0.3–10 keV, so the observation event files were first

filtered to only include events with nominal energies that fell within this range. Source spectra were then extracted from 2.5″ radius regions (making sure the aperture size was appropriate to encompass $\gtrsim$90% of the photons) while background spectra were extracted from regions near but beyond 2.5″ from the target, on the same CCD (I3), using 20″ outer radius extraction apertures. The light curves for all of these CXO observations are shown in Figure 24. The light curves for the three October observations (Fig. 24, bottom panel) show that the X-ray count rate appears to be at roughly the same level for all three observations, the hardness ratios do not change in any significant way, and no flaring events appear in these data. In addition, the median photon energy (not shown) is statistically indistinguishable in these three data sets. Finally, these three observations were obtained close enough in time to one another that the detector characteristics/responses of ACIS should not have changed in any significant way. Therefore, we used CIAO to extract and combine the spectra of the three October observations and present the composite X-ray spectrum characteristics, along with those of the 2008 March and June spectra, in Table 5. The resultant spectral data points for each of the three observation epochs were grouped into energy bins with a minimum of five counts per bin prior to spectral modeling. The count rates were high enough and durations long enough for each of the observations that this bin size yielded PI spectra with good statistics.

Table 5. Chandra ACIS Observations of EX Lupi Following the 2008 Outburst

| ObsID | Observation Date | JD | Exposure (ks) | Net Counts | Mean Count Rate ($ks^{-1}$) | Median Photon Energy (keV) | Hardness Ratio[a] (H–S/H+S) |
|---|---|---|---|---|---|---|---|
| 8923 | 2008 Mar 25 | 2454551 | 20.1 | 944 | $47.6 \pm 1.6$ | $1.15 \pm 0.02$ | $-0.06 \pm 0.03$ |
| 8924 | 2008 Jun 16 | 2454634 | 20.1 | 318 | $16.0 \pm 0.9$ | $1.09 \pm 0.03$ | $-0.13 \pm 0.06$ |
| 8925[b] | 2008 Oct 6 | 2454746 | 30.1 | 232 | $7.7 \pm 0.5$ | $1.69 \pm 0.06$ | $0.55 \pm 0.05$ |
| 10789[b] | 2008 Oct 6 | 2454746 | | | | | |
| 10791[b] | 2008 Oct 9 | 2454749 | | | | | |

[a]Hardness ratio computed using the total numbers of hard and soft X-ray photons from the entire observation.

[b]Parameter values are derived from the combined spectra of the three 2008 October observations (ObsIDs 8925, 10789, and 10791.

Note. — All errors are $1\sigma$. The net counts for each observation are the total number of counts within the 0.3–10.0 keV range. Median photon energy uncertainties were calculated via the half-sample method used in Kastner et al. (2006). Mean count rates were determined by dividing the net counts by exposure times. Uncertainties for mean count rates and hardness ratios of total counts follow Poisson statistics.

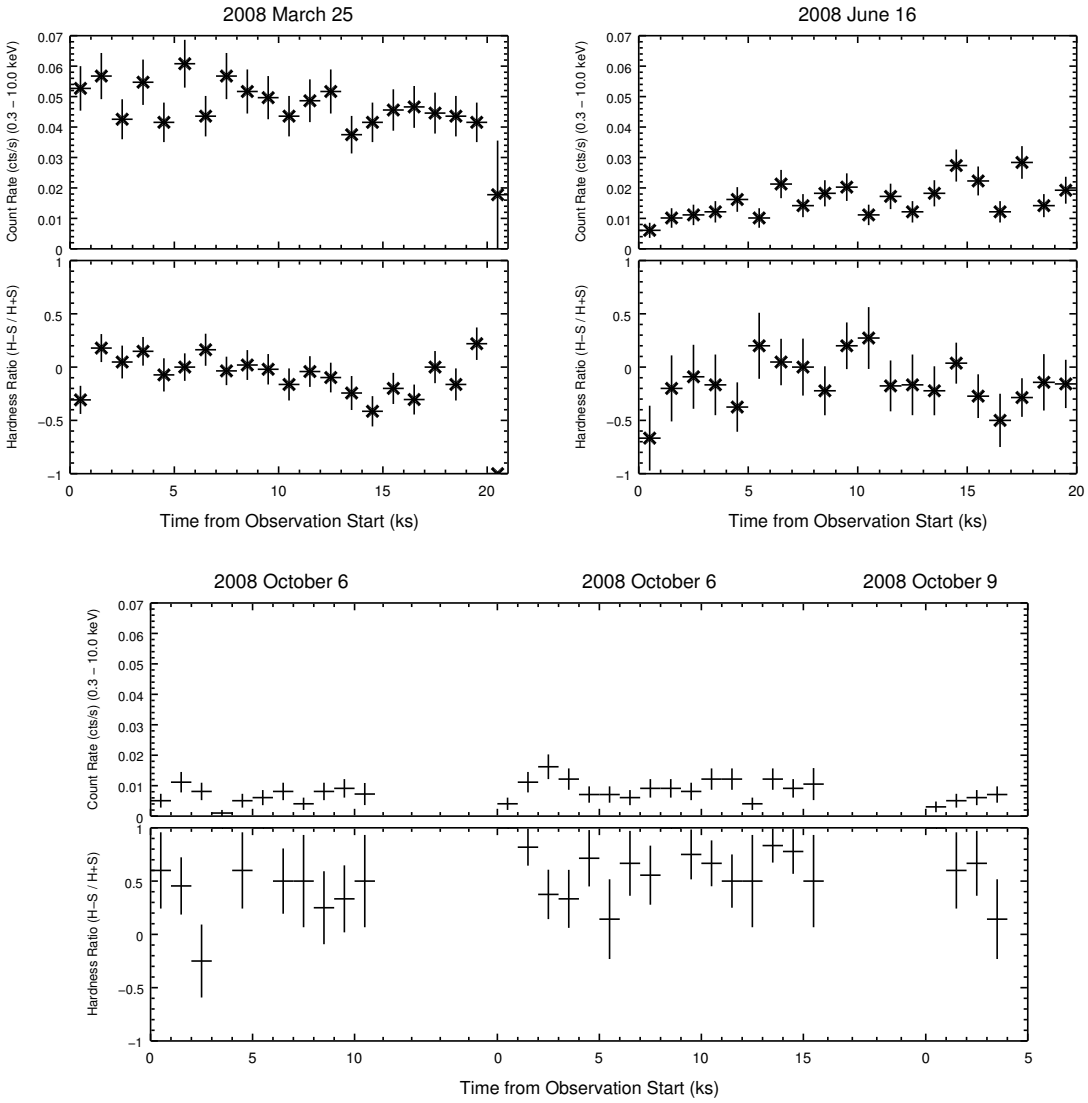


Figure 24: Background-subtracted X-ray light curves (top panes of each panel) and hardness ratio curves (bottom panes of each panel) for the 2008 CXO observations of EX Lupi. Time bins are 1 ks each, and the soft and hard energy bands are 0.3–1.2 keV and 1.2–10 keV, respectively. Plotted uncertainties in hardness ratios and count rates are $1\sigma$. The light curves and hardness ratio curves for the three 2008 October observations have been concatenated in the bottom panel with arbitrary time gaps between observations.

## 5.3 Results from X-ray Observations

### 5.3.1 General Spectral Characteristics Indicating Accretion

The data indicate that X-ray spectrum of EX Lupi consisted of a bright source of relatively soft X-rays immediately after the outburst but had changed to a faint source of harder X-rays by the end of the outburst. Table 5 gives the mean count rates, median photon energies, and hardness ratios of the spectra of EX Lupi for the 2008 CXO observations, and Figure 25 illustrates the temporal changes in these properties of the X-ray spectra and the correlation between the decline in the V band and the decrease in X-ray flux. Immediately following the onset of the optical outburst, the X-ray count rate is high, the median photon energy is soft, and the hardness ratio[5] is modestly negative. Approximately three months later, the X-ray count rate had decreased by a factor of $\sim$3, and the median photon energy and hardness ratio were roughly unchanged. In 2008 October, approximately six months after the first X-ray observation of EX Lupi and roughly eight months after the onset of the optical outburst, the X-ray count rate had declined to roughly one-sixth of its 2008 March 25 value, the median photon energy had increased by a factor of $\sim$1.5, and the hardness ratio had become significantly positive.

### 5.3.2 Spectral Modeling

In modeling the EX Lupi spectra, we employed XSPEC v12.4. First, we computed models with a thin, single-temperature plasma (APEC model) subject to absorption

[5]Hardness ratio = (H–S/H+S), where S is defined as the soft X-ray band (0.3–1.2 keV) and H is the hard X-ray band (1.2–10.0 keV).

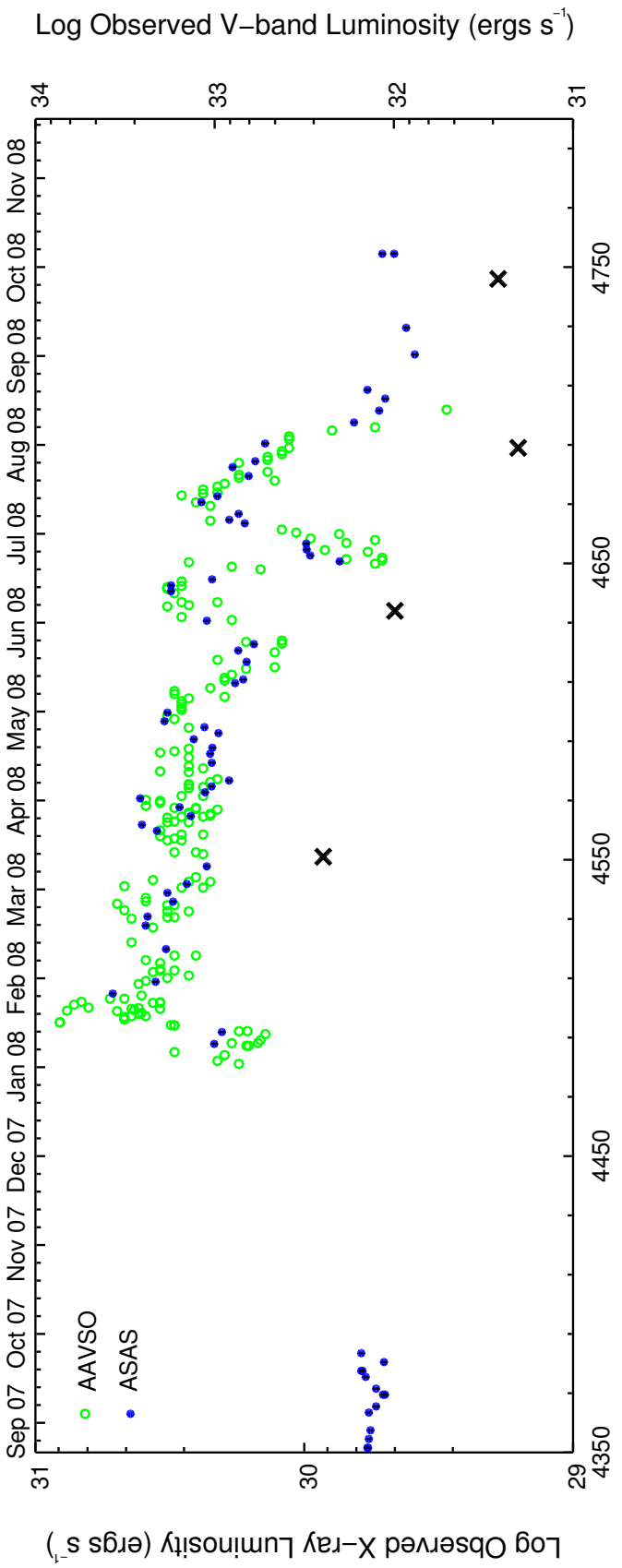


Figure 25: Optical and X-ray light curves of EX Lupi during the 2008 outburst. After the onset of the optical outburst of EX Lupi, the observed X-ray (crosses) luminosity decreased as the V-band (blue and green circles) luminosity decreased. Error bars (one sigma) are typically smaller than the plotted symbols. During the 2008 outburst, the optical light curve shows strong evidence for a ∼37 day periodicity.

by an intervening column of hydrogen (WABS component). Parameters for the hydrogen column density ("HCD") and the plasma temperature were initially set to $N_H = 1{\times}10^{22}$ cm$^{-2}$ and $kT_X = 0.5$ keV, respectively, while the chemical abundances were set to values found in the XEST survey (Güdel et al., 2007), consistent with the approach in Grosso et al. (2010). Next, we fit the data with a two-component model, using these same starting parameters for the first plasma, but with the second plasma component (subject to the same hydrogen column density) initially set to $kT_X = 2.0$ keV. Finally, we again reset the two-component plasma model to the same starting parameters and incorporated a second intervening hydrogen column initially set to $N_H = 1{\times}10^{22}$ cm$^{-2}$. In all three models, the hydrogen column densities and plasma temperatures were allowed to vary while the chemical abundances remained fixed. Initial model parameter values were chosen to lie within the parameter range found by Grosso et al. (2010).

**2008 March** The spectrum of ObsID 8923 (Fig. 26) was obtained approximately two months after EX Lupi was first observed to be in an eruptive state. The single-component plasma ("1T") model can account for the X-ray emission at energies below 2 keV but is unable to account for most of the X-ray emission from ∼2 to 6 keV. We find that this spectrum is fit best (F-test probability[6] = 4.5 $\times10^{-6}$) with the two-component plasma ("2T") model (Table 6) with temperatures of 0.4 keV and 1.7 keV suffering extinction from a single intervening absorbing column of $N_H$=0.4 $\times10^{22}$

[6]F-test probability provides an assessment of the improvement in using one model versus another and is calculated from the chi-squared and degrees-of-freedom values of the two model fits using the XSPEC *ftest* command. An F-test probability much less than unity (usually $\lesssim$0.05) suggests that it is very to add the additional model component.

$cm^{-2}$. The lower-temperature component contributes roughly four times more X-ray flux (as derived from absorption-corrected models) than the higher-temperature component and accounts for most of the emission up to energies of $\sim$1.5 keV. The addition of another parameter describing the absorption toward the second (hotter) plasma component does not improve the fit (F-test probability = 0.92) for this particular observation, as the value of the second hydrogen column density converges to the same value as the first.

Table 6. Best-Fit Models for EX Lupi Observations

| ObsID | Observation Date | Observation Time | Reduced $\chi^2$ | Degrees of Freedom | $N_H$ ($\times 10^{22}$ cm$^{-2}$) | $kT_X$ (keV) | EM ($\times 10^{53}$ cm$^{-3}$) | Plasma Component $F_X$ ($\times 10^{-13}$ ergs cm$^{-2}$ s$^{-1}$) | Total Observed $L_X$ ($\times 10^{29}$ ergs s$^{-1}$) |
|---|---|---|---|---|---|---|---|---|---|
| 8923 | 2008 Mar 25 | 22:29:38 | 0.92 | 90 | $0.4^{+0.2}_{-0.2}$ | $0.4^{+0.3}_{-0.1}$ | $3.1^{+4.9}_{-2.0}$ | 9.8 | 8.5 |
| | | | | | ... | $1.7^{+0.6}_{-0.4}$ | $0.7^{+0.4}_{-0.2}$ | 2.5 | |
| 8924 | 2008 Jun 16 | 22:06:06 | 0.90 | 42 | $0.01^{+0.13}_{-0.01}$ | $0.5^{+0.1}_{-0.1}$ | $0.2^{+0.1}_{-0.1}$ | 0.8 | 4.6 |
| | | | | | $1.7^{+3.5}_{-0.8}$ | $0.7^{+1.0}_{-0.4}$ | $0.9^{+17.6}_{-0.7}$ | 3.2 | |
| | | | | | $\sim$40 | $\sim$4 | $\sim$1 | 5.7 | |
| XMM[a] | 2008 Aug 10 | | 0.87 | 12 | $0.04^{+0.11}_{-0.04}$ | $0.4^{+0.3}_{-0.1}$ | $0.04^{+0.04}_{-0.01}$ | 0.1 | 1.6 |
| | | | | | $2.7^{+4.6}_{-2.3}$ | $4.6^{+N/A}_{-3.0}$ | $0.2^{+1.0}_{-0.1}$ | 1.1 | |
| 8925[b] | 2008 Oct 6 | 00:01:53 | 0.92 | 35 | $0.9^{+0.4}_{-0.4}$ | $0.9^{+0.3}_{-0.4}$ | $0.5^{+1.0}_{-0.4}$ | 1.8 | 1.9 |
| 10789[b] | 2008 Oct 6 | 17:32:36 | | | $3.8^{+13.5}_{-3.0}$ | $2.3^{+27.1}_{-1.4}$ | $0.3^{+1.1}_{-0.3}$ | 1.4 | |
| 10791[b] | 2008 Oct 9 | 12:08:54 | | | | | | | |

[a]Here we only report the spectral model of the low-level period (first row of Table 1 of Grosso et al. (2010)).

[b]Parameter values are derived from the combined spectra of the three 2008 October observations.

Note. — Uncertainties given for hydrogen column density and plasma temperature correspond to the 90% confidence intervals. Emission measures and luminosities assume a distance of 155 pc to EX Lupi. X-ray fluxes for each of the plasma components have been corrected for absorption; however, the total observed X-ray luminosities are not corrected for absorption and give the total X-ray flux derived from the modeling procedure. X-ray fluxes and luminosities are derived for the 0.2–10.0 keV energy range. All chemical abundances are fixed at XEST values. Due to poor constraints on the third plasma component of the 2008 June spectrum model, the error ranges have been omitted and the best-fit values are given only.

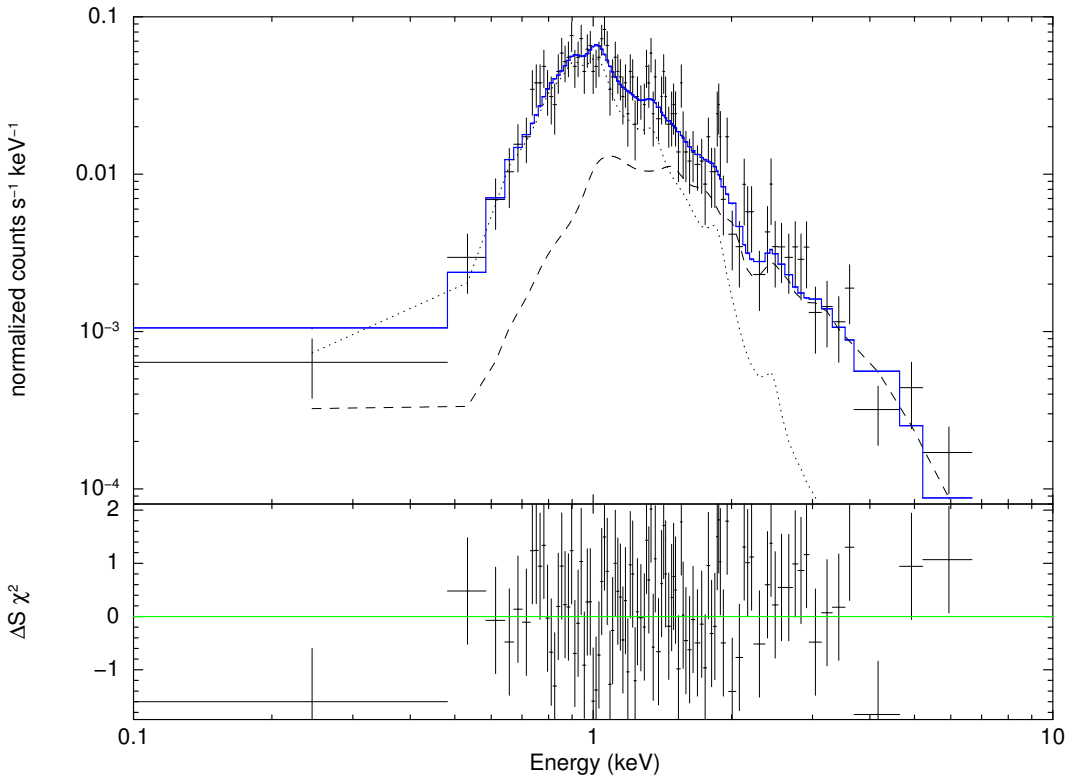


Figure 26: The best-fit two-component XSPEC model of the 2008 March EX Lupi spectrum (data binned to five-count-minimum bins) is displayed (blue line) in the top panel. The horizontal lines for each of the data points represent the bin widths, and the vertical lines represent the one-sigma error bars. The dotted and dashed lines represent the absorbed contributions from the lower-temperature and higher-temperature plasma components, respectively.

**2008 June** The spectrum of ObsID 8924 (Fig. 27), when compared to the other two CXO observations of EX Lupi, appears to have "excess" X-ray flux at energies above ∼4 keV (see §3.3). This emission does not appear to be present in the 2008 August XMM-Newton observation (Grosso et al., 2010) either. Like the 2008 March spectrum, we first fit this spectrum with a single-component plasma, but the model was unable to account for emission above ∼2 keV. Fitting the spectrum to a two-

component plasma, subject to a single hydrogen column density, resulted in a better fit of the spectrum past ∼2 keV but a poor fit to the spectrum beyond ∼4 keV. We note that this model converged to a fit with a very low hydrogen column density (0.05 $\times 10^{22}$ cm$^{-2}$) in comparison to the hydrogen column density that provided the best fit to the 2008 March spectrum, though this low column density is very similar to one of the hydrogen column densities found by Grosso et al. (2010) for the 2008 August X-ray spectrum. The temperature of the hotter plasma component in this model (0.5 keV and 11.6 keV) is not well constrained, and we find that the emission beyond ∼4 keV is not well accounted for. The addition of a second hydrogen column density resulted in the fit of the hotter plasma component diverging to an unrealistic temperature. We conclude that this two-component model is not adequate for modeling this spectrum.

We then fit the spectrum with a three-component plasma model with each plasma component subject to a separate hydrogen column density (Table 6). In order to have some control over the fitting algorithm, we first modeled the spectrum up to the ∼4.5 keV energy range (the portion of this X-ray spectrum that was visually similar to the 2008 March spectrum) with a two-temperature/two-hydrogen column density model, which yielded a good fit to this portion of the spectrum. We then fixed those parameter values, reset the modeled energy range to include all of the energy spectrum, and added the third hydrogen column density and plasma components to the model. We held the chemical abundances fixed but allowed all other parameters to vary and reran the model, allowing the parameters to adjust to find the best fit. The addition of the third plasma component improved the fit for the entire spectrum (F-test probabilities, when going from a 1HCD/2T model and a 2HCD/2T model to a

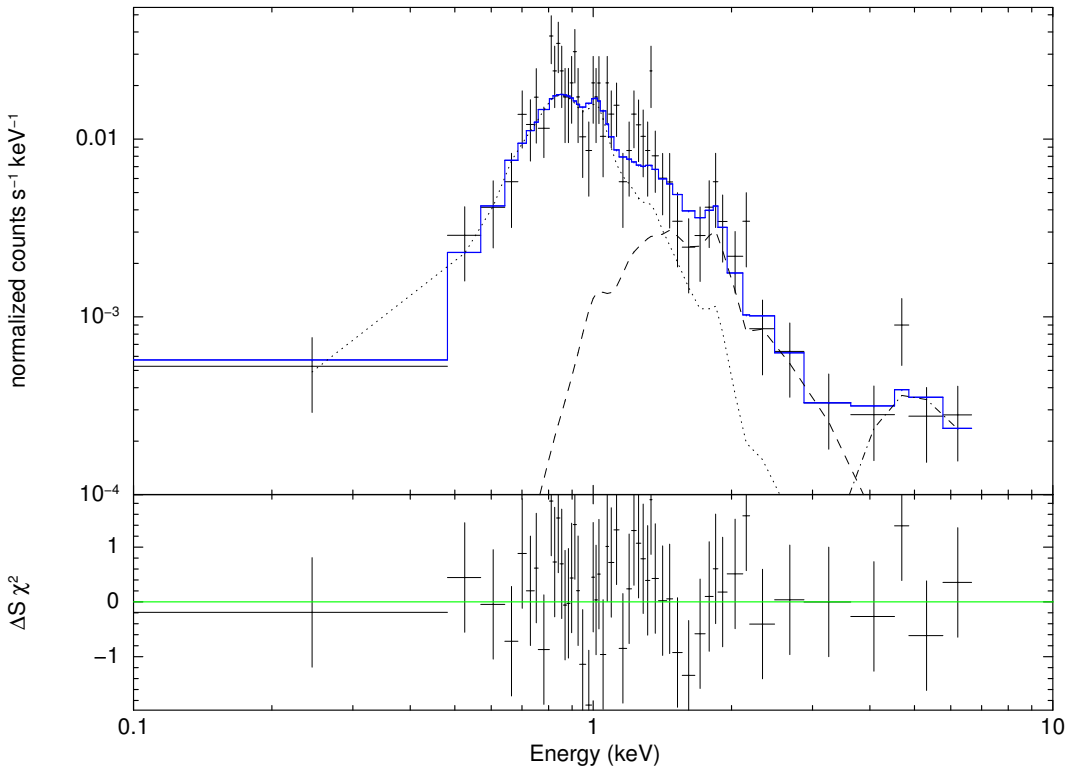


Figure 27: The best-fit three-component XSPEC model of the 2008 June EX Lupi spectrum (data binned to five-count-minimum bins) is displayed (blue line) in the top panel. Residuals to the fit are given in the bottom panel. The emission above ∼4 keV does not appear to be present in the other X-ray observations of EX Lupi during the 2008 outburst. The remaining lines represent the absorbed contributions from the 0.5 keV (dotted line), 0.7 keV (dashed line), and ∼4 keV (dash-dotted) plasma components.

3HCD/3T model, are 0.08 and 0.05, respectively, which suggests that the 3HCD/3T model is an improvement over the 1HCD/2T or the 2HCD/2T model). The ∼4 keV plasma component does not have a well-constrained temperature or hydrogen column density, but we find that the higher-energy portion of the 2008 June spectrum is not adequately fit without the additional plasma component *and* hydrogen column density. Therefore, we conclude that our 2HCD/2T model fits the 2008 June 16 spectrum well up to energies of ∼4 keV; however, the models show that this spectrum

does require a third, heavily-absorbed plasma component in order to characterize it more completely.

As shown in Figure 27, the prominent emission past ∼4.5 keV is contributed by the most heavily-absorbed plasma component with a plasma temperature of ∼4 keV. The additional hydrogen column density, which is over an order of magnitude greater than the second-highest column density of this observation, is required to quench the lower-energy portion of the spectrum of the ∼4 keV plasma such that only the higher-energy portion is able to contribute to the 2008 June spectrum. We also find that the light curve of ObsID 8924 (Fig. 24, top right panel) did not indicate any large-scale variability during the 20 ks observing period, and the spectrum hardness ratio throughout this observation remained at a constant level. Therefore, it does not appear that there were any flaring events that might have contributed to the appearance of the third plasma component during only a short portion of the observation. One interpretation of this spectral behavior is that the accretion rate had decreased enough by 2008 June 16 that we were able to detect the X-ray signature of the corona itself; this interpretation is discussed later in Section 5.3.3.

**2008 October** We find that the best-fit model for the 2008 October combined spectrum of EX Lupi (Fig. 28) is a two-component plasma with each component subject to absorption from a different hydrogen column density (Table 3). The F-test probabilities of using a 2HCD/2T model instead of 1HCD/1T and 1HCD/2T models were 0.08 and 0.05, respectively. The best-fit model includes both a low-temperature plasma with a modest column density and a high-temperature plasma

with a larger column density. The emission measures and unabsorbed plasma X-ray fluxes are comparable for the two components; however, the best-fit values of these parameters are significantly higher than those of the cooler plasma component during the 2008 August 10 observation and roughly twice as high as those of the hotter plasma component during that exposure.

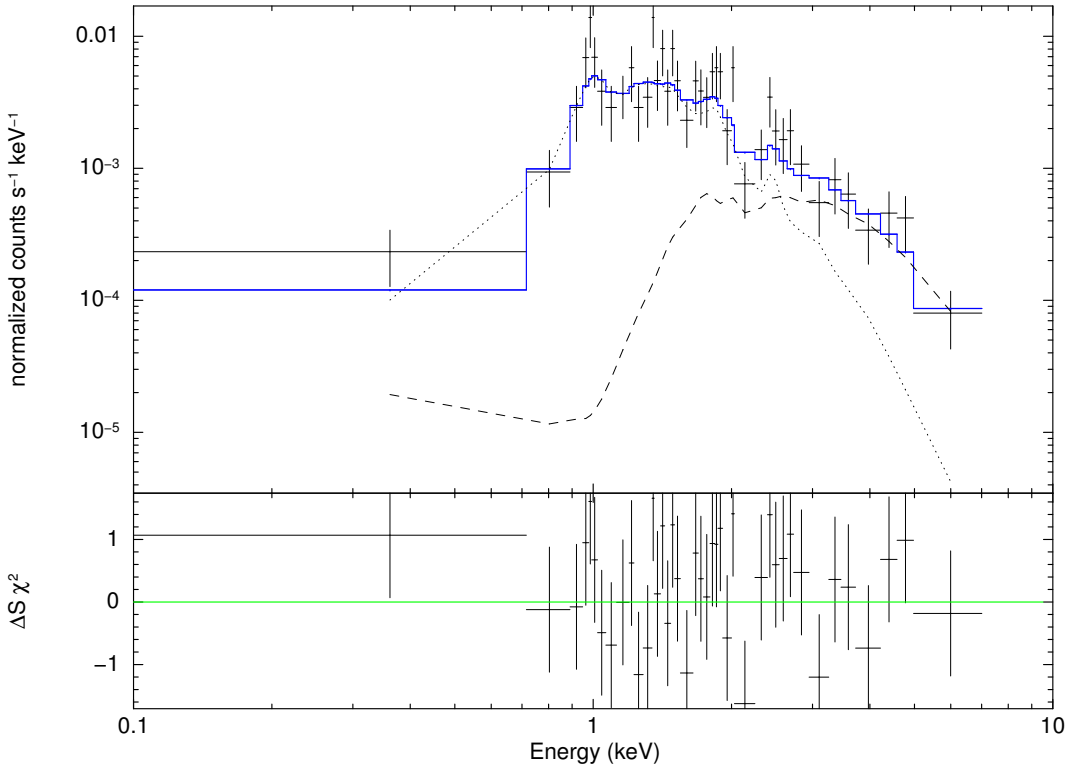


Figure 28: The best-fit XSPEC model of the 2008 October EX Lupi composite spectrum data (binned to five-count-minimum bins) is displayed (blue line) in the top panel. Residuals to the fit are given in the bottom panel. The dotted and dashed lines represent the absorbed contributions from the lower-temperature and higher-temperature plasma components, respectively.

### 5.3.3 The Temporal Evolution of the Post-Outburst X-ray Plasma

From Figure 25, we see that EX Lupi began to gradually fade back toward quiescent optical levels immediately after the onset of the optical outburst in 2008 January. Comparing this trend to what was observed in the X-ray spectral characteristics as EX Lupi returned to optical quiescence (Tables 1 and 3), we see correlations that strongly suggest that the X-ray evolution and optical evolution of EX Lupi are linked. In 2008 March, when we observed that EX Lupi had a high X-ray count rate, the median photon energy was soft and the hardness ratio was modestly negative. In addition, the spectrum is best modeled by two plasmas, one with a temperature of $kT_X$=0.4 keV and another with a higher temperature of $kT_X$=1.7 keV. The lower-temperature component has an absorption-corrected flux that is roughly four times higher than the flux associated with the higher-temperature component, and its temperature is characteristic of plasma heated in shocks due to accretion of circumstellar material onto the stellar photosphere.

Roughly three months later, EX Lupi had declined modestly ($\sim$0.05 magnitudes) in optical flux while the X-ray count-rate had dropped to roughly one-third of the 2008 March level. The X-ray emitting plasma is best modeled by three different components, two of which were of similar low temperature but subject to absorption by different hydrogen column densities. Given their derived 90% confidence intervals, the lowest temperature plasma ($kT_X$=0.5 keV) could have been generated via an accretion hotspot, but the second, low-temperature plasma ($kT_X$=0.7 keV) is too hot to have been generated by an accretion hotspot. This plasma temperature is

consistent with the cooler plasma component found by Preibisch et al. (2005) in their X-ray spectral fits of many of the COUP sources. They found that for nearly all stars in their "optical sample" the cooler plasma components of their two-component plasma models had temperatures of ≈8–10 MK ($kT_X \approx 0.7$–$0.9$ keV). Brickhouse et al. (2010) also found evidence of a similar plasma component in TW Hya from the presence and ratios of certain emission lines; they interpreted that this component was possibly due to "accretion-fed coronal loops" with temperatures around 10 MK. The third plasma component had an X-ray temperature of ∼4 keV, which is too high to be generated at an accretion hotspot; however, it is possible that this hotter plasma could be due to magnetic reconnection events in the accretion stream, as we proposed for V1647 Ori (Teets et al., 2011). We find that the coolest plasma of the 2008 June 16 observation had an emission measure that was approximately one-fourth that of the other, hotter plasmas. This is in stark contrast to the results of the 2008 March 25 spectral model, which showed a cooler plasma with roughly four times the emission measure and absorption-corrected X-ray flux as that of the hotter plasma. This suggests that the amount of accretion shock-generated X-ray plasma had decreased significantly over a span of three months; however, since there had only been a very modest decrease in the optical flux of EX Lupi by 2008 June 16, accretion apparently was still occurring during this CXO observation. Though there had been a sharp decline in softer X-ray flux (by a factor of ∼3) since 2008 March 25, the overall level of X-ray flux remained quite high (as shown by the absorption-corrected flux levels), including a significant contribution from the heavily-absorbed third plasma component.

Figure 29 shows the three CXO spectra of EX Lupi overlaid with a simulated spectrum of the 2008 August XMM-Newton (low-level period in Table 1 of Grosso et al. (2010)) after being convolved with a CXO response. We see that over time the softer portion ($\lesssim$4 keV) of the X-ray spectrum of EX Lupi diminishes as the accretion rate decreases; however, the harder portion remains at roughly the same level. Thus, while it appears that there is an X-ray "excess" at energies above ($\gtrsim$4 keV) in the 2008 June X-ray spectrum of EX Lupi, it appears that the excess is actually the X-ray signature of the active coronal plasma, which is otherwise present at a nearly constant level during all observing epochs.

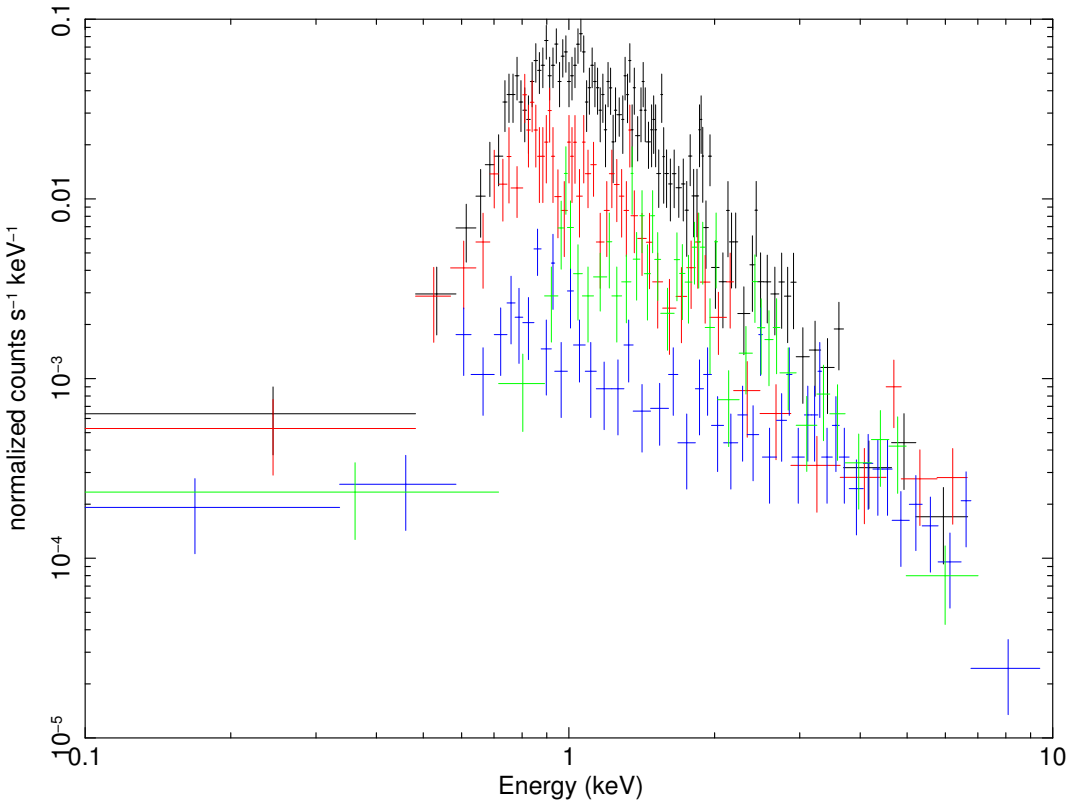


Figure 29: Overlay of the three 2008 EX Lupi CXO spectra (March - black, June - red, and October - green) and the 2008 August XMM-Newton spectral model of the low-level period (blue) from Grosso et al. (2010) convolved with a CXO response. While the softer portion of the spectrum of EX Lupi decreases over time as accretion diminishes, the 4–10 keV range appears mostly unchanged over the same time interval (i.e., the 2008 June 16 X-ray spectrum does not seem to have an excess above $\sim$4 keV). Thus, it appears that we are detecting the X-ray emission from the active corona of EX Lupi in this spectral range.

From 2008 June to August, the plasma temperature appears to have remained largely unchanged, although the emission measure dropped dramatically. Grosso et al. (2010) found evidence for two X-ray plasmas in the 2008 August spectrum, one of which (0.4 keV) is nearly identical to the 0.4 keV plasma seen in March and the 0.5 keV plasma seen in June, which we have already identified as likely generated at an accretion footprint. The emission measure of this low-temperature plasma, however, which had dropped by two-thirds from March to June, by August had dropped to about one percent of the original (March) value. The accretion phase for EX Lupi, as seen in X-rays, apparently was nearing its end. This conclusion is supported by the optical measurements, in which the V band magnitude had dropped at least 1.5 magnitudes from March to August and was in the middle of a precipitous descent back to its quiescent magnitude, which it would reach in only ten more days (Fig. 25).

In August, during the low-level period observed with XMM-Newton, the hotter plasma component had a temperature and emission measure (within the 90% confidence intervals) very similar to the hotter plasma component that was observed in the 2008 March 25 spectrum of EX Lupi. Given that its temperature is too high to be generated by an accretion shock and the optical flux had returned to its quiescent level, the hotter plasma component is most likely associated with coronal activity. Moreover, in August, this hotter plasma component exhibited flaring activity (Grosso et al., 2010).

By October, when the V-band flux had returned to the pre-outburst level, the X-ray count rate of EX Lupi had declined by another factor of two, the median X-

ray photon energy had jumped by ∼0.6 keV, and the hardness ratio had become significantly positive. The 2008 October spectrum of EX Lupi is best modeled with two plasma components; however, even taking into consideration the 90% confidence intervals of the modeled plasma temperatures, we find that the two plasmas are too hot to be generated by an accretion hotspot. Thus, the hotspot plasma signature detected in the spectrum of EX Lupi in the months prior had declined to levels below the detection threshold, supporting the conclusion that once the optical eruption had ended, the X-ray flux had returned to levels typical for EX Lupi in a low accretion state. The higher-temperature plasma component and its associated column density are similar to the high temperature plasma component seen in June and in August. The total emission measure in October is only about 20% that of March. These results suggest that the several-keV plasma that is associated with a total emission measure of about $\sim 8 \times 10^{23}$ cm$^{-3}$ is the recovered X-ray signature of the quiescent corona of EX Lupi and that its spectrum likely includes a "quiescent mass accretion rate" component that is too low to produce a large observable excess in the CXO X-ray spectrum.

The fits of the 2008 June, August, and October observations of EX Lupi all improve with spectral models that have more than one hydrogen column density component. It is likely the case that the contribution of the lower-temperature plasma during the 2008 March 25 observation overwhelmed the signal at the lower end of the energy spectrum for the second, higher-temperature plasma and that, coupled with the level of noise in the spectrum during the observation, the derived single X-ray-absorbing column was adequate to account for the absorption suffered by both plasmas. By 2008

June, however, the X-ray flux from the dominant, lower-temperature plasma had decreased enough that the lower-energy end of the spectrum of the higher-temperature plasma became noticeable and our modeling was sensitive enough so as to require the presence of a second parameter in order to account for the intervening absorbing column toward the hotter component.

The X-ray behavior of EX Lupi during the 2008 outburst is similar to what was observed in the X-ray and optical/near-infrared behavior during the 2005 optical outburst of V1118 Ori. For the duration of the 2005 optical outburst, the optical and near-infrared fluxes of V1118 Ori varied by a factor of 2–10 while the X-ray flux was found to vary only by a factor of 2. In addition, the X-ray-emitting plasma of V1118 Ori was shown to be cooler during the outburst than during optical quiescence, suggesting that the X-ray plasma temperature change was likely due to enhanced accretion onto the star (Audard et al., 2005, 2010). During the 2008 outburst of EX Lupi, we observed that the optical flux varied by a factor of 50–100 while the X-ray flux changed by a factor of 4–5. As EX Lupi returned to optical quiescence, the X-ray plasma temperature generally increased. Once EX Lupi had returned to optical quiescence, the X-ray plasma temperature was similar to that observed for V1118 during optical quiescence.

These observed trends are in sharp contrast to what was observed during multiple X-ray and optical/near-infrared observations of the erupting pre-main sequence star, V1647 Ori. During the 2003 and 2008 optical eruptions, X-ray observations of V1647 Ori revealed that the X-ray plasma temperature was on the order of $\sim$4 keV while the X-ray plasma temperature was significantly cooler during optical quiescence ($\sim$1

keV) (Teets et al., 2011). In addition, the optical flux of V1647 Ori varied by a factor of 60–100 between quiescent and eruptive phases while the X-ray flux varied more by a factor of 150–500, suggesting that although X-rays are the result of accretion in both cases, the X-ray generation mechanisms themselves were different for these two eruptive pre-main sequence stars. The estimate of the mass accretion rate of EX Lupi during the 2008 optical outburst is very similar to the value of (4–7)$\times 10^{-7}$ $M_{\odot}$ $yr^{-1}$ derived by Lorenzetti et al. (2009) for V1118 Ori (on 2005 September 10, i.e., during the outburst) from the luminosities of emission line Pa$\beta$ and Br$\gamma$. By contrast, the outburst mass accretion rate of V1647 Ori was about 1,000 times larger. Therefore, we propose that the X-ray flux is enhanced as the mass accretion rate is enhanced during the optical outburst. During the optical outburst of V1647 Ori, the high level of accretion should have generated a large number of accretion-fed loops, which are reservoirs of hotter plasma than what would be found in accretion footprints (Brickhouse et al., 2010) and are locations in which magnetic reconnection events would occur.

### 5.4 Optical Variability During the 2008 Outburst

Figure 25 shows V-band data from the All-Sky Automated Survey (ASAS) telescope and the American Association of Variable Star Observers (AAVSO) database. ASAS data used in the figure were only those data flagged as photometric. Close inspection of the EX Lupi optical light curve during the 2008 outburst reveals that EX Lupi appears to have exhibited a periodic variation in its optical flux, with a period of approximately 35 to 40 days. We constructed Lomb-Scargle periodograms

to test this light curve for possible periodicities and determine which, if any, periodicities are likely real via their corresponding false-alarm probabilities (Scargle, 1982). With the ASAS magnitudes in our optical data set being of higher quality than the AAVSO magnitudes (since AAVSO data were obtained through visual estimations of the magnitude of EX Lupi), we first used only the ASAS data (48 data points from JD 2454504.8 to 2454697.6) in the periodicity analysis. We subjected the data to the IDL routine *linfit*, calculated a linear fit, and then ran the linear-fit-subtracted data through an IDL Lomb-Scargle periodogram routine[7] to search through 2500 possible periods. The results reveal a 37 day period that appears to be much more significant than all other possible periods identified in this analysis. From the possible identified periods (Fig. 30, top panel), only a period of 37 days has a false-alarm probability ("FAP") of less than 0.01, which corresponds to a confidence level of 99%. The next strongest period had a FAP greater than 0.99 and so is almost certainly not real. We reran the same analysis using both the ASAS and AAVSO data (the AAVSO data was selected to be within the same time range as that of the ASAS data). In the resultant periodogram (Fig. 30, bottom panel), the strongest signal corresponds to a period of 36.5 days and a FAP of less than 0.01. The second strongest signal (a period of ∼28 days) had a very high FAP of 0.88. It therefore appears that the ∼37 day period, and only the ∼37 day period, is real.

[7]The IDL routine is available from Institut für Astronomie und Astrophysik at http://astro.uni-tuebingen.de/software/idl/aitlib/timing/scargle.html

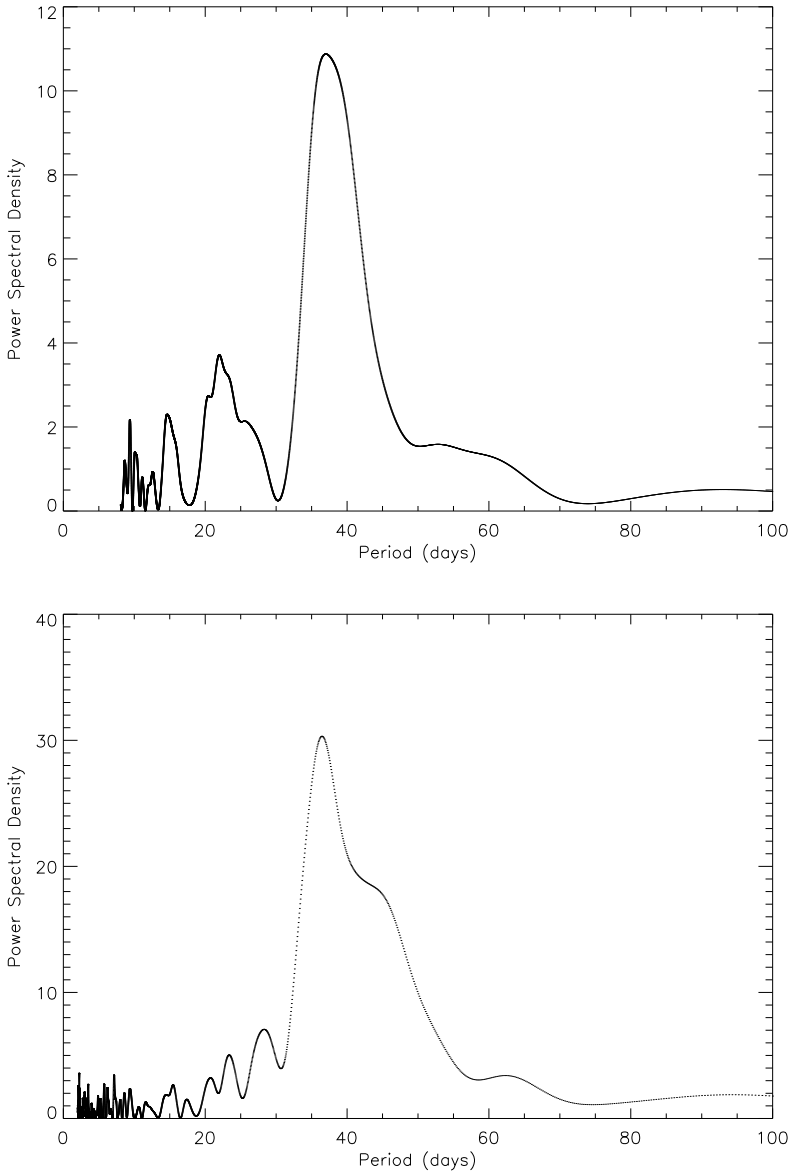


Figure 30: Periodograms of the optical light curve of EX Lupi derived from data obtained during the 2008 outburst. The top panel uses ASAS data only, and the bottom panel uses both ASAS and AAVSO data. In each panel, the strongest signal corresponds to a period of $\sim 37$ days and is within the 99% confidence interval (FAP $< 0.01$).

We note that in the above analysis, we searched for a periodicity in the optical light curve of EX Lupi only during the outburst phase, from 2008 January through October. If this periodicity is present only during the outburst phase, it is probably associated in some way with accretion. As a check for this, we applied the same analysis procedures to optical magnitudes of EX Lupi obtained from the AAVSO database over a period beginning about five years before the outburst and ending almost two years before the outburst (Julian dates 2451999.204 to 2453915). Due to the greater length of time these observations span, we increased the period search number from 2500 to 20000.

The Lomb-Scargle periodogram analysis reveals hundreds of insignificant potential periods (FAP values greater than 0.995, meaning they have at least a 99.5% chance of being random in this data set) at virtually all time periods from a day to hundreds of days. None of these are likely real. For the time frame of greatest interest to us, as we are trying to determine whether the 37 day period detected during the outburst is also present before the eruption, we present in Figure 31 the Lomb-Scargle periodogram analysis for periods ranging from 28 to 50 days, centered approximately on the known 37 day period. The plot reveals a dozen or more peaks, all of weak strength, with periods between 28 and 48 days. The peak closest to 37 days lies at 36.8 days and has a FAP value of 0.999; therefore, this peak is not significant, and neither are any of the other peaks seen in this periodogram. Thus, the data shows that the 37 day period that was present during the outburst, from January through October of 2008, did not exist prior to the outburst.

D'Angelo & Spruit (2012) interpreted the timescale of periodicity found in the

light curve of this class of object (eruptive, rapidly-accreting pre-main sequence stars) in the context of mass possibly becoming "trapped" at the corotation radius of the accretion disk and cyclically accreting onto the star. D'Angelo & Spruit (2012) noted the ∼30 day periodicity during the outburst of EX Lupi, citing it as evidence for such "mass trapping." Our analysis supports their assertion and further refines the likely periodicity timescale.

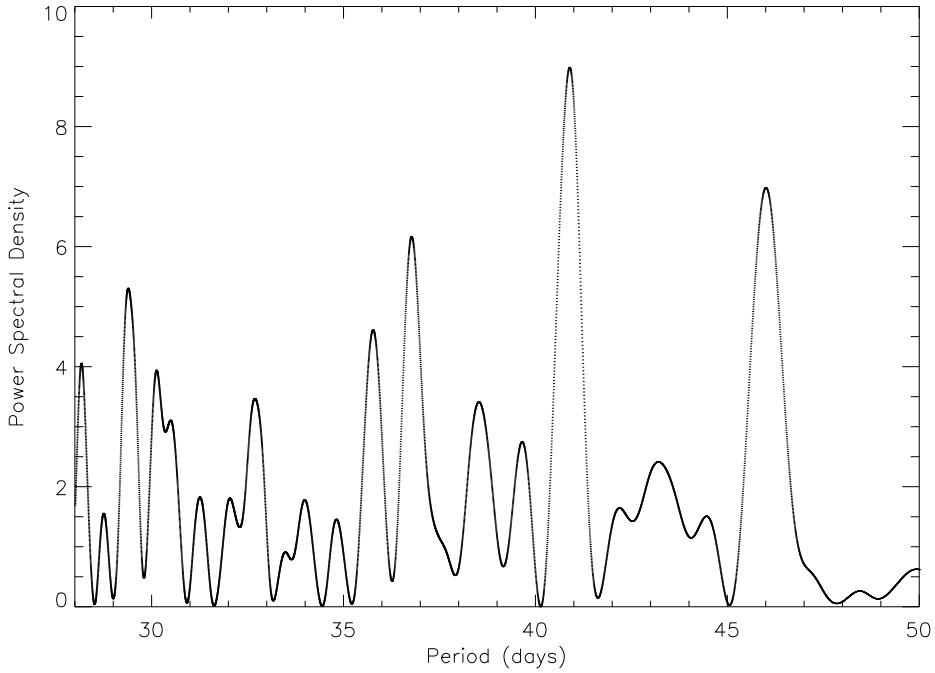


Figure 31: Periodogram of the light curve of EX Lupi obtained during the optically quiescent period before the 2008 eruption. All of the peaks lie well below the 0.1% confidence level (equivalent to a power spectral density value of 8), except for the peak at ∼41 days, which is roughly at the 10% confidence level.

## 5.5 Discussion & Conclusions

The optical outbursts of eruptive objects, such as EXors and FUors, are thought to be the result of sudden, large-scale accretion events. Accretion of circumstellar gas should result in the production of a relatively low-temperature, X-ray-generating plasma as free-falling material impacts the stellar photosphere and is shock-heated to temperatures of a few million Kelvin at the accretion stream footprint in the stellar photosphere. If the intervening hydrogen column density is low enough and the emission measure of the shock-heated plasma is large enough, then we should be able to detect this X-ray flux component – as is clearly the case for EX Lupi – as well as the hotter coronal X-ray emission resulting from non-accretion-related magnetic activity (see Grosso et al., 2010). As the accretion subsides and the X-ray output of the accretion footprint diminishes, the softer X-ray flux should decrease, resulting in the median photon energy increasing, the hardness ratio becoming less negative, and an overall decrease in X-ray flux. Given that all three of these correlations are observed in the X-ray spectrum as time progresses and the optical flux levels of EX Lupi return to quiescent levels as the accretion event subsides, the hypothesis that the elevated X-ray flux observed during the 2008 outburst was generated via circumstellar accretion onto the stellar photosphere is strongly supported.

Similar correlations were documented in optical, near-infrared, and X-ray observations of the young, PMS V1647 Ori when it was observed to erupt in 2003 and then again in 2008 (Teets et al., 2011). In the case of V1647 Ori, however, the CXO spectra showed no evidence for the soft X-ray component that should be generated by

accretion. Teets et al. (2011) interpreted the large increase and subsequent decrease in hard X-ray flux from V1647 Ori to be the result of accretion and explained the absence of an observed soft X-ray component during the accretion episode as a consequence of very high intervening hydrogen column density. The observed increase in the hard X-ray flux was thought to originate in the accretion funnels from magnetic reconnection events. As accretion subsided, the hard X-ray flux decreased as well.

During the 2008 outburst of EX Lupi, we first observed a two-component plasma, with one component consisting of a plasma with a temperature characteristic of shock-heated accreting material and the other component consisting of a plasma with a temperature much higher and characteristic of those temperatures found in the V1647 Ori observations by CXO (Kastner et al., 2004, 2006; Teets et al., 2011), XMM-Newton (Grosso et al., 2005), and Suzaku (Hamaguchi et al., 2010). As time passed and the accretion subsided, the X-ray spectrum of EX Lupi changed such that the lower-temperature component emission measure and flux level decreased while the hotter plasma component's emission measure and flux level generally decreased as well. After the accretion episode ended, the spectrum was characterized by faint emission from hotter plasma characteristic of coronal activity. This sequence of changes follows the expected pattern of spectral changes if the elevated X-ray flux is accretion shock-generated and the column density is low enough that we can detect soft X-rays generated in or near the photosphere. In addition, an elevated level of harder X-rays during the optical outburst may also be associated with magnetic reconnection events in or near the accretion-fed loops and/or the accretion funnels.

# CHAPTER VI

## DISCUSSION AND CONCLUSIONS

Our analysis of the X-ray observations of V1647 Ori and EX Lupi have given us insight into how young stars, still in the final formation phases, are able to generate copious amounts of X-ray flux. Using optical and infrared flux measurements obtained during the optical outbursts of these objects, I have been able to show that there are strong correlations between the increases and decreases in X-ray flux and increases and decreases in optical and/or near-infrared for these two YSOs when they undergo large optical outbursts. These correlations strongly suggest that accretion, which is already well established as the cause of the substantial variations observed in the visible and near-infrared fluxes, is also the driver for the observed correlated increases and decreases in X-ray flux.

In the case of V1647 Ori, we found that the X-ray spectrum of this YSO is best modeled with a single, high-temperature plasma component that is too hot to be generated by an accretion footprint. In addition, the X-ray plasma temperature of V1647 Ori increased significantly during the optical outbursts as compared to its pre-outburst level. The large increase in X-ray flux, as well as the hardening of the X-ray spectrum, is so well temporally correlated with the changes observed in the optical and near-infrared flux that we can only conclude that the behavior observed in these three wavelength regimes is the result of accretion. In addition, we have observed this same correlation during the two observed outbursts of this object. The

high hydrogen column density for this object would have absorbed X-ray emission from a low-temperature plasma coming from below it (i.e., the photosphere), so it is not surprising that we were not able to detect the accretion footprint signature in the X-ray spectra.

Unlike V1647 Ori, EX Lupi has been observed to undergo many optical outbursts. We were fortunate to be able to use CXO to monitor this star in X-rays during its last observed optical outburst, starting soon after the onset of the outburst until shortly after it had returned to a quiescent state. We found that shortly after the onset of the optical outburst, the X-ray spectrum was characterized by two plasma components: a brighter, cooler component characteristic of an accretion footprint and a cooler, hotter component characteristic of coronal emission. As EX Lupi returned to a more quiescent optical level, the cooler component faded, which is exactly what was expected when the accretion event ended. Finally, once EX Lupi returned to quiescence, the X-ray spectrum was characterized by hot plasmas typical of normal coronal emission.

In the case of EX Lupi, we do have the smoking gun of accretion-generated X-rays – X-ray emission from a source with a temperature characteristic of an accretion hotspot that fades as accretion subsides. With V1647 Ori, we still have a strong X-ray/optical/near-infrared correlation, but the case made for accretion-generated X-ray emission would be firmer if other observations could disentangle coronal X-ray emission from X-rays produced from magnetic reconnection events in accretion streams. One possible means would be high-resolution X-ray spectroscopy of a source like V1647 Ori during an optical outburst. Line profiles might permit temperature-

sensitive line diagnostics that would allow us to probe for lower-temperature X-ray plasma signatures that are heavily extincted by high column densities.

As is usually the case with all targets of interest, more observations these objects will enable us to learn more, especially about how and where X-rays are generated via accretion. Obtaining additional X-ray data that can provide us with a different perspective of accretion-generated X-rays, such as HETGS data, might enable us to determine other factors about accretion, such as calculating accretion rates and luminosities. We can only hope that we catch enigmatic objects, such as V1647 Ori and EX Lupi, at the onset of future eruptions so that further X-ray observations can be obtained.

# REFERENCES

Ábrahám, P., Kóspál, A., Csizmadia, S., Moór, A., Kun, M., & Stringfellow, G. 2004, A&A, 419, L39

Acosta-Pulido, J. A., et al. 2007, AJ, 133, 2020

Anthony-Twarog, B.J. The H-beta distance scale for B stars - The Orion association, AJ, 87, 1213-1222 (1982)

Armitage, P. J., Livio, M., & Pringle, J. E. 2001, MNRAS, 324, 705

Arnaud, K.A., 1996, Astronomical Data Analysis Software and Systems V, eds. Jacoby G. and Barnes J., p17, ASP Conf. Series volume 101

Aspin, C., Beck, T. L., & Reipurth, B. 2008, ApJ, 135, 423

Aspin, C., et al. 2009, ApJ, 692, L67

Aspin, C., Reipurth, B., Herczeg, G. J., & Capak, P. 2010, ApJ, 719, L50

Audard, M. et al. 2005, ApJ, 635, L81

Audard, M., Briggs, K. R., Grosso, N., Güdel, M., Scelsi, L., Bouvier, J., & Telleschi, A. 2007, A&A, 468, 379

Audard, M., et al. 2010, A&A, 511, A63

Barnard, E. E. 1895, MNRAS, 55, 442

Becklin, E. E., Matthews, K., Neugebauer, G., & Willner, S. P. 1978, ApJ, 220, 83

Bell, K. R., Lin, D. N. C., & Ruden, S. P. 1991, ApJ, 372, 633

Bonnell, I., & Bastien, P. 1992, ApJ, 401, L31

Boss, A. P. 2009, ApJ, 697, 1940

Briceño, C., et al. 2004, ApJ, 606, L123

Brittain, S., Rettig, T., Simon, T., Gibb, E., & Liskowsky, J. 2010, ApJ, 708, 109

Brickhouse, N. S., Cranmer, S. R., Dupree, A. K., Luna, G. J. M., & Wolk, S. 2010, ApJ, 710, 1835

Calvet, N., Hartmann, L., & Kenyon, S. J. 1991, ApJ, 383, 752

Calvet, N. & Gullbring, E. 1998, ApJ, 509, 802

Calvet, N., Muzerolle, J., Briceño, C., Hernández, J., Hartmann, L., Saucedo, J. L., & Gordon, K. D. 2004, AJ, 128, 1294

Cargill, P. J. & Klimchuk, J. A. 2006, ApJ, 643, 438

Clarke, C. J., Lin, D. N. C., & Papaloizou, J. C. B. 1989, MNRAS, 236, 495

D'Angelo, C. R., Spruit, H. C. 2012, MNRAS, 420, 416

Donati, J.-F. et al. 2007, MNRAS, 380, 1297

Dupree, A., et al. (2012), ApJ, in press

Favata et al. 2005, ApJS, 160, 469

Fedele, D., van den Ancker, M. E., Petr-Gotzens, M. G., Ageorges, N., & Rafanelli, P. 2007, A&A, 472, 199

Feigelson, E. D. & DeCampli, W. M. 1981, ApJ, 243, L89

Flaccomio et al. 2005, ApJ, 160, 450

Freeman, P., Doe, S., & Siemiginowska, A. 2001, Proc. SPIE, 4477, 76

Gregory, S. G., Wood, K., & Jardine, M. 2007, MNRAS, 379, L35

Grosso, N., Kastner, J. H., Ozawa, H., Richmond, M., Simon, T., Weintraub, D. A., Hamaguchi, K., & Frank, A. 2005, A&A, 438, 159

Grosso, N. 2006, in ESA Special Publication, Vol. 604, The X-ray Universe 2005, ed. A. Wilson, 51-56

Grosso, N., Hamaguchi, K., Kastner, J. H., Richmond, M., & Weintraub, D. A. 2010, A&A, 522, A56

Güdel, M. et al. 2007, A&A, 468, 353

Güdel, M. & Nazé, Y. 2009, A&A Rev., 17, 309

Haisch, K. E., Lada, E. A., & Lada, C. J. 2001, ApJ, 553, L153

Hamaguchi, K., Grosso, N., Kastner, J. H., Weintraub, D. A., & Richmond, M. 2010, ApJ, 714, L16

Hamaguchi, K., et al. 2012, ApJ, submitted

Hartmann, L. & Kenyon, S. J. 1996, ARA&A, 34, 207

Hartmann, L. 1998 Accretion Processes in Star Formation (Cambridge, Cambridge University Press)

Herbig, G. H. 1977, ApJ, 217, 693

Herbig, G. H., Aspin, C., Gilmore, A. C., Imhoff, C. L., & Jones, A. F. 2001, PASP, 113, 1547

Herbig, G. H. 2007, AJ, 133, 2679

Imanishi, K., Koyama, K., & Tsuboi, Y. 2001, ApJ, 557, 747

Isobe, H., Shibata, K., Yokoyama, T., & Imanishi, K. 2003, PASJ, 55, 967

Itagaki, K., Nakano, S., & Yamaoka, H. 2008, IAU Circ., 8968, 2

Jones, A. F. 2008, CBET, 1231, 1

Joy, A. H. 1945, ApJ, 102, 168

Kastner, J. H., Huenemoerder, D. P., Schulz, N. S., Canizares, C. R., & Weintraub, D. A. 2002, ApJ, 567, 434

Kastner, J. H., et al. 2004, Nature, 430, 429

Kastner, J. H., et al. 2006, ApJ, 648, L43

Königl, A., Romanova, M. M., & Lovelace, R. V. E. 2011, arXiv:1106.2356

Kurosawa, R., Harries, T. J., Symington, N. H. 2006, MNRAS, 370, 580

Lin, D. N. C. & Papaloizou, J. C. B. 1985, In *Protostars and Planets II*, 981–1072

Long, M., Romanova, M. M., Kulkarni, A. K., & Donati, J.-F. 2011, MNRAS, 413, 1061

Lorenzetti, D., Larionov, V. M., Giannini, T., Arkharov, A. A., Antoniucci, S., Nisini, B., & Di Paola, A. 2009, ApJ, 693, 1056

Mamajek, E. E., Meyer, M. R., Hinz, P. M., Hoffman, W. F., Cohen, M., & Hora, J. L. 2004, ApJ, 612, 496

Martín, E.L., Rebolo, R., Magazzù, A., & Pavlenko, Ya.V. 1994, A&A,282, 503

Martín, E. L. 1997, A&A, 321, 497

McGehee, P. M., Smith, J. A., Hendon, A. A., Richmond, M. W., Knapp, G. R., Finkbeiner, D. P., Ivezić, $\check{Z}$., & Brinkmann, J. 2004, ApJ, 616, 1058

McLaughlin, D. B. 1946, AJ, 52, 109

McNeil, J. W. 2003, IAU Circ., 8284

Muzerolle, J., Megeath, S. T., Flaherty, K. M., Gordon, K. D., Rieke, G. H., Young, E. T., & Lada, C. J. 2005, ApJ, 620, 107

Ojha, D. K., et al. 2005, PASJ, 57, 203

Ojha, D. K., et al. 2006, MNRAS, 368, 825

Ojha, D. K., Ghosh, S. K., & Kaurav, S. S. 2008, IAU Circ., 9006

Orlando, S., Peres, G., & Reale, F. 2001, ApJ, 560, 499

Porquet, D., Dubau, J., & Grosso, N. 2010, Space Sci. Rev., 157, 103

Preibisch, T., et al. 2005, ApJS, 160, 401

Prentice, A. J. R. 1978, The Origin of the Solar System, p.111, ed. Dermott, S. F., Wiley, Chichester

Raassen, A. J. J. 2009, A&A, 505, 755

Reipurth, B. & Aspin, C. 2004, ApJ, 606, L119

Rice, W. K. M., Wood, K., Armitage, P. J. Whitney, B. A., & Bjorkman, J. E. 2003, MNRAS, 342, 79

Sacco, G. G., Orlando, S., Argiroffi, C., Maggio, A., Peres, G., Reale, F., & Curran, R. L. 2010, A&A, 522, A55

Sakamoto, T., Wallace, C. A., Donato, D., Gehrels, N., Okajima, T., & Ukwatta, T. N. 2011, Adv. Space Res., 47(8), 1444

Sanz-Forcada, J., Brickhouse, N. S., & Dupree, A. K. 2001, ApJ, 554, 1079

Scargle, J. D. 1982, ApJ, 263, 835

Semkov, E. 2004, Inf. Bull. Variable Stars 5578

Semkov, E. 2006, Inf. Bull. Variable Stars 5683

Shakura, N. I., & Sunyaev, R. A. 1973, A&A, 24, 337

Shibata, K. and Yokoyama, T. 2002, ApJ, 577, 422

Shu, F. H., Najita, J., Ostriker, E., Wilkin, F., Ruden, S., & Lizano, S. 1994, ApJ, 429, 781

Shukla, S. J., Weintraub, D. A., & Kastner, J. H. 2008, ApJ, 683, 893

Simon, T., Andrews, S. M., & Rayner, J. T. 2004, ApJ, 611, 940

Skinner, S., Briggs, K., & Güdel, M. 2006, ApJ, 643, 995

Skinner, S., Sokal, K., Güdel, M., & Briggs, K. 2009, ApJ, 696, 766

Stassun, K. G., van den Berg, M., Feigelson, E., & Flaccomio, E. 2006, ApJ, 649, 914

Stelzer, B. & Schmitt, J. H. 2004, A&A, 418, 687

Stelzer, B., Hubrig, S., Orlando, S., Micela, G., Mikulášek, Z., & Schöller, M. 2009, A&A, 499, 529

Teets, W. K., Weintraub, D. A., Grosso, N., Principe, D., Kastner, J. H., Hamaguchi, K., & Richmond, M. 2011, ApJ, 741, 83

Tsujimoto, M., Feigelson, E. D., Grosso, N., Micela, G., Tsuboi, Y., Favata, F., Shang, H., & Kastner, J. H. 2005, ApJS, 160, 503

Vacca, W. D., Cushing, M. C., & Simon, T. 2004, ApJ, 609, L29

Venkat, V. & Anandarao, B. G. 2006, IAU Circ., 8694

Venkat, V. & Anandarao, B. G. 2009, CBET, 2104

Venkat, V. & Anandarao, B. G. 2011, CBET, 2647

Vilhu, O., & Rucinski, S. M. 1983, A&A, 127, 5

Vuong, M. H., Montmerle, T., Grosso, N., Feigelson, E. D., Verstraete, L., & Ozawa, H. 2003, å, 408, 581

Walter, F. M. 1986, ApJ, 306, 573

Weintraub, D. A., Sandell, G., & Duncan, W. D. 1991, ApJ, 382, 270

Wolk, S. J. & Walter, F. M. 1996, AJ, 111, 2066

Woolfson, M. M. 1993, QJRAS, 34, 1

Wright, N. J., Drake, J. J., Mamajek, E. E., & Henry, G. W. 2011, ApJ, 743, 48

Yorke, H. W. & Bodenheimer, P. 1999, ApJ, 525, 530

Zhu, Z., Hartmann, L., Gammie, C., & McKinney, J. C. 2009, ApJ, 701, 620